

FACILITY AND FLOW DEPENDENCE ISSUES INFLUENCING THE
EXPERIMENTAL CHARACTERIZATION OF A LAMINAR SEPARATION BUBBLE
AT LOW REYNOLDS NUMBER

By

David Arthur Olson

A THESIS

Submitted to
Michigan State University
in partial fulfillment of the requirements
for the degree of

MASTER OF SCIENCE

Mechanical Engineering

2011

ABSTRACT

FACILITY AND FLOW DEPENDENCE ISSUES INFLUENCING THE EXPERIMENTAL CHARACTERIZATION OF A LAMINAR SEPARATION BUBBLE AT LOW REYNOLDS NUMBER

By

David Arthur Olson

There is an immediate and evolving need for Micro Air Vehicles (MAVs) in both the defense and civilian industry. The applications for these very small (bird and insect sized), remotely operated or autonomous vehicles range from reconnaissance to remote hazardous material identification. The fundamental fluid mechanics of these small aerial vehicles, operating at low speeds, are not yet fully understood. One particular issue is a documented discrepancy in the characteristics of the laminar separation bubble on airfoils obtained from various experimental and computational studies at Reynolds numbers typical of MAV operation. The influence of added freestream turbulence, among other facility-dependent issues, is studied for a range of chord Reynolds numbers ($2 \times 10^4 - 6 \times 10^4$), and angles of attack ($0^\circ - 11^\circ$). The baseline flow is compared against the flow with added freestream turbulence using single-component Molecular Tagging Velocimetry (1c-MTV) with a cross-stream spatial resolution of $52 \mu\text{m}$. An increase in freestream turbulence is shown to decrease the size of the separation bubble, both by delaying separation and triggering an earlier reattachment. Increased freestream turbulence is also characterized by a reduction in the height of the reversed flow region, and a decrease in the streamwise velocity fluctuations downstream of separation. The experimental characterization of the separation bubble is also found to be sensitive to near-wall spatial resolution. The introduced bias error shortens the measured bubble length and is dependent on the shape of the separation bubble.

Copyright by
DAVID ARTHUR OLSON
2011

ACKNOWLEDGMENTS

First and foremost, I would like to acknowledge my advisors Dr. Manooch Koochesfahani and Dr. Ahmed Naguib for their continual support and guidance throughout the course of project. And, I would like to thank the other members of my guidance committee: Dr. Farhad Jaber and from the Air Force Research Laboratory, Dr. Miguel Visbal.

I graciously thank Dr. Shahram Pouya for his endless patience and support in the early stages of my research (and all the troubleshooting in the latter stages). I would like to thank Rohit Nehe for our endless discussions, which ranged from the technical details to recommendations for quality movies and television. I also greatly appreciated all of the much needed ping-pong breaks at all hours of the day and night. And I would also like to thank Dr. Bruno Monnier, who has provided good daily conversation over lunch and has made Rohit and I step up our ping-pong game.

Lastly, I would like to thank my friends and family for attempting to keep me sane during this entire process.

TABLE OF CONTENTS

List of Tables	vii
List of Figures	viii
Nomenclature	xi
1 Introduction	1
1.1 Motivation	1
1.2 Background	1
2 Experimental Methods	4
2.1 Facility	4
2.1.1 Flow Facility	4
2.1.2 Airfoil	8
2.1.3 Grid Generated Turbulence	13
2.2 Molecular Tagging Velocimetry (MTV)	14
2.2.1 Background	14
2.2.2 Current Implementation	14
2.2.3 Error Quantification of 1c-MTV over an Airfoil Surface	16
2.3 Quantifying the Freestream Turbulence	18
2.3.1 Background	18
2.3.2 Technique	19
2.4 Data Acquisition	22
2.4.1 Imaging	22
2.4.2 Image Processing	27
2.4.3 Alignment and Synchronization	28
2.5 Experiments	32
2.5.1 Experimental Parameters	32
2.5.2 Experimental Procedure	32
3 Results and Discussion	34
3.1 Freestream Turbulence Characteristics	34
3.2 Representative Results	37
3.2.1 Streamwise Velocity Contours: Mean and Fluctuation	37
3.2.2 Separation and Reattachment	39
3.3 Characterizing the Laminar Separation Bubble	42
3.3.1 Influence of Added Freestream Turbulence	42

3.3.2	Influence of Angle of Attack	48
3.3.3	Influence of Reynolds Number	48
3.4	Comparisons of LSB Characteristics	51
3.4.1	Separation and Reattachment	51
3.4.1.1	Reynolds Number 20,000	51
3.4.1.2	Reynolds Number 30,000	54
3.4.1.3	Reynolds Number 40,000	56
3.4.2	Bubble Length	58
3.4.3	Summary of LSB Characteristics	59
3.5	Facility and Flow Dependent Issues	60
3.5.1	Freestream Turbulence	60
3.5.2	Flow Three-Dimensionatlity	61
3.5.3	Airfoil Shape	61
3.5.4	Near-wall Spatial Resolution	62
3.5.5	Uncertainty in Wall location	63
3.5.6	Angle of Attack Sensitivity	63
4	Summary	65
4.1	Summary	65
4.2	Future Work	66
4.3	Conclusions	67
A	Freestream Turbulence	69
A.1	Freestream Turbulence Spectra	69
B	Mean and RMS Contours	73
B.1	Mean Flow field Evolution by Angle of Attack	73
B.2	RMS Flow field Evolution by Angle of Attack	77
B.3	Mean Flow field Evolution by Reynolds Number	81
C	Compiled LSB Characteristics	86
D	Miscellaneous	88
D.1	Test Section Photos	88
D.2	Procedure of Simulated Experiments	90
D.3	Experimental Procedure	92
	Bibliography	96

LIST OF TABLES

2.1	Experimental test matrix	33
3.1	Freestream characteristics	36
C.1	Compiled LSB characteristics	87

LIST OF FIGURES

1.1	A typical laminar separation bubble	2
2.1	Flow facility	6
2.2	Test section schematic	7
2.3	Airfoil profile	8
2.4	Error in airfoil profile	9
2.5	Airfoil camber line	10
2.6	Airfoil pitching system	11
2.7	Near-wall regions of airfoil surface	12
2.8	Experimental determination of surface location	12
2.9	Turbulence-generating woven mesh screen	13
2.10	Example of MTV	15
2.11	Schematic representing the 1c-MTV error	16
2.12	Simulated experiment 1c-MTV error results	17
2.13	Enlarged view of simulated experiment 1c-MTV error results	18
2.14	Sample spatial autocorrelation of the freestream	20
2.15	Sample spatial autocorrelation coefficients of the freestream	21
2.16	Sample 2c-MTV image pair	23

2.17	Sample 1c-MTV image pair	24
2.18	Sample FOV shift diagram	26
2.19	Hardware diagram	30
2.20	Timing diagram	31
3.1	Freestream spectra	35
3.2	Representative contour of streamwise velocity	38
3.3	Representative contour of streamwise velocity fluctuation	38
3.4	Representative view of separation	40
3.5	Representative view reattachment	41
3.6	Influence of increased FSTI on \bar{u} at $Re_C = 3 \times 10^4$ and moderate α	43
3.7	Influence of increased FSTI on \bar{u} at $Re_C = 2 \times 10^4$ and high α	44
3.8	Influence of increased FSTI on \bar{u} at $Re_C = 4 \times 10^4$ and moderate α	45
3.9	Influence of increased FSTI on u_{rms} at $Re_C = 4 \times 10^4$ and moderate α	46
3.10	Influence of increased FSTI on u_{rms} at $Re_C = 3 \times 10^4$ and moderate α	47
3.11	Angle of attack effect on separation and reattachment locations	49
3.12	Reynolds number effect on separation and reattachment locations	50
3.13	Separation and reattachment locations, $Re_C = 2 \times 10^4$	52
3.14	Separation and reattachment locations, $Re_C = 3 \times 10^4$	54
3.15	Separation and reattachment locations, $Re_C = 4 \times 10^4$	56
3.16	Laminar separation bubble length	58

3.17	Near-wall region of separation	62
A.1	Freestream PSD	70
A.2	Freestream PSD for each Reynolds number	72
B.1	\bar{u} for $Re_c = 2 \times 10^4$	74
B.2	\bar{u} for $Re_c = 3 \times 10^4$	75
B.3	\bar{u} for $Re_c = 4 \times 10^4$	76
B.4	u_{rms} for $Re_c = 2 \times 10^4$	78
B.5	u_{rms} for $Re_c = 3 \times 10^4$	79
B.6	u_{rms} for $Re_c = 4 \times 10^4$	80
B.7	Reynolds number effect on baseline \bar{u} , low α	82
B.8	Reynolds number effect on baseline \bar{u} , medium α	83
B.9	Reynolds number effect on baseline \bar{u} , high α	84
B.10	Reynolds number effect on increased FSTI \bar{u} , high α	85
D.1	Test section photos	89

Nomenclature

α	Angle of attack
\bar{u}	Mean streamwise velocity
ν	Kinematic viscosity
c	Chord
L_y	Integral length scale
u_{rms}	Root mean square of the streamwise velocity
U_∞	Magnitude of the freestream velocity
(X,Y)	Lab reference frame with X along the bottom of the tunnel
(x,y)	Airfoil reference frame, x is along the chordline and the leading edge is (x=0,y=0)
1c-MTV	Single-component MTV
2c-MTV	Two-component MTV
Re_c	Chord Reynolds number, $Re_c = \frac{U_\infty c}{\nu}$
FOV	Field of view

FSTI	Freestream turbulence intensity
hp	Horsepower
LSB	Laminar separation bubble
mC	Milli-chord, $1 \text{ mC} = 0.001c$
MTV	Molecular Tagging Velocimetry
PSD	Power spectral density
RMS	Root mean square
SNR	Signal to noise ratio
u,u	The streamwise component of velocity along the X-direction
UV	Ultraviolet
v,v	The cross-stream component of velocity along the Y-direction

Chapter 1

Introduction

1.1 Motivation

Low Reynolds number ($10^4 - 10^5$) aerodynamic flows are found in applications ranging from small wind turbines, model aircrafts, to bio-mimetic devices and Micro Air Vehicles (MAVs). Developments in complementary technologies, such as microelectronics and lightweight power supplies, have brought MAVs into focus recently for a variety of applications in both the civilian and defense industry. They are well suited for reconnaissance, search and rescue, remote diagnostics, and other applications where human presence is not possible or hazardous.

1.2 Background

The boundary layer of airfoils in the low-Reynolds number regime tends to remain laminar, at least for some portion of the airfoil. This renders the boundary layer susceptible to separation while the flow is still laminar, a process that is primarily dictated by the adverse pressure gradient and is referred to as laminar separation. The separated shear layer will

typically transition into turbulence over the surface of the airfoil and will then reattach to the surface, forming a laminar separation bubble, as depicted in Figure 1.1. If the separated shear layer does not reattach to the surface, it is referred to as an open separation.

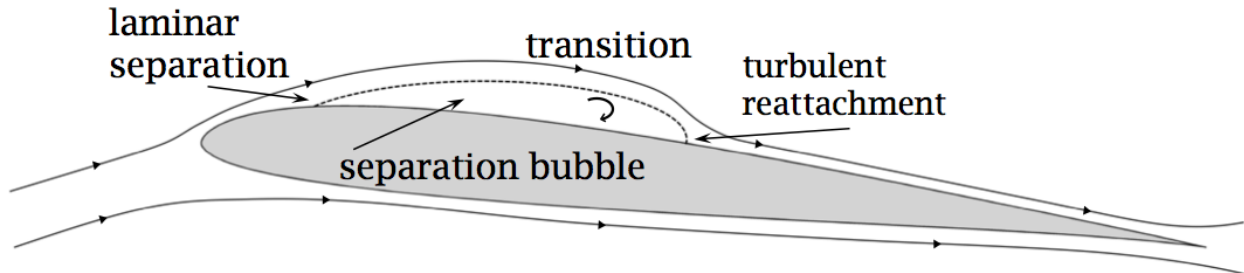


Figure 1.1: The general characteristics of a laminar separation bubble are shown. In the mean flow, separation is defined by the location at which the wall shear stress is zero, corresponding to the location where the dividing streamline between forward and reversed flow region intersects the wall. Reattachment is also defined in the mean flow where the wall shear stress returns to zero and the diving streamline intersects the wall again.

The presence of a laminar separation bubble is typically associated with an increase in drag and decrease in lift and is therefore, detrimental to the performance. The bursting of a laminar separation bubble (i.e. an open separation) is not only detrimental to the performance, but the stability of the aircraft. In the development of MAVs, it is important that these flow dynamics are understood so they may be properly modeled and resolved in computational studies. The steady flow around a stationary SD7003 airfoil has been used in various studies (both experimental and computational) in the literature to investigate this flow phenomena.

There are however, discrepancies in the literature in the locations of separation and reattachment (which define the laminar separation bubble) for this airfoil, e.g. see Ol et al. (2005); Katz (2010); Olson et al. (2011). This presents a significant challenge for validating simulations. The discrepancies have previously been attributed to: differences in spatial

resolution by Ol et al. (2005), and differences in freestream turbulence by Burgmann and Schröder (2008); although none of the studies examined these effects systematically.

Freestream broadband turbulence acts as an excitation source for the boundary layer instability upstream of separation and the Kelvin-Helmholtz instability of the separated shear layer. Based on physical reasoning, increased freestream turbulence would be expected to delay separation and trigger an earlier transition and subsequent reattachment.

In the present work, the characteristics of the laminar separation bubble on an SD7003 airfoil are studied experimentally for a range of angle of attack ($\alpha = 0^\circ - 11^\circ$) and chord Reynolds number $Re_c = 2.6 \times 10^4$. The measurements are carried out using single component Molecular Tagging Velocimetry over the entire suction side of the airfoil. The freestream turbulence of the test facility is modified and the resulting flow with increased freestream turbulence is compared to the baseline case. The primary characteristics of interest are the locations of separation and reattachment, the separation bubble thickness, and the characteristics of the streamwise velocity fluctuations. The results of the current study are compared to various other experimental and computational studies in the literature. The inherent limitations of the experimental techniques and their impact on accurately characterizing the laminar separation bubble are also discussed.

Chapter 2

Experimental Methods

The influence of added Freestream Turbulence Intensity (FSTI) on the mean flow around a stationary SD7003 airfoil was studied experimentally for a range of chord (c) Reynolds number ($Re_c = 2 \times 10^4 - 6 \times 10^4$) and angle of attack ($\alpha = 0^\circ - 11^\circ$). The baseline flow was compared against the flow with added freestream turbulence using single-component Molecular Tagging Velocimetry (1c-MTV) with a specific focus on the laminar separation bubble (LSB) which may develop on the suction side of the airfoil.

2.1 Facility

2.1.1 Flow Facility

Experiments were performed in a 10,000 L close-loop water tunnel operating with a free-surface. The facility was designed and manufactured by Engineering Laboratory Design and is located at Michigan State University's Turbulent Mixing and Unsteady Aerodynamics Laboratory (TMUAL) in East Lansing, Michigan. The various flow management de-

vices and their locations are illustrated in Figure 2.1 while a more detailed schematic of the test section configuration is shown in Figure 2.2. Photos of the test section may be found in Figure D.1, located in Appendix D.1. The test section is 24 in. \times 24 in. \times 96 in. (61 cm \times 61 cm \times 243 cm) and the polycarbonate coated Plexiglas walls provide full optical access in the visible spectrum for unobstructed imaging of the measurement region. Quartz windows are mounted in a flat-bottom boat-shaped holders that skim the surface of the water to permit the transmission of the UV photon source to the measurement region while eliminating beam scatter due to water surface irregularities. The tunnel's speed is adjusted with a Toshiba Tosvert VT130H1U motor controller which powers a 20 hp motor connected to the tunnel's impeller. The fluid temperature is measured for each experiment using a VWR 61066-104 thermometer (with nominal accuracy of $\pm 0.5^\circ C$) and is taken into account in determining the viscosity for calculating the Reynolds number.

Two coordinate systems are used in these experiments. The first, (X, Y) , is relative to the test section with X along the streamwise direction (aligned with the bottom of the tunnel) and Y is in the cross-stream, which are depicted in the top of Figure 2.2. The streamwise velocity, (u) , and cross-stream velocity (v) are also defined in this coordinate system with the magnitude of the freestream is defined as U_∞ . The origin of this coordinate system is not explicitly defined.

The second coordinate system, which will be used to present velocity contours and discuss locations along the airfoil (such as separation and reattachment), is shown near the bottom of Figure 2.2 with the origin defined at the leading edge of the airfoil with x along the chordline and y normal to it. Note, both u and v are still defined in (X, Y) .

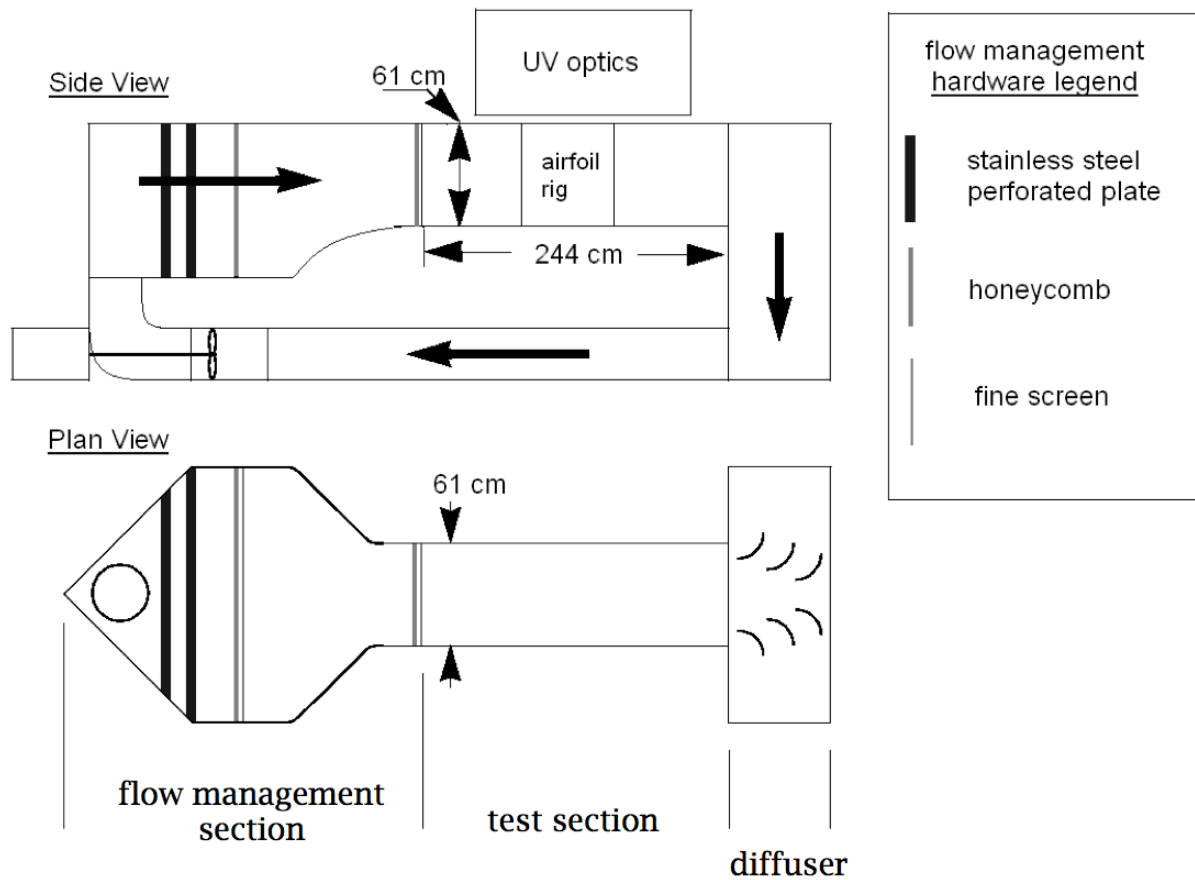


Figure 2.1: Flow Facility Schematic. The original drawing was created by Gen-drich (1999) and has been updated accordingly.

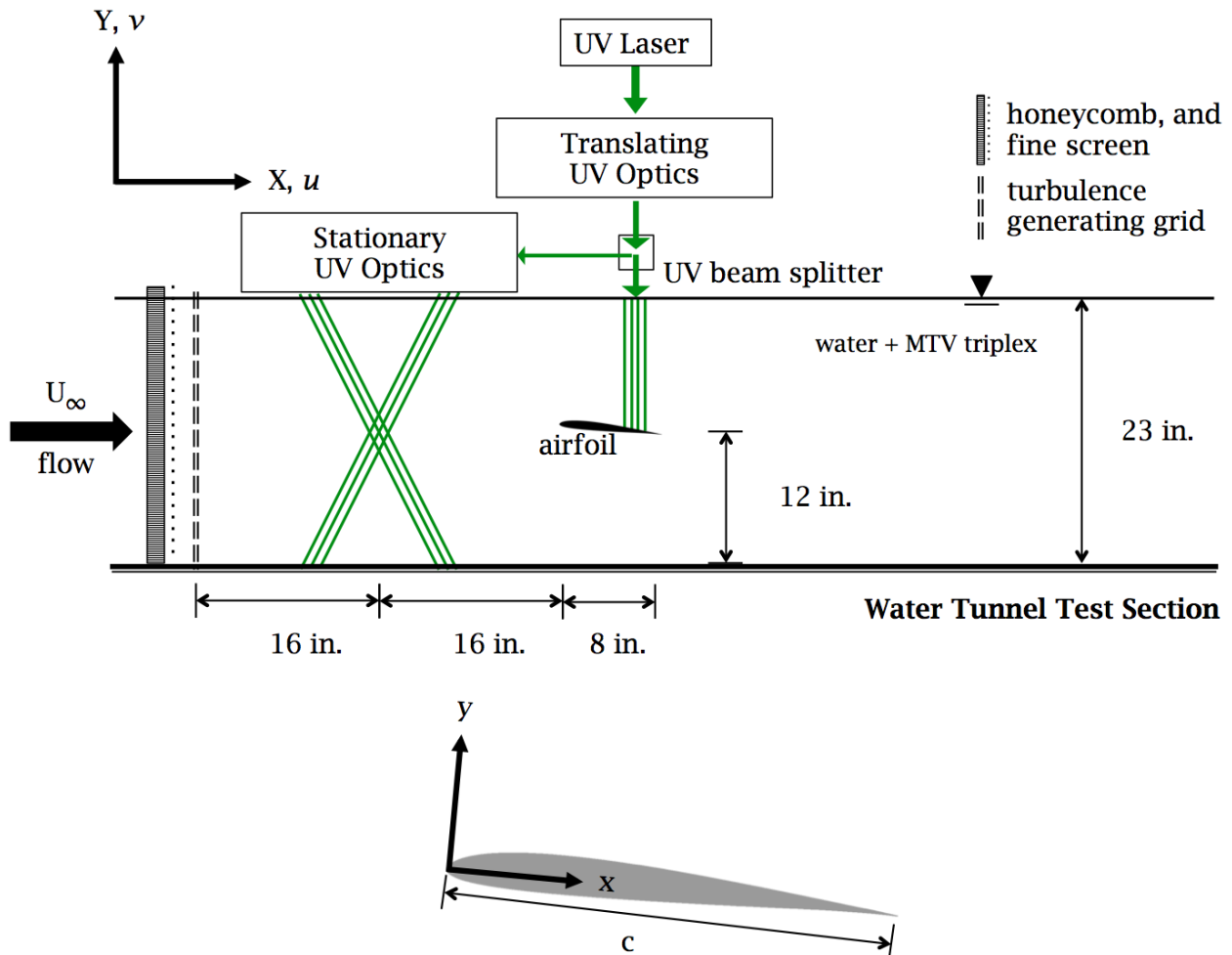


Figure 2.2: Test Section Schematic. The relative position of the flow management, turbulence generating screen, airfoil and measurement regions are shown above. The upstream measurement location is located along the chordline at a geometric angle of attack, $\alpha = 0^\circ$ relative to the bottom of the tunnel. The coordinate system (X, Y) is fixed, with no explicitly defined origin, and relative to the test section. The coordinate system (x, y) rotates with the airfoil with its origin defined as the leading edge of the airfoil. The chord length, c , is also indicated. The green arrows and lines represent the simplified laser beam path. For interpretation of the references to color in this and all other figures, the reader is referred to the electronic version of this thesis.

2.1.2 Airfoil

The theoretical airfoil profile designated for testing was an SD7003, a low Reynolds number airfoil that has a long separation bubble over a wide range of angle of attack and Reynolds number; more detailed information may be found in Selig et al. (1995) on the airfoil's performance and characteristics at various Reynolds numbers. This particular airfoil was chosen due to the large number of recent comparisons in the literature, both experimental and computational, and the considerable amount of discrepancy in a number of these studies. The physical airfoil model has a chord length, $c = 7.959$ in., a span of $b \approx 18$ in., and was loaned to TMUAL by Dr. Michael Ol of the Air Force Research Laboratory, Wright Patterson Air Force Base, Ohio.

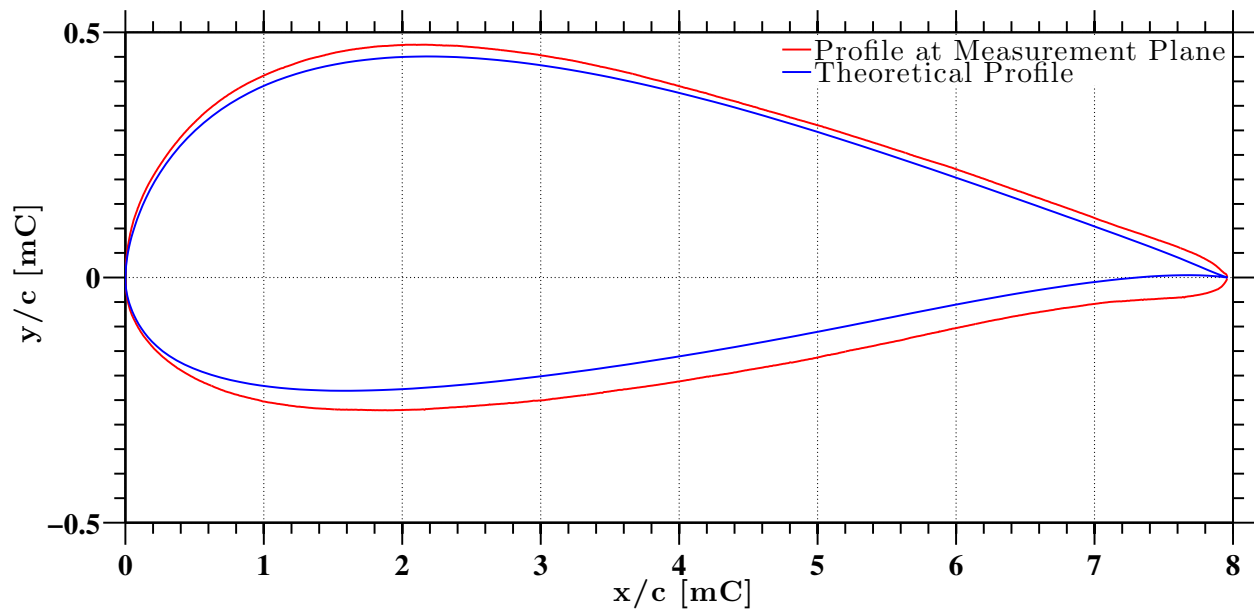


Figure 2.3: The theoretical profile is plotted against the measured airfoil profile at the measurement plane (not to scale). The actual airfoil is clearly thicker than the theoretical profile with most of the added thickness from the bottom surface.

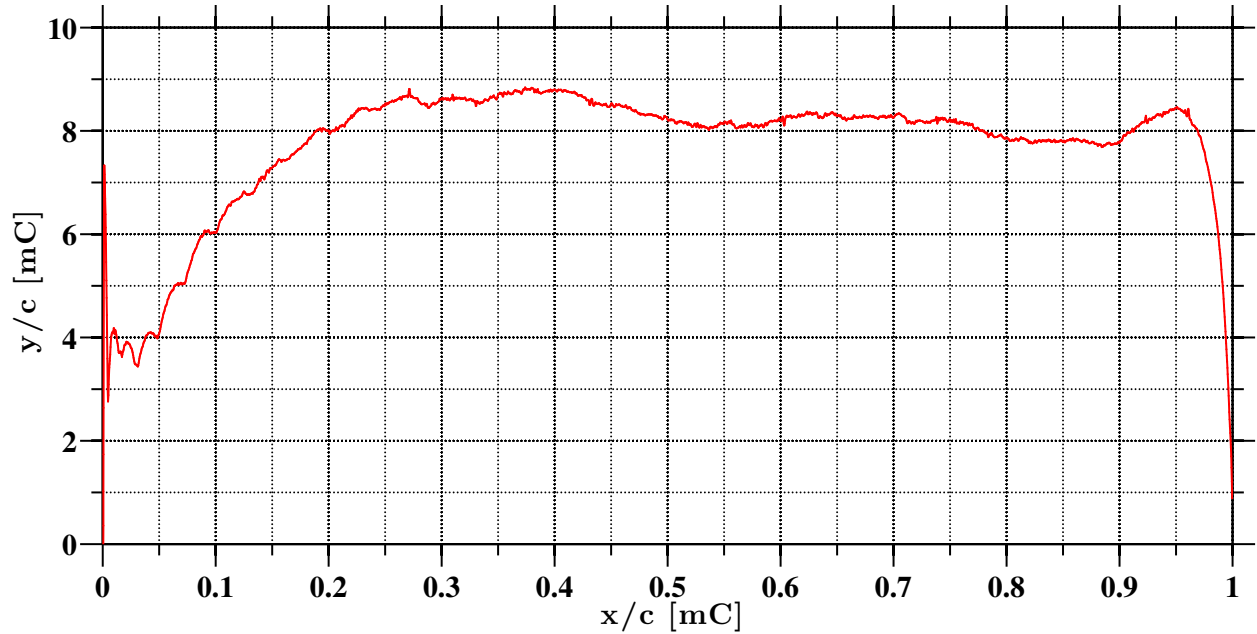


Figure 2.4: The error in the profile thickness as a function of chord. The error in thickness is nearly constant over 70% of the chord at ~ 8 mC (0.064 in.)

The airfoil’s actual shape was determined by GKS Global Services in Plymouth, MI with a nominal accuracy of ± 0.0015 in. using a triangulation 3D laser scanner. The measured shape at the spanwise location of the measurement plane is compared to the theoretical profile in Figure 2.3 and is noticeably thicker, approximately a constant 8 mC (1 mC = 0.001c) over 70% of the chord, as shown in Figure 2.4. It was not possible to determine if the previous study done by Katz (2010) at MSU, which used the same model, also had the same profile thickness. The measurement plane was chosen to be ~ 2.6 in. off mid-span to avoid surface anomalies that develop after prolonged underwater exposure.

Figure 2.5 shows the camber lines of both the theoretical and current airfoil profile. The current airfoil’s maximum camber was determined to be 1.36% compared to 1.46% in the theoretical profile. The location of maximum camber is farther upstream at 0.30 x/c compared to 0.35 x/c of the theoretical profile. There is little visual deviation in the camber lines

for $x/c < 0.20$, but a systematic decrease in the camber line is seen from $0.4 > x/c > 0.95$.

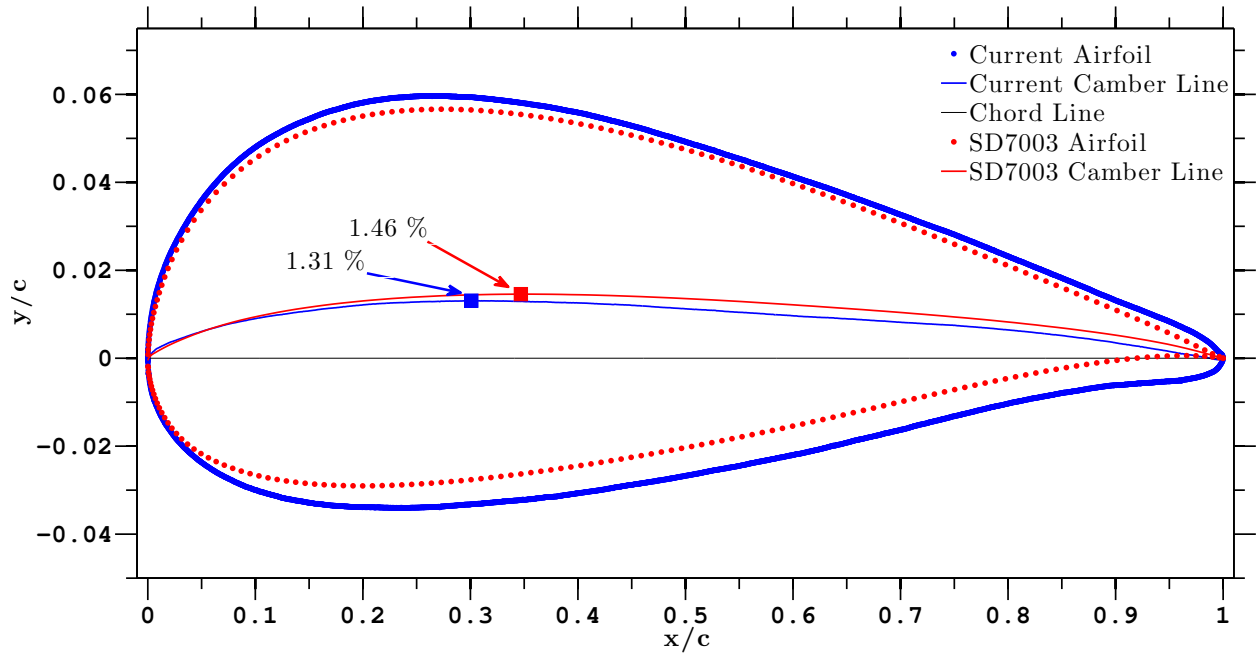


Figure 2.5: The normalized profiles of the current and theoretical airfoil and their respective camber lines (not to scale). The location of the peak camber is identified by the square symbols with the percent camber indicated. The current airfoil's peak camber is less and is located farther upstream than the theoretical SD7003 airfoil.

Deviation from two-dimensional flow conditions were minimized by mounting the airfoil between two acrylic plates since the airfoil's span (~ 18 in.) is not as wide as the test section (24 in.). The airfoil's angle of attack was adjusted using a Velmex A1506P40-S1.5 linear traverse mounted to a lever arm 7 in. from the pitch axis as depicted in Figure 2.6. This manual pitching system provided a relative angle change accuracy of $\pm 0.05^\circ$, determined by rotational correlation of images of the airfoil profile.

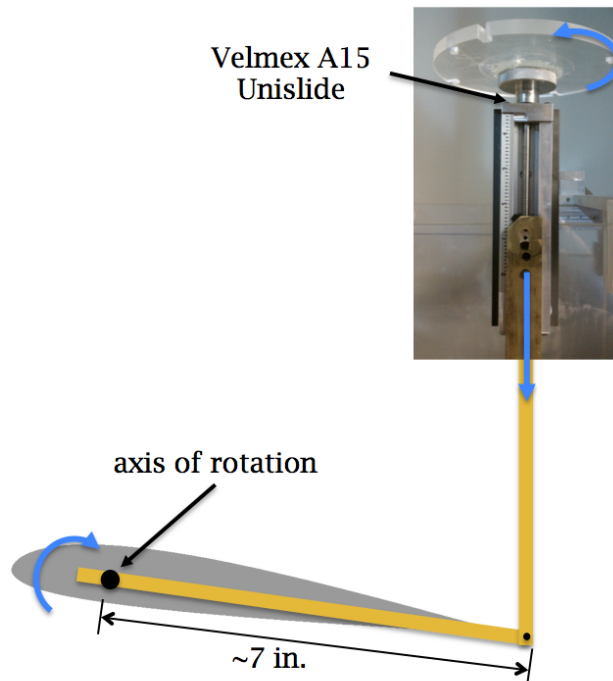


Figure 2.6: A Velmex A1506P40-S1.5 Unislide traverse with a 0.001 in. graduated knob is connected via a lever arm to the pitch axis of the airfoil to change the angle of attack of the airfoil. The blue arrows indicate the motion with the black circles representing pin joints.

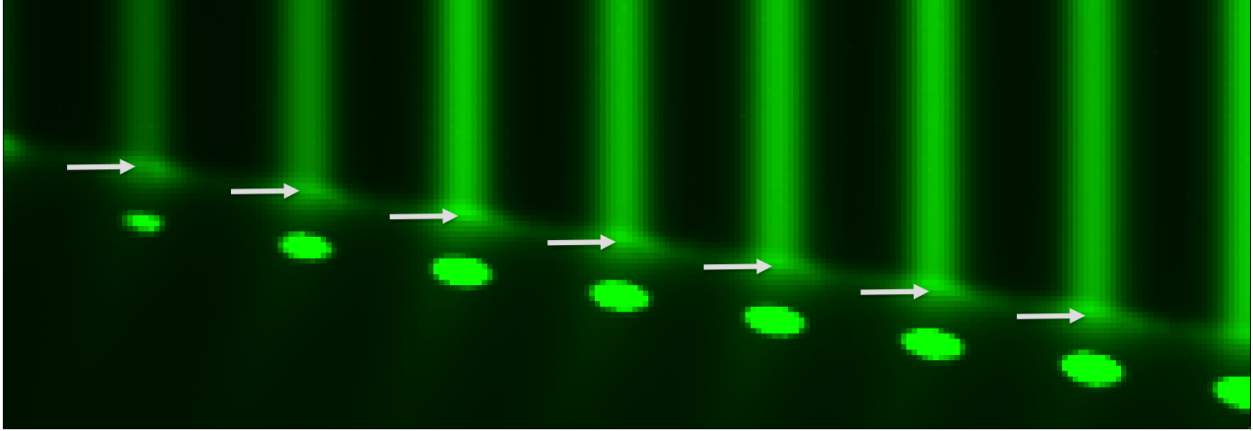


Figure 2.7: A small region (width = 170 pixels) of an average undelayed MTV image (see Section 2.2.2 for more details) is shown above. The white arrows indicate the manually determined surface locations. The image has been artificially colored green to resemble the emission wavelength. The large bright spots beneath the surface are artifacts of the Pixelfly CCD and do not effect the measurements.

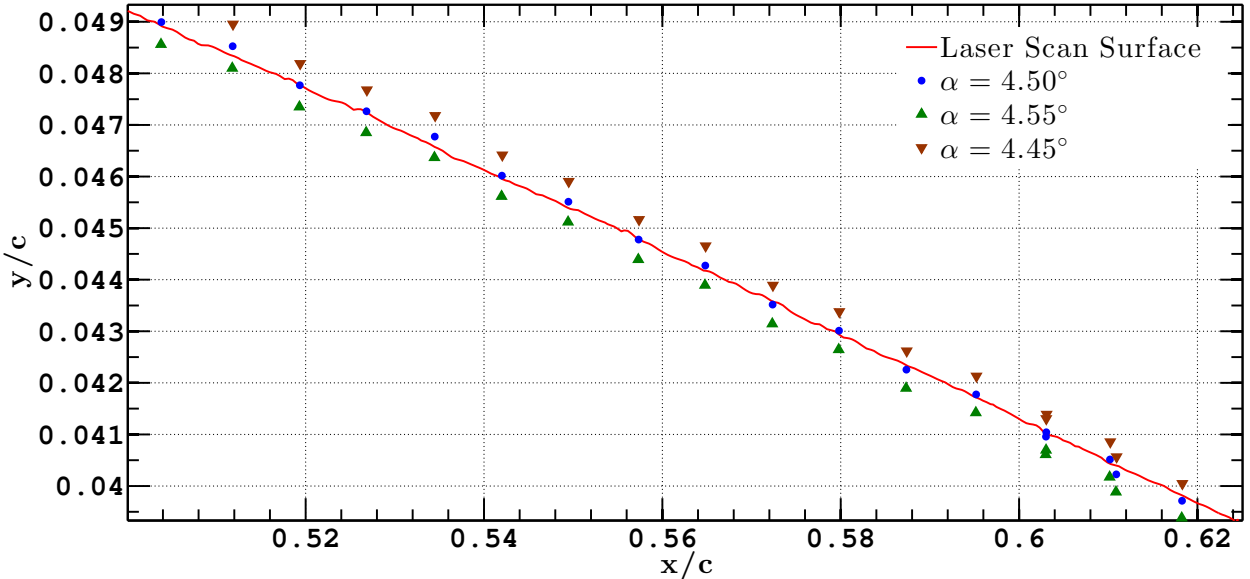


Figure 2.8: The manually located surface locations are plotted for different possible geometric angles of attack. The error in location of these points to the laser scan surface was minimized to yield $\alpha = 4.5^\circ$ for this case. It is easily seen the accuracy of this technique is better than the $\pm 0.05^\circ$ shown here. Note, only a very small portion of the suction side of the airfoil surface is shown.

The geometric angle of attack was determined by a least-squares minimization of the error between airfoil surface location manually located from each laser line intersecting with the surface (shown in Figure 2.7) and the surface profile as measured by the laser scanning. The repeatability of visually determining the surface was ± 1 pixel. The uncertainty of this technique is better than $\pm 0.05^\circ$ (estimated by the procedure shown in Figure 2.8) which also accounts for all other angle alignment uncertainties.

2.1.3 Grid Generated Turbulence

The water tunnel's freestream turbulence is modified during the current experiments by the introduction of a mesh grid 4c upstream of the airfoil as depicted in the test section schematic (Figure 2.2). The grid itself, shown in Figure 2.9, is a stainless steel woven wire screen with a mesh size of 0.75 in. and a wire diameter of 0.120 in.

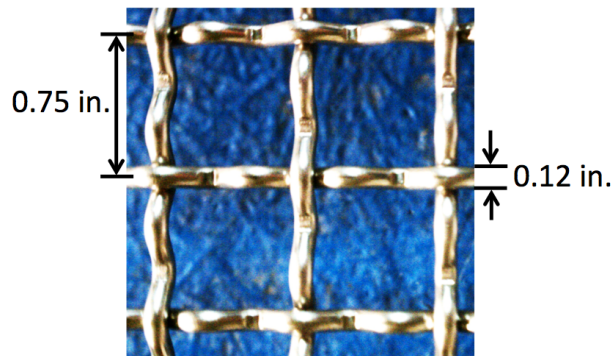


Figure 2.9: A small region of the stainless steel woven mesh screen is shown with the mesh size and wire diameter indicated.

The freestream turbulence intensity (FSTI), based on the streamwise velocity component, was measured from FOV #11 (see Figure 2.18), which extends over a range of 2.10 – 4.20 in. ($Y/c = 0.264 - 0.528$) above the leading edge and a range of 0 – 1.09 in. ($X/c = 0 - 0.14$) downstream of the leading edge of the airfoil. The baseline FSTI over a range of tunnel speed

$U_\infty \approx 9 - 19$ cm/s was 0.42 - 0.66%, which corresponds to ($Re_C \approx 2 \times 10^4 - 4 \times 10^4$). In the presence of the grid, the FSTI was measured to be 0.95 - 1.47% over the same range of tunnel speed. The details of the freestream turbulence measurements using single-component MTV (1c-MTV) may be found in Section 2.3.

2.2 Molecular Tagging Velocimetry (MTV)

2.2.1 Background

Molecular Tagging Velocimetry (MTV) is a whole field measurement technique in which particular molecules of a homogenous solution are utilized as long lifetime tracers through photon excitation. In the current application, a phosphorescent supramolecule, Gendrich et al. (1997), is utilized as the tracer and is excited by a pulsed UV Excimer laser (Lambda Physik XeCl 308 nm). The laser is fired once to excite, or tag, molecules and the resulting phosphorescent emission is interrogated twice with a prescribed time delay to form an image pair. Features in the images, created by spatial gradients in intensity, are correlated to yield an estimate of the displacement, and with the prescribed time delay, the velocity of the flow field as shown in Figure 2.10. The reader is referred to Gendrich and Koochesfahani (1996); Gendrich et al. (1997); Koochesfahani and Nocera (2007) for more details on the history, applications, and photochemistry of MTV.

2.2.2 Current Implementation

The experiments utilized both single and two-component MTV. Two-component measurements were used to monitor freestream fluctuations in the approach flow 2c upstream of the

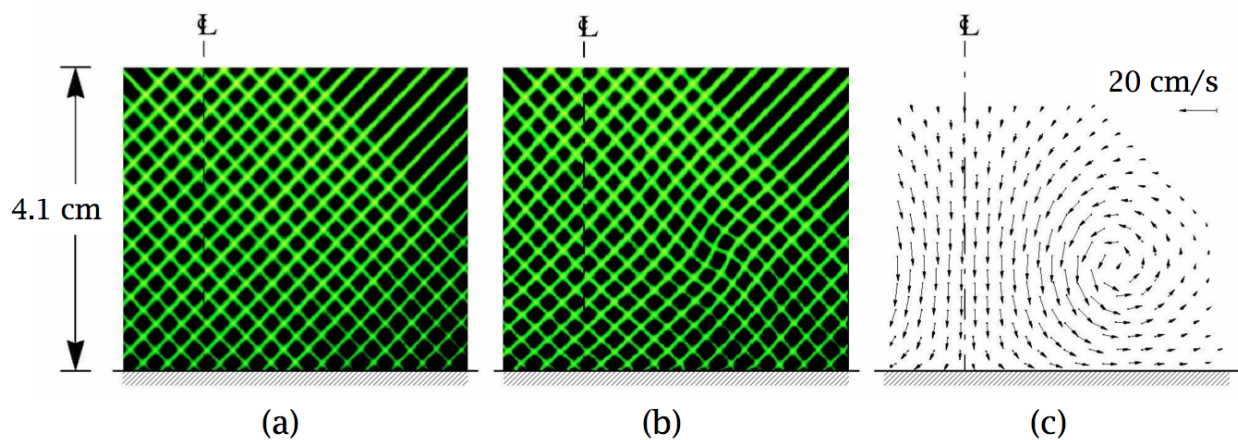


Figure 2.10: A typical 2c-MTV image pair and resulting 2-component velocity vector field. (a) The fluid flow of a vortex ring impinging on a flat plate with normal incidence is imaged $\sim 1 \mu\text{s}$ after the laser pulse. (b) The same tagged fluid is interrogated again 8 ms after the first image. (c) The resulting 2-component velocity vector field is derived from correlating the undelayed (a) and delayed (b) images. (Gendrich and Koochesfahani, 1996).

airfoil during the experiments and were also used for calibrating the tunnel speed. In the primary measurement region, the suction side of the airfoil, single component MTV (1c-MTV) was employed to measure the streamwise component of velocity.

Single-component MTV is a highly attractive technique for the current study because it captures the key features of interest, separation and reattachment, and provides highly detailed velocity profiles for future comparisons to simulations. The very high resolution, which is approximately 10 times that of recent PIV studies of this airfoil, Burgmann et al. (2007); Burgmann and Schröder (2008), comes at the expense of a possible error due to the unresolved velocity component in the measurement plane. The inherent error associated with this technique and the implications on this type of flow field are discussed in the next section, 2.2.3.

2.2.3 Error Quantification of 1c-MTV over an Airfoil Surface

The inherent error in 1c-MTV, previously investigated by Hill and Klewicki (1996) is defined as follows in Koochesfahani and Nocera (2007). The error is most easily shown by the diagram in Figure 2.11 which shows the initial tagged line of fluid and displaced fluid molecules at a later time. If there is a component of the velocity vector (\underline{V}) parallel to the tag line, i.e. $\theta \neq 0$, the error (Δu) is also non-zero.

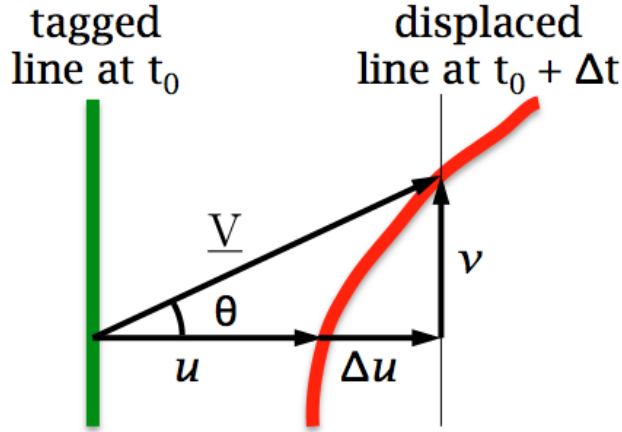


Figure 2.11: The tagged fluid at t_0 (green) and $t_0 + \Delta t$ (red) due to the velocity vector \underline{V} . The measured streamwise velocity u and its error Δu is also shown.

The images are processed assuming the fluid molecules have displaced normal to the tag line (x-direction), which, in the presence of a v -component of velocity, is not generally a good assumption. The error in the measured streamwise velocity component, as presented in Koochesfahani and Nocera (2007), may be formally expressed as

$$\frac{\Delta u}{u} = \frac{v}{u} \frac{\partial u}{\partial y} \Delta t \quad (2.1)$$

where the error is defined in terms of the flow variables and Δt , the time delay between the image pair. From Equation 2.1, it is clear that $\Delta u \rightarrow 0$ near surfaces, where $\frac{v}{u} \rightarrow 0$,

and in the freestream, where $\frac{\partial u}{\partial y} \rightarrow 0$. The error may be minimized by reducing the Δt between interrogations, but the latter cannot be set arbitrarily small in experiments because the molecules must displace far enough to be accurately measured.

In order to determine the accuracy of 1c-MTV over the entire suction side of the airfoil, “simulated experiments” were conducted using CFD simulations (performed by Galbraith (2009)) of the mean flow around an SD7003 at $Re_c = 4 \times 10^4$ and $\alpha = 4^\circ$. Other conditions were also studied but have been excluded for brevity. The “simulated experiments” were performed using the procedure outline in Appendix D.2, which match the assumptions and parameters of the experiments.

The magnitude of the error, normalized by the freestream velocity ($\frac{|\Delta u|}{U_\infty}$), between the known flow field and the simulated experiment is shown in Figures 2.12 and 2.13 for $\Delta t = 5$ ms (which is typical of the current experiments). Most of the flow field has a negligible amount of error with the highest values occurring near the leading edge, as expected, due to the very high velocity gradients and large v in this region. The error in the separated shear layer, extending from $\sim 0.24c - 0.7c$, is $< 2\%$.

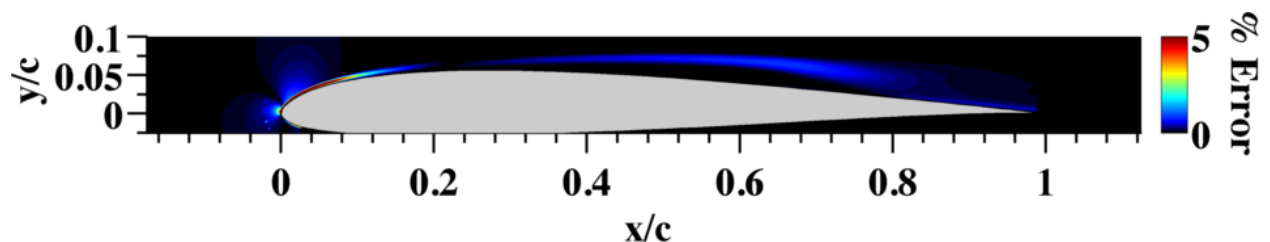


Figure 2.12: The error in the 1c-MTV estimate of u is shown as $\frac{|\Delta u|}{U_\infty} \times 100$ over the entire suction side of the airfoil.

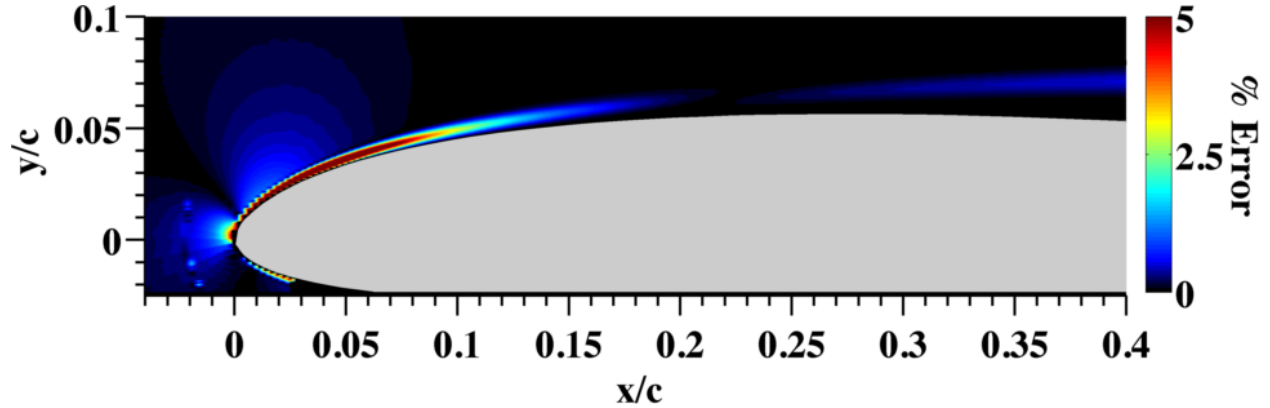


Figure 2.13: An enlarged view of Figure 2.12 over the leading edge.

2.3 Quantifying the Freestream Turbulence

2.3.1 Background

The freestream turbulence must be accurately quantified to enable future comparisons to simulations. Previous measurements of the FSTI have varied in this facility: 0.3% (Gendrich (1999)), 1.5% (Bohl (2002)), and most recently, $\sim 2\%$ (Katz (2010)) but the spectral components and length scales have never been reported. The flow management and tunnel operating conditions were not necessarily the same between any of these investigations and must be measured again for completeness.

Traditionally, LDV (Laser Doppler Velocimetry) and hot-wire anemometry (or hot-film anemometry) have been utilized for the measurement of turbulent quantities. Both techniques are nominally point measurements of high temporal resolution whereas MTV is a whole field technique with a high, user-configurable spatial resolution but a typically much lower data rate. At the time of the current experiments neither LDV or hot-film anemometry was available for use, so the feasibility of using MTV for FSTI was investigated.

2.3.2 Technique

The two primary quantities in these experiments used to describe the freestream turbulence are: the freestream turbulence intensity,

$$\text{FSTI} = \frac{u_{\text{rms}}}{U_{\infty}} \quad (2.2)$$

and the integral length scale,

$$L_y = \int_0^{\xi_0} R_{uu}(\xi) \, d\xi \quad (2.3)$$

where u_{rms} is the RMS (root mean square) of streamwise velocity fluctuation, with ξ as the spatial offset in the cross-stream direction and ξ_0 is the first zero crossing of $R_{uu}(\xi)$.

The autocorrelation function, $r_{uu}(\Delta\xi)$, is obtained from measurements of the streamwise velocity at N_y discrete spatial locations along y , $\Delta\xi$, and time record (m), and is given by:

$$r_{uu}(\Delta\xi; m) = \frac{\sum_{n=0}^{N_y-1-\Delta\xi} u(m, n) u(m, n - \Delta\xi)}{N_y - \Delta\xi} \quad (2.4)$$

The autocorrelation coefficient, $R_{uu}(\Delta\xi)$, is defined as:

$$R_{uu}(\Delta\xi) = \frac{r_{uu}(\Delta\xi; m)}{r_{uu}(0; m)} \quad (2.5)$$

and was averaged over all m . In practice however, these calculations were performed in the frequency domain using periodic extensions of the spatial signals for ease and computational efficiency. The high spatial resolution of 1c-MTV in the y -direction, i.e. $u(y)$, allowed the computation of L_y to be performed relatively easily and was proven to be a robust and

consistent measurement, which is described in Section 3.1.

The computation of FSTI, requires an accurate measure of both U_∞ (a mean quantity) and u_{rms} (the RMS of velocity). Even in measurements with high levels of random uncertainty the mean quantities can still be known with a high degree of certainty (depending on the number of samples). The RMS, however, is significantly higher than the actual value due to the contribution of noise. If the noise is purely random, it may be removed by using the autocorrelation function, as shown in Figure 2.14. Since white noise only correlates with

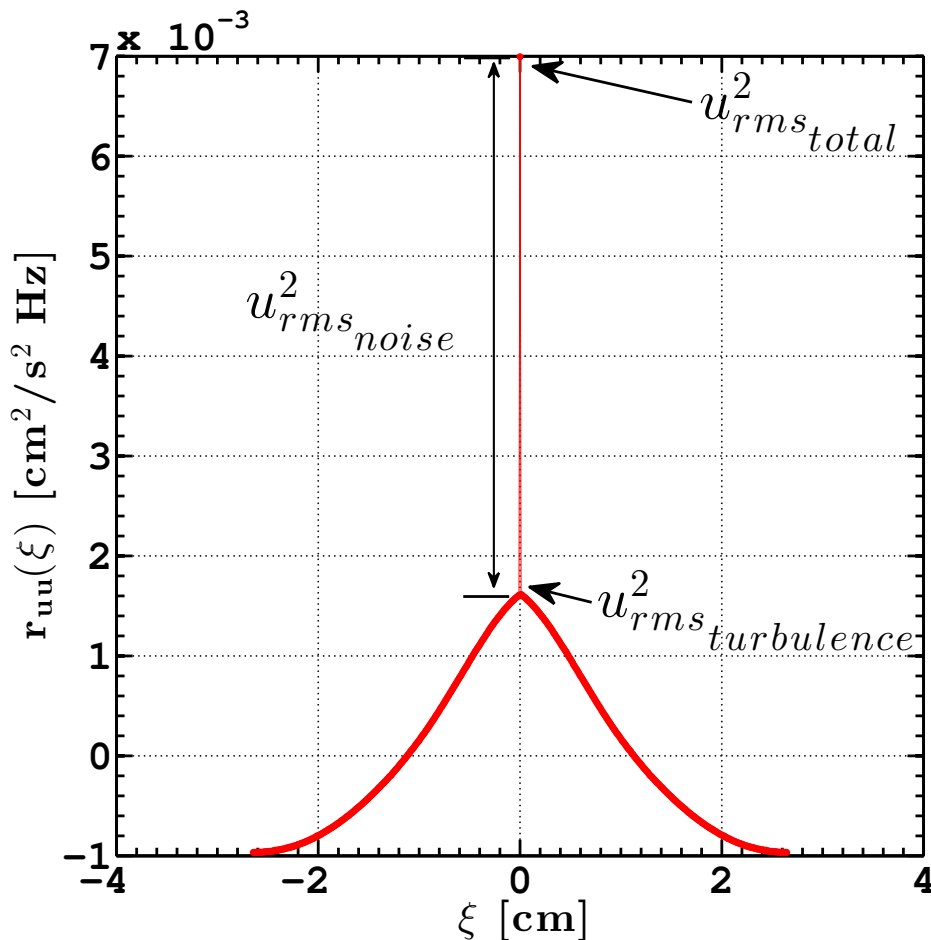


Figure 2.14: The autocorrelation ($r_{uu}(\xi)$) obtained from a single tag line of 1c-MTV data. The autocorrelation function at zero-lag is equal to u_{rms}^2 ($r_{uu}(0) = u_{\text{rms}}^2$) and may be used, as shown, to obtain the fraction of u_{rms}^2 that is due to turbulence only.

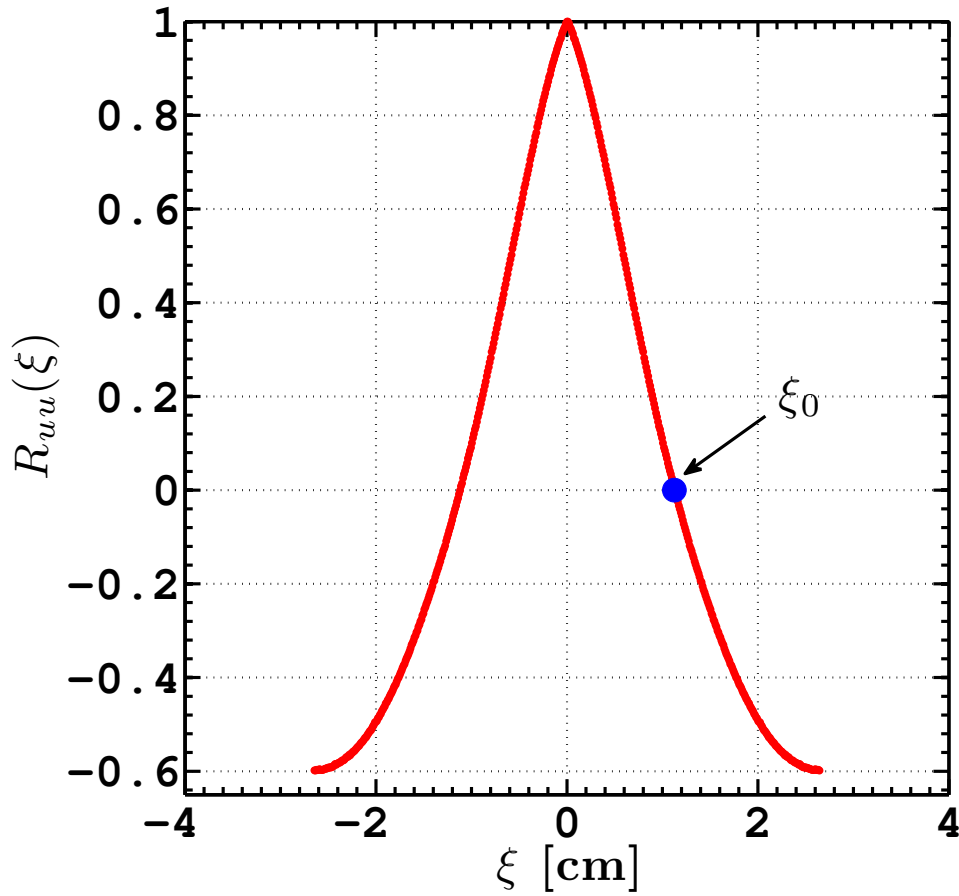


Figure 2.15: The autocorrelation coefficient is shown after the white noise has been removed. The integral length scale, L_y is calculated from this curve by integrating from $\xi = 0$ to ξ_0 .

itself at zero spatial and temporal offset it will only have a non-zero contribution to the autocorrelation at zero offset, i.e. $R_{uu}(0)$. Once removed, a “noise-free” autocorrelation can be obtained, as shown in Figure 2.15, which is used in conjunction with Equation 2.3 for the computation of L_y .

The Power Spectral Density (PSD) is also computed to characterize the freestream data. The PSD is computed from each 300 s time series from a single row of pixels from a single tag line by splitting the time series into 10 records each of length 600 to compute the mean PSD. The overall mean PSD, which is described and shown for both the baseline and flow with increased FSTI in Section 3.1, is the average PSD from all of the rows and tag lines in FOV #11 (see Figure 2.18 for location of FOV).

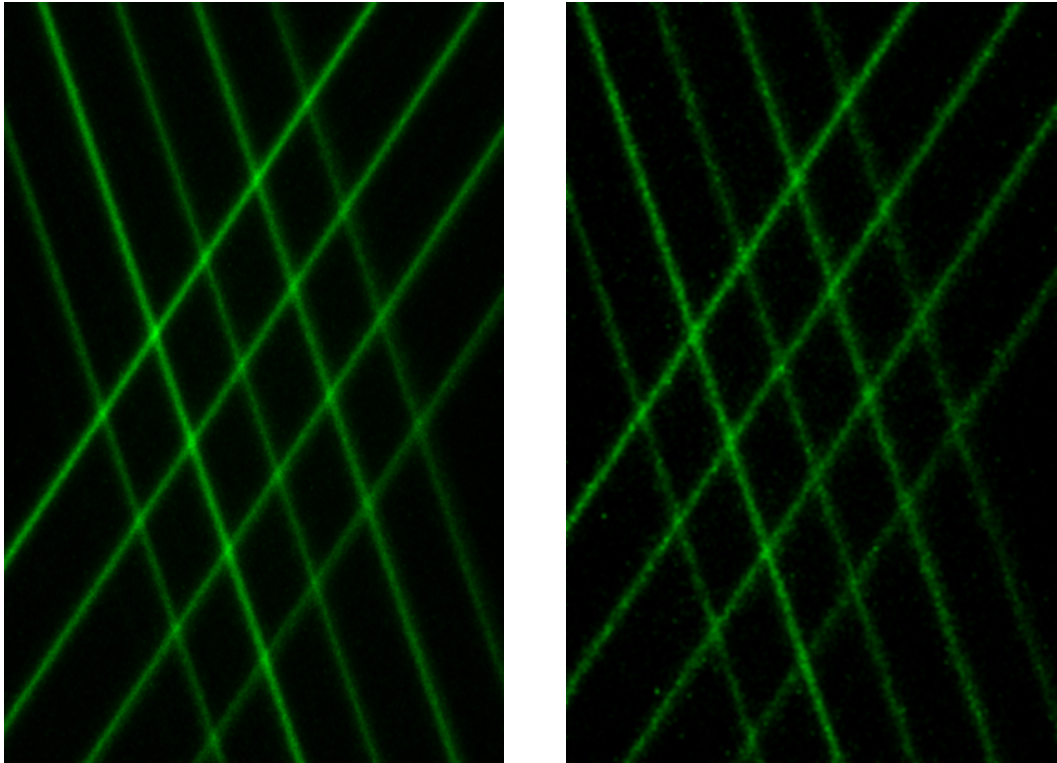
2.4 Data Acquisition

2.4.1 Imaging

The upstream measurement region, located $2c$ upstream of the airfoil, is imaged using a 12 bit 1280×1024 pixel PCO DiCam Pro camera paired with a Micro-Nikkor 105mm f/2.8D lens. This camera is capable of taking two images with a short time delay between images to form the MTV image pair. The first image is acquired at $\sim 3 \mu\text{s}$ after the laser has fired with a 0.7 ms exposure and the second image is acquired 10.7 ms after the beginning of the first image, also with a 0.7 ms exposure. A 336×512 pixel region of the CCD array is used to record the images, this reduces the data size while also increasing the maximum frame rate of the camera.

The images are recorded directly to disk on a 32 bit Windows XP PC using PCO Camware v3.02 and a set of sample instantaneous images are shown in Figure 2.16. The image scale was determined to be 102.6 ± 0.2 px/cm, using a subpixel accurate, 2D cross-correlation routine applied to an image of a target that was placed in the measurement plane. The target, as described in Bohl (2002), consists rectangular intersections of a known spacing.

For each field of view (FOV) in the primary measurement area, a sequence of 1500 image pairs recorded at 5 frames per second, (5 minutes), was taken simultaneously at the upstream location to monitor the approach flow.



(a) Sample Instantaneous Undelayed Freestream Image

(b) Sample Instantaneous Delayed Freestream Image

Figure 2.16: Representative instantaneous undelayed (a) and delayed (b) upstream images. The images are artificially colored and the look up table (LUT) has been adjusted for clarity. Only high quality intersections are used for correlation to ensure the highest possible subpixel accuracy.

The primary measurement region was imaged using a 12bit 1392×1024 pixel PCO Pixelfly QE camera paired with a Nikkor 50mm f/1.2 lens. This camera does not have the capability of recording two images in short succession, therefore, there are no longer individual image pairs but two sequences of images recorded at two different time delays relative to the laser pulse. The first undelayed image sequence is $\sim 30 \mu\text{s}$ after the laser pulse and the second

delayed image sequence, is at $t = t_2$ after the laser pulse, which is typically varied in the range of 0.5 ms - 6.8 ms for different fields of view over the airfoil surface. The FOVs used for computing freestream turbulence characteristics typically used a 12 ms delay. A sample image pair may be seen in Figure 2.17. The time delay and exposure (typically 0.2 ms - 0.8 ms) was optimized for each FOV based on flow conditions to maximize the accuracy of the technique.

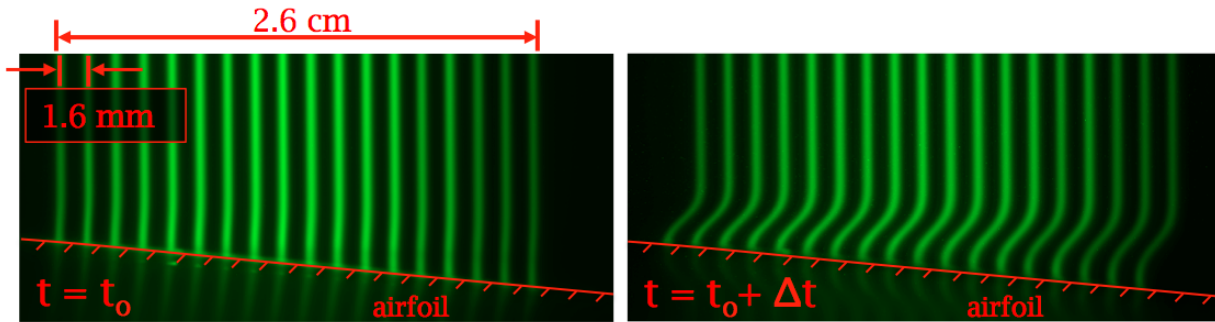


Figure 2.17: Representative average undelayed (left) and average delayed (right) images are shown near where separation occurs. Only $\sim 1/4$ of the height of the image is shown so the shear layer may be seen.

Each FOV in the primary measurement region is $1024\text{px} \times 1392\text{px}$ and contains 19 lines equally spaced at ~ 30 pixels in the streamwise direction with an effective measurement area of $\sim 1024 \times 530$ pixels. The scale factor of this imaging setup is 192.9 ± 0.2 px/cm resulting in an effective measurement region of $2.76 \text{ cm} \times 5.31 \text{ cm}$ or $(137 \text{ mC} \times 528 \text{ mC})$, a line spacing of 0.16 cm or 8 mC , and a cross-stream resolution of $51.8 \mu\text{m}$ or 0.26 mC in the X and Y directions respectively. Each undelayed image sequence contains 500 images recorded at 10 frames per second, which was determined to be sufficient by studying the convergence of the subpixel noise characteristics of correlating the mean image with its instantaneous images. Each delayed image sequence is comprised of 3000 images (also recorded at 10 frames per second for an acquisition time of 5 minutes). In the case of FOVs used for

computing freestream turbulence characteristics, the images are recorded at 20 frames per second by sacrificing the vertical resolution by a factor of 2. The length of time series was determined by Katz (2010) to ensure statistical convergence in the separated shear layer over the same airfoil and under similar flow conditions.

Clearly, at the relatively small size of the field of view needed to obtain high spatial resolution, multiple FOVs are needed to image the entire suction side of the airfoil. This was accomplished using a set of linear traverses along the streamwise and wall normal directions to move the imaging system relative to the test section to image the entire airfoil. The accuracy of the traverse motions were found to be ± 0.008 in. (1 mC) in the streamwise direction and ± 0.004 in. (0.5 mC) in the cross-stream direction. The UV optics are attached to the streamwise traverse such that the camera and tagged fluid region move together. This setup can be seen in the test section schematic seen in Figure 2.2 and the pictures in Figure D.1. A sample shift pattern, showing the relative motion between each FOV is shown in Figure 2.18 for a geometric angle of attack of $\alpha = 8^\circ$.

There are 8 FOVs over the suction side of the airfoil and two additional FOVs to record data immediately upstream and downstream of the airfoil. The two FOVs located above the airfoil (FOV # 11,12) are utilized for turbulence measurements; it was found from CFD simulations and previous experiments that the velocity fluctuations (u' and v') in these regions were representative of freestream conditions (assuming an open separation did not occur). For improved temporal resolution, in these two FOVs the spatial resolution was reduced by a factor of 2 and the acquisition rate increased to 20 Hz to yield 6000 images in the delayed sequence.

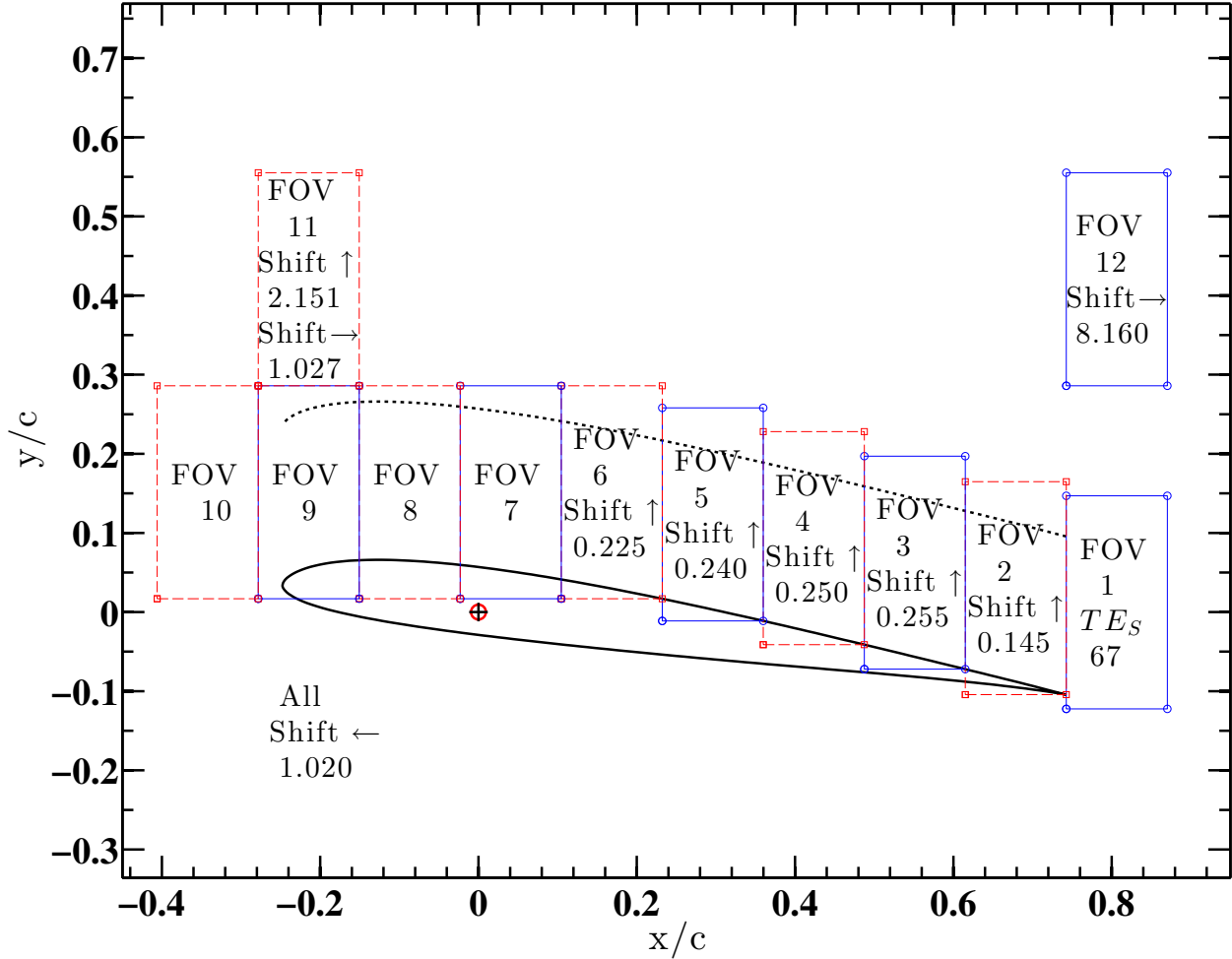


Figure 2.18: The shift diagram for a geometric angle of 8° is shown. All units are in inches unless noted. All shifts to the left are 1.020 in. The dotted line represents the airfoil profile 0.20c above the surface, beneath which (in all but a few cases), all of the interesting flow features are contained. The TE_s in FOV #1 indicates the height of the trailing edge, in pixels, from the bottom of the image to ensure the chordline, if extended past the trailing edge, is still imaged on the right hand side of the image.

2.4.2 Image Processing

The upstream measurements (2c-MTV) are processed using in-house processing programs previously developed and described in detail in Gendrich and Koochesfahani (1996). The 1c-MTV data is also processed using an in-house processing program described in Katz (2010). As part of the current work, the 1c-MTV code has since undergone a significant amount of optimization and parallelization to allow all of the current experiments to be completely processed in a reasonable amount of time. The speed of the original processing code was ~ 230 displacement vectors per second (referred to as nodes/second). After the initial parallelization and speed enhancements it was capable of 730 nodes/second on dual-core machines. After sufficient performance testing, two Apple Mac Pro machines with (2) 6-core 2.66 GHz Intel Xeon 5650 processors and 12 GB of 1333 MHz ECC RAM were purchased for data processing. Additional optimizations were made to take advantage of the new machines which are capable of processing at $\sim 20,000$ nodes/second. Using the original code, processing the data would have taken $\sim 11,000$ hours (~ 150 weeks), whereas with the new processing code it was reduced to ~ 300 hours or just under 2 weeks.

In the current experiments, the undelayed and delayed 1c-MTV images are not acquired from the same laser pulse (i.e. the molecules tagged in the first image are not the same as those in the second). The average of the undelayed images is correlated to each instantaneous delayed image to form image pairs. This technique is acceptable if the fluid can be assumed to be steady over the exposure time period of the first image and laser jitter is small. Any deviation from steady flow (or changes in tag line location) will manifest as an increase in the RMS of the mean flow. This increase in RMS associated with this technique may be estimated by examining the correlations of the mean undelayed image with each instanta-

neous undelayed image. If all of the assumptions made above are correct and there is no noise due to processing, both the mean and displacement RMS should be zero. The mean will be non-zero if there is an asymmetric distribution in the displacement fluctuations. The displacement RMS is however, non-zero and serves as an estimate for the combined effect of both the processing noise and due to correlating the average undelayed image to each instantaneous delayed image.

The data presented have been remapped onto a regularly spaced grid, with an x and y spacing approximately equivalent to the original data spacing to facilitate plotting. The u_{rms} has been spatially filtered along the tag line in order to remove noisy pixels. The filter uses the deviation from the local mean to identify bad pixels and replaces it with a linear interpolation of the region. In general, less than 20 pixels per line ($< 3\%$) were modified. The spatially non-uniform background u_{rms}^2 has been removed from the data as well. This was necessary to account for large variations in SNR across a FOV. There is virtually no difference in the background u_{rms}^2 values subtracted between the baseline and increased FSTI cases and therefore, does not impact any conclusions regarding the effect of FSTI of either \bar{u} or u_{rms} .

2.4.3 Alignment and Synchronization

The alignment of the two different imaging systems, the stationary upstream DiCamPro and the translating Pixelfy QE, was achieved by directing the beam of a HeNe Laser through the end view of the test section such that it passed through both camera's FOV in the measurement plane. The scatter of the HeNe beam produces images of a straight line passing through the entire FOV. The angle of this line relative to each camera's pixel coordinates

is found, providing the rotational alignment required between the imaging systems. The alignment of translational axis of the imaging system and the bottom of the tunnel was determined with an accuracy of $\pm 0.03^\circ$ by correlating the images of an object placed on the bottom of tunnel at two different positions to find the vertical displacement for a known travel distance of the imaging system.

The synchronization of the two different imaging systems and laser was achieved using two Stanford Research Systems DG535 Digital Delay Generators as indicated in the hardware diagram in Figure 2.19 and the timing diagram in Figure 2.20.

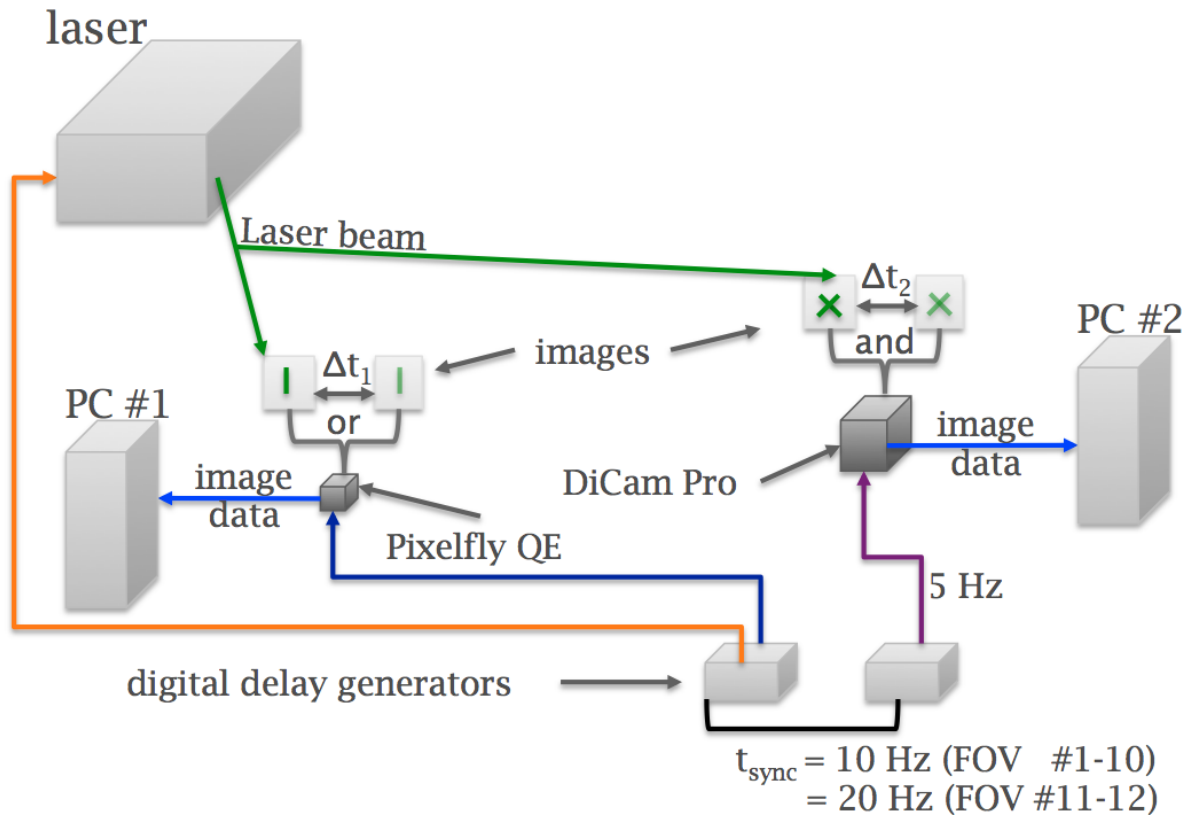


Figure 2.19: The diagram above indicates the hardware, synchronization, and data flow for the current experiments. The first digital delay generator provides the sync signal to the second delay generator and triggers the laser and Pixelfly Camera at 10 or 20 Hz depending on the FOV. The Pixelfly either records the first or second image which are Δt_1 apart and sends the images to PC #1 where it is written to hard disk. The second digital delay generator uses this sync signal and outputs a 5 Hz signal to the DiCam Pro, which records two images (Δt_2 apart) and sends the images to PC #2 where it is written to hard disk. Both PC #1 and PC #2 use Camware v3.02 provided by PCO to control and record images.

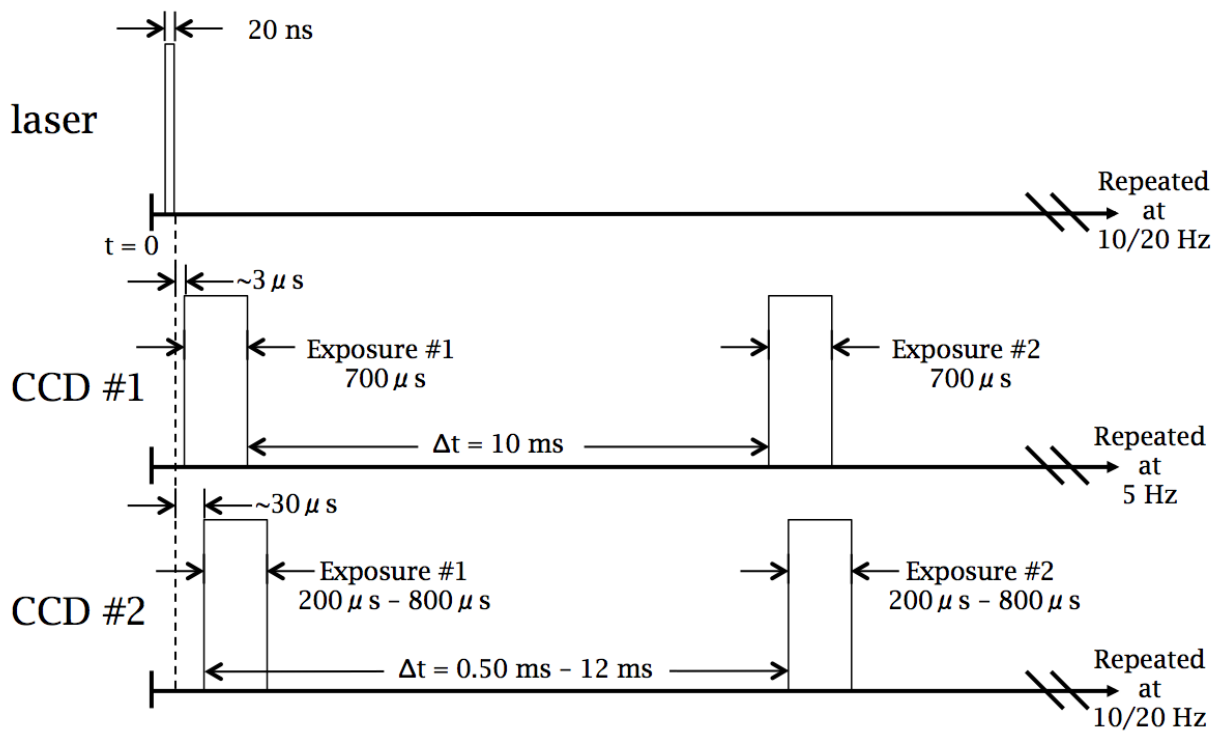


Figure 2.20: The timing diagrams of the experiments (not to scale). It should be noted that CCD # 2, the Pixelfly QE, only records one exposure at a time, the second exposure is recorded during a different sequence of images.

2.5 Experiments

2.5.1 Experimental Parameters

The chord Reynolds number and angle of attack for both the baseline and increased FSTI configuration for each case in the current study are listed in Table 2.1. The chord Reynolds numbers shown are mostly slightly less than the objective: 20,000, 30,000 and 40,000, because the airfoil was originally thought to be 8.000 in., but was later found to be 7.959 in. from the laser scanning measurements. And, although extreme care was taken to ensure the angles of attack would be very close to other experimental and computational studies (i.e. 2, 4, 6, 8, and 12 degrees), a minor issue was uncovered after the experiments had been performed leading to the geometric angles of attack listed (relative to the bottom of the tunnel). Data were also taken at a Reynolds number of 60,000 but has been excluded since only the baseline case was performed.

2.5.2 Experimental Procedure

The time required to take all 12 FOVs for each case angle of attack was approximately 2 hours, which permitted a single Reynolds number (for either the baseline or increased FSTI) to be studied in each day of data taking. As described previously, the day-to-day fluctuations of the tunnel operating parameters were monitored and taken into consideration. The typical procedure used for conducting the experiments is given in Appendix D.3. The total hard disk space required for each case, a single angle of attack for a single Reynolds number for a single freestream condition, after processing is ~ 180 GB, for a total size of 5.4 TB for all of the experiments.

Baseline		Increased FSTI	
Re_c	Geometric α	Re_c	Geometric α
20120 ± 40	0.5 ± 0.1	19720 ± 60	-0.3 ± 0.3
19880 ± 20	2.5 ± 0.1	19780 ± 20	1.5 ± 0.2
19940 ± 60	4.5 ± 0.2	19800 ± 80	3.5 ± 0.2
19900 ± 120	6.1 ± 0.1	19820 ± 80	5.8 ± 0.1
19900 ± 80	10.0 ± 0.2	19780 ± 60	10.0 ± 0.1
29740 ± 60	0.5 ± 0.2	29820 ± 60	0.7 ± 0.1
29760 ± 120	2.3 ± 0.1	29820 ± 120	2.4 ± 0.1
29760 ± 40	4.4 ± 0.0	29860 ± 100	4.6 ± 0.0
29820 ± 140	6.4 ± 0.1	29900 ± 100	6.4 ± 0.0
29820 ± 60	10.7 ± 0.1	29900 ± 120	10.6 ± 0.1
39340 ± 240	0.4 ± 0.1	39740 ± 20	0.4 ± 0.1
39420 ± 300	2.4 ± 0.0	39900 ± 240	2.4 ± 0.1
39280 ± 140	4.6 ± 0.1	39840 ± 100	4.5 ± 0.2
39300 ± 20	6.8 ± 0.1	39840 ± 60	6.6 ± 0.1
39360 ± 100	10.8 ± 0.1	39800 ± 60	10.7 ± 0.1

Table 2.1: The Reynolds number and angle of attack for each case studied is shown in the table with the uncertainty of each value. The freestream velocity for each of the three Reynolds number shown above are approximately: 9.3 cm/s, 14.2 cm/s, and 18.3 cm/s.

Chapter 3

Results and Discussion

3.1 Freestream Turbulence Characteristics

The velocity fluctuations in the freestream of the water tunnel facility is predominately produced by very low frequency oscillations ($f < 0.2$ Hz) which may be seen in the power spectral density (PSD) in Figure 3.1a. These frequencies are suspected to be from ‘U-Tube’ oscillations that develop and are allowed to propagate due to the exposed free surface along the entire length of the tunnel (as discussed in Katz (2010)). These oscillations manifest in the test section as spatially uniform velocity fluctuations of very low frequencies.

Fluctuations of this type may, however, be removed by subtracting the spatial mean velocity at each instance in time. The spectra for both the baseline and increased FSTI configurations are shown in Figure 3.1b after the spatial mean was removed. The removal of the spatial mean is warranted for two reasons: (1) to characterize the broadband ‘random’ fluctuations in both space and time (i.e. what is typically considered turbulence); (2) it is hypothesized that these very low frequencies do not significantly influence the flow physics of

separation and reattachment, and should simply be considered as a fluctuation in Reynolds number rather than an increased turbulence level. It is not, however, possible from the current experiments to completely determine if this hypothesis is correct and should be considered for future work.

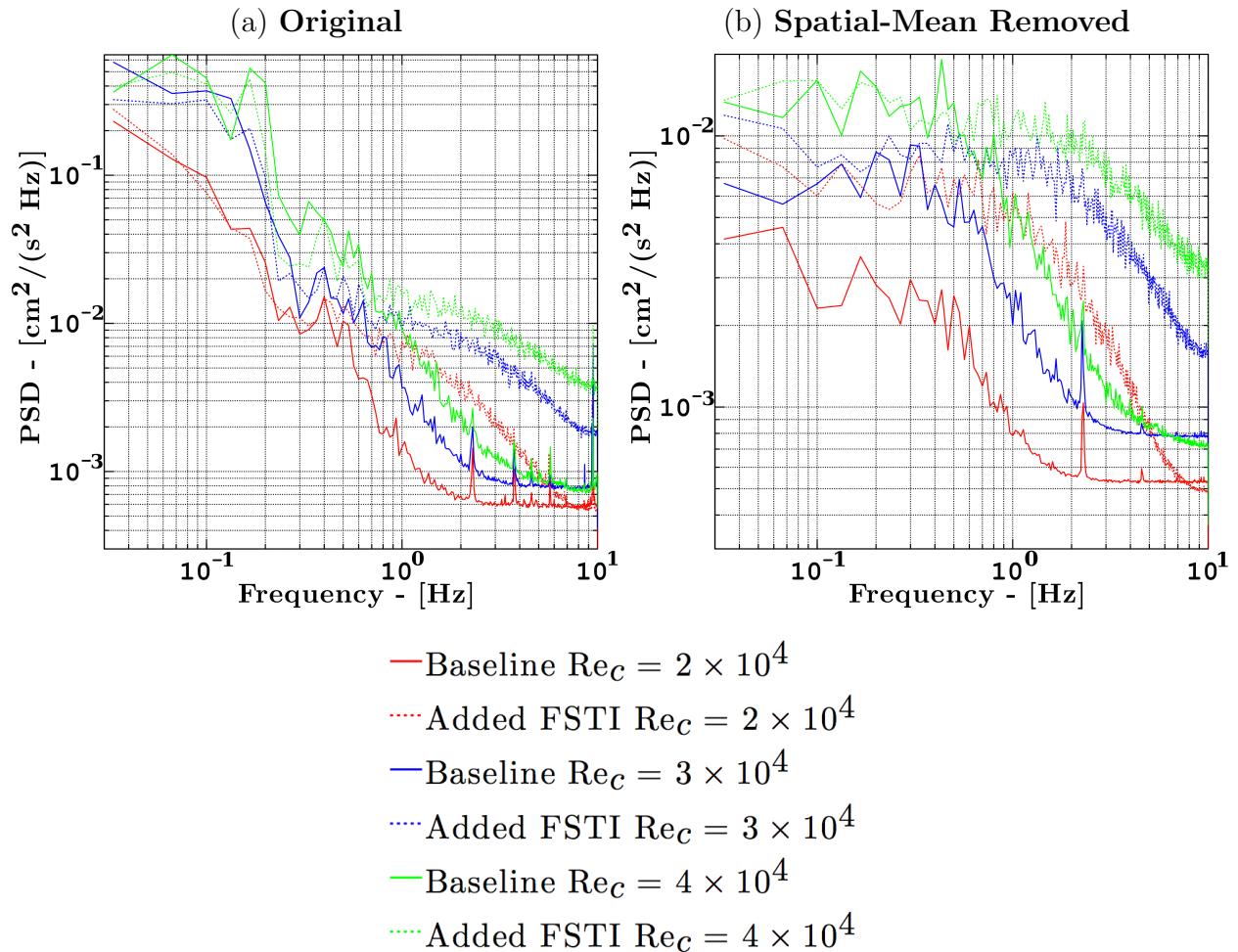


Figure 3.1: The original (a) and spatial-mean removed (b) freestream power spectral density (PSD) for each Reynolds number and configuration. The baseline configuration is represented by solid lines and dashed lines represent the increased FSTI configuration in both plots. The color of the line corresponds to the Reynolds number. The PSD is computed from the average of 12, 500-point records of the time series from each pixel of each line.

The addition of the woven mesh grid increases the freestream turbulence for all Reynolds numbers but its influence on the spectra changes as a function of Reynolds number. The influence of the grid at low frequencies degrades as the Reynolds number increases while the impact on high frequencies increases with an increasing Reynolds number. A more detailed comparison of the spectra at each Reynolds number may be found in Appendix A.

The turbulence characteristics described in Section 2.3, L_y and FSTI, are calculated from the spatial mean removed velocity data for each case in the current study. The FSTI and L_y for both the baseline and increased FSTI configurations are compared in Table 3.1 for each Reynolds number. The value shown is the mean computed from ~ 15 tag lines in FOV # 11 for each angle of attack (approximately 75 samples in total). The uncertainty listed as the RMS of those 75 samples. For reference, the FSTI computed from the raw time series at $Re_c = 2 \times 10^4$ is 1.82% (baseline) and 2.15% (increased FSTI configuration).

Table 3.1: Freestream Characteristics

Re_c	Baseline		Increased FSTI	
	FSTI [%]	L_y [cm]	FSTI [%]	L_y [cm]
2×10^4	0.45 ± 0.04	0.59 ± 0.01	1.43 ± 0.03	0.44 ± 0.01
3×10^4	0.52 ± 0.01	0.53 ± 0.02	1.23 ± 0.01	0.38 ± 0.01
4×10^4	0.65 ± 0.03	0.48 ± 0.01	1.29 ± 0.02	0.36 ± 0.01

There is little variation in both the FSTI and L_y for different angles of attack (α). This provides confidence in the flow facility and its ability to provide repeatable boundary conditions since the minimum time between measurements was ~ 3 hours and some were as much as 24 hours. With this confidence, changes in LSB characteristics should be correlated to the addition of the mesh screen, and not day-to-day changes in the flow facility.

In the baseline configuration, the FSTI increases slightly with increased tunnel speed. The

integral length scale however, decreases slightly with increased tunnel speed. The presence of the grid increases the FSTI of the tunnel by a factor of $\sim 2 - 3$ and decreases the integral length scale by $\sim 25\%$. The Reynolds number dependencies, described above for the baseline configuration, are reduced by the presence of the grid.

The freestream turbulence characteristics presented in this section provide a complete description of how the freestream was modified by the grid.

3.2 Representative Results

3.2.1 Streamwise Velocity Contours: Mean and Fluctuation

Representative contours of the mean streamwise velocity and streamwise velocity RMS are described in this section. The separation location is defined with respect to the mean flow field as the surface location above which the sign of the velocity reverses from positive to negative in the data closest to the wall. Similarly, the reattachment location is defined with respect to the mean flow field as the location where the sign of the velocity reverses from negative to positive. The determination of separation and reattachment from the data is described in more detail in the next section. All colormaps shown of the mean streamwise velocity utilize the same color scale of $-0.18 \leq \frac{\bar{u}}{U_\infty} \leq 1.74$ with any velocities above or below these values are saturated. There is a step change at $\frac{\bar{u}}{U_\infty} = 0$, such that all negative velocities are pink to facilitate the identification reversed flow.

The primary features of interest in the mean streamwise velocity contour shown in Figure 3.2 are the separation and reattachment locations, which are indicated. The length and height of the reversed flow region changes with both Reynolds number and angle of attack.

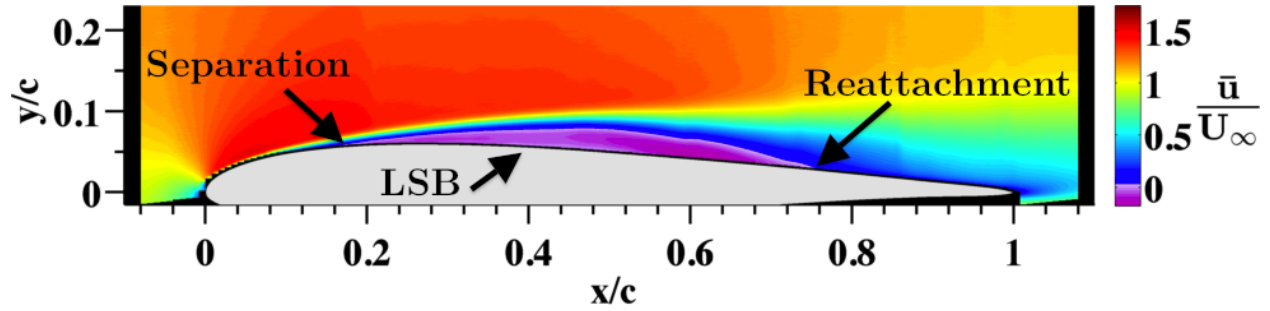


Figure 3.2: A representative mean streamwise velocity contour at $Re_c = 2 \times 10^4$ and $\alpha = 6.1^\circ$. Separation, reattachment, and the laminar separation bubble has been indicated. The pink to purple colors represent reversed flow.

The primary features of interest in Figure 3.3 are the long slender region of gradually increasing u_{rms} in the separated shear layer and its abrupt increase in height, quickly extending back to the surface of the airfoil, after which the flow becomes highly unsteady characterized by a non-canonical boundary layer underneath the unsteady flow structure emerging from the separated region.

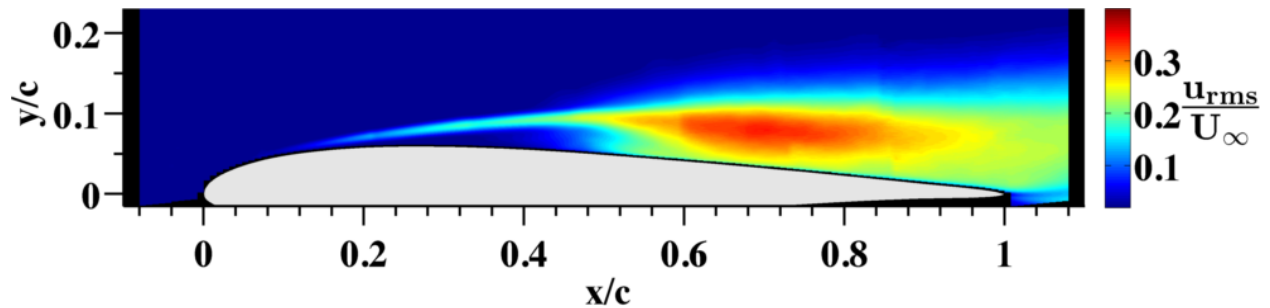


Figure 3.3: A representative contour plot of the RMS streamwise velocity at $Re_c = 2 \times 10^4$ and $\alpha = 6.1^\circ$. The primary feature of the u_{rms} is a long thin region of increased u_{rms} initially tracking the separated shear layer and gradually increasing in magnitude. At some downstream location, the thin band of increased u_{rms} extends from the separated shear layer to the surface; downstream of which an elongated region of much higher u_{rms} is found and gradually decreases in magnitude along the x-direction.

The slight discontinuities in the \bar{u} or u_{rms} contour plots (as seen in Figures 3.3 and 3.2 and others) may be attributed to the following: uncertainties or error in FOV alignment, the

accuracy of the laser sheet alignment relative to the CCD array, optical distortions, changes in laser sheet location (quantified to cause $< 1\%$ spatial non-uniformity in magnification), and slight changes in flow from the time one FOV is recorded to the next. In the distribution of u_{rms} , the spatial non-uniformity of the signal to noise ratio (SNR) also contributes to the discontinuity of the results. Although corrective measures were implemented (see Section 2.4.2) to account for most spatial non-uniformity in u_{rms} , clearly, some may still exist.

3.2.2 Separation and Reattachment

As discussed previously, separation is determined by locating flow reversal at the first available velocity data above the surface in the mean flow. In this study, due to near wall imaging issues, the first 4 or 5 pixels (1.0 - 1.3 mC) above the wall are excluded. It was shown in Olson et al. (2011) from computational results at $Re_c = 4 \times 10^4$ and $\alpha = 4^\circ$ that excluding the first 2 mC of data above the surface, separation would be improperly identified 100 mC farther downstream than its actual location as determined by the closet computational point above the surface. The growth in height of the reversed flow above the surface is nearly linear for this simulation, and therefore, it is reasonable to estimate that by excluding 1 mC of above the surface, separation would be identified ~ 50 mC farther downstream than its actual value. Clearly, since this analysis was performed only at $Re_c = 4 \times 10^4$ and $\alpha = 4^\circ$, this conclusion relies on the shape of the separated bubble to be uniform across both Re_c and α , and also assumes the shape of the bubble in these simulations is the same as experiments, which is generally not the case. It does however, yield a useful estimate of the bias introduced by using velocity vectors 1 mC above the surface of the airfoil.

Another possible alternative for estimating both the actual separation point and/or the

error by excluding the near wall region is by following the change in sign of velocity as a function of both x/c and y/c and extrapolating this locus to the surface. This may be visualized in Figure 3.4 by following the dark band (i.e. zero velocity) above the clearly reversed region in the upstream direction and locating its intersection with the surface. This technique has been proposed for future work. The shape of the reversed flow region near reattachment is typically not as sensitive to this issue but, a bias does still exist. Its magnitude however, should be less and results in identifying reattachment farther upstream than its actual location.

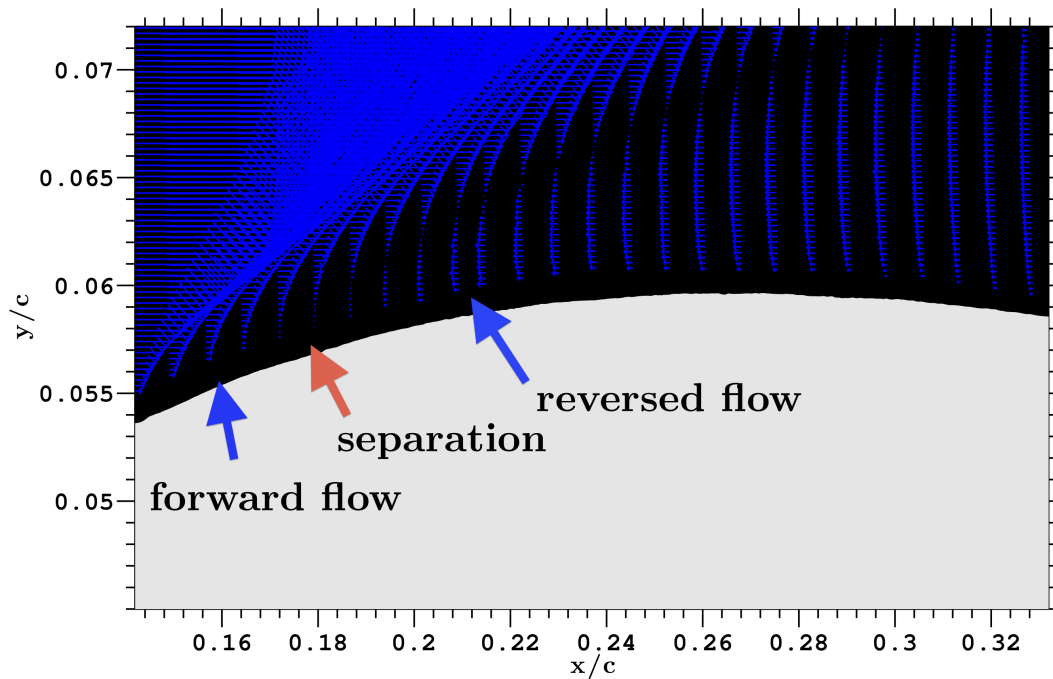


Figure 3.4: Representative view of separation for the baseline configuration, $Re_c = 2 \times 10^4$, and $\alpha = 6.1^\circ$ (not to scale). The regions of clearly forward and reversed flow are indicated. The separation location is $x/c = 0.18 \pm 0.02$.

The process of determining separation is depicted in Figure 3.4 with the regions of the flow that are “clearly forward”, and “clearly reversed” indicated. Separation must occur between these two regions and is recorded as midpoint between the first “clearly forward” velocity vector and the first “clearly reversed” vector. The uncertainty is listed as the distance between these two clearly defined regions, which is typically 1 or 2 line spacings (8 mC or 16 mC). The same procedure is used for determining the reattachment location as shown in Figure 3.5.

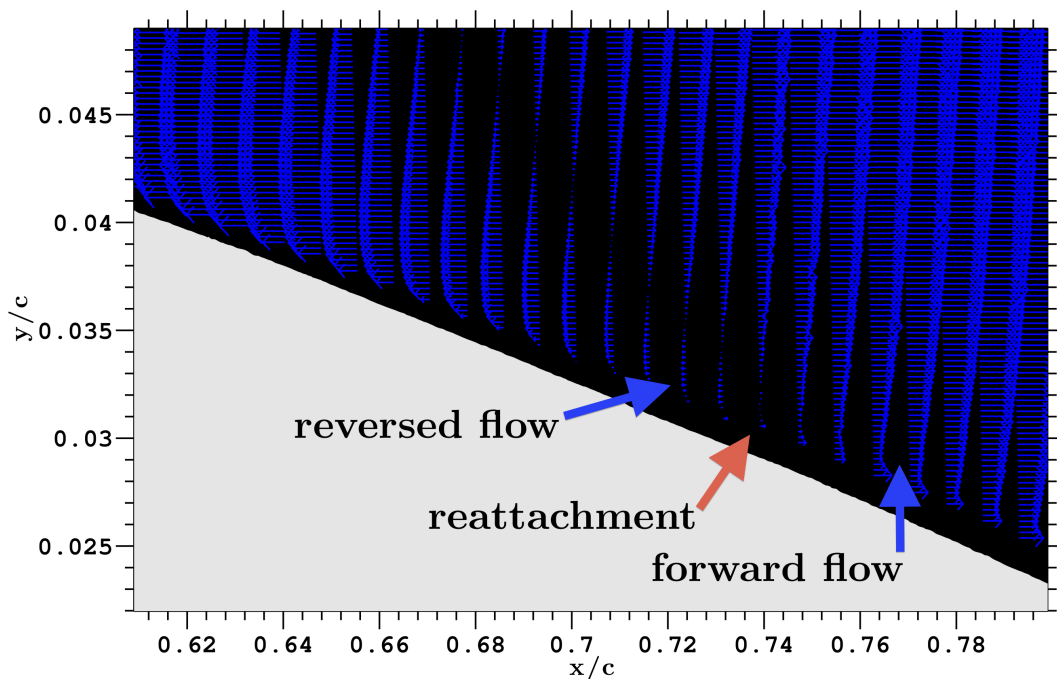


Figure 3.5: Representative view of reattachment for the baseline configuration, $Re_c = 2 \times 10^4$, and $\alpha = 6.1^\circ$ (not to scale). The regions of clearly forward and reversed flow are indicated. The reattachment location is $x/c = 0.74 \pm 0.02$

3.3 Characterizing the Laminar Separation Bubble

In this section the influences of increased freestream turbulence intensity, Reynolds number, and angle of attack, on the laminar separation bubble are discussed. The effects of these parameters on separation location, reattachment location, and the overall bubble length are presented with the primary focus on the influence of FSTI. Most effects are discussed qualitatively, but separation and reattachment location are quantitatively compared, when available in the literature, between the baseline and increased FSTI configurations as well as other experiments and computations.

3.3.1 Influence of Added Freestream Turbulence

Qualitatively, the influence of increased freestream turbulence intensity on the mean flow has the effect of suppressing the laminar separation bubble: separation moves downstream and reattachment moves upstream making the bubble shorter in length and thinner in height. This effect can be seen across all Reynolds numbers studied and all angles of attack, although its extent reduced at both high and low angles. These effects can be seen by comparing the mean streamwise velocity shown in Figure 3.6 for both the baseline and increased FSTI configuration for $Re_C = 3 \times 10^4$ and $\alpha = 6.4^\circ$. The reversed flow region in the baseline case is clearly visible, while in the increased FSTI case the reversed flow region is barely visible at this scale. Quantitative results for all other cases are presented later in Section 3.4.1 and the contours of mean and RMS for all cases are provided in Appendix B.

In some cases, the increased FSTI configuration is drastically different from the baseline configuration as seen at $Re_C = 2 \times 10^4$ and $\alpha = 10.0^\circ$ in Figure 3.7. At these conditions the baseline case is characterized by an open separation, i.e. the flow has a fully separated shear

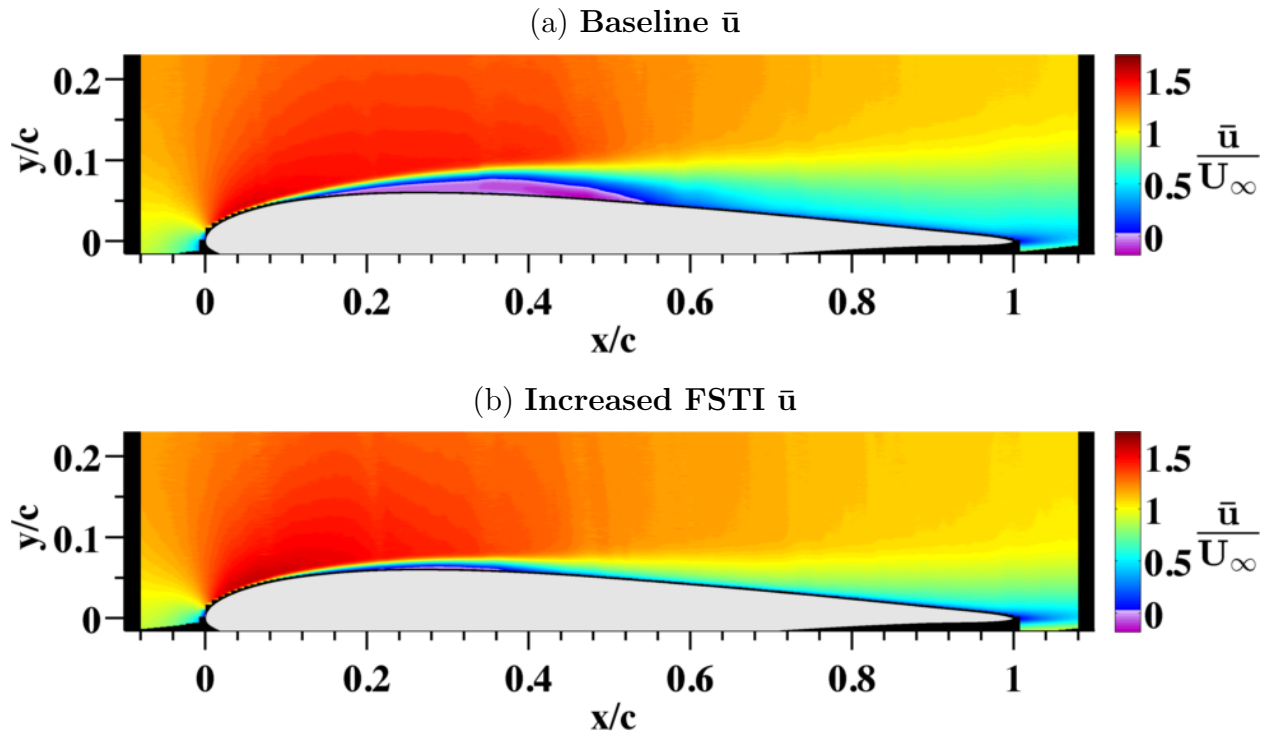


Figure 3.6: The mean flow is compared for the baseline (top) and increased FSTI (bottom) configuration at $Re_c = 3 \times 10^4$ and $\alpha = 6.4^\circ$. In the increased FSTI configuration, separation has been delayed, reattachment occurs earlier, the reversed flow region is shorter in length, and is much thinner in height (barely visible at this resolution).

layer which does not reattach over the surface of the airfoil (the flow is much more indicative of a leading edge separation/stall). On the other hand, the flow with increased FSTI has clearly defined closed separation bubble. This observation indicates increased FSTI may delay stall.

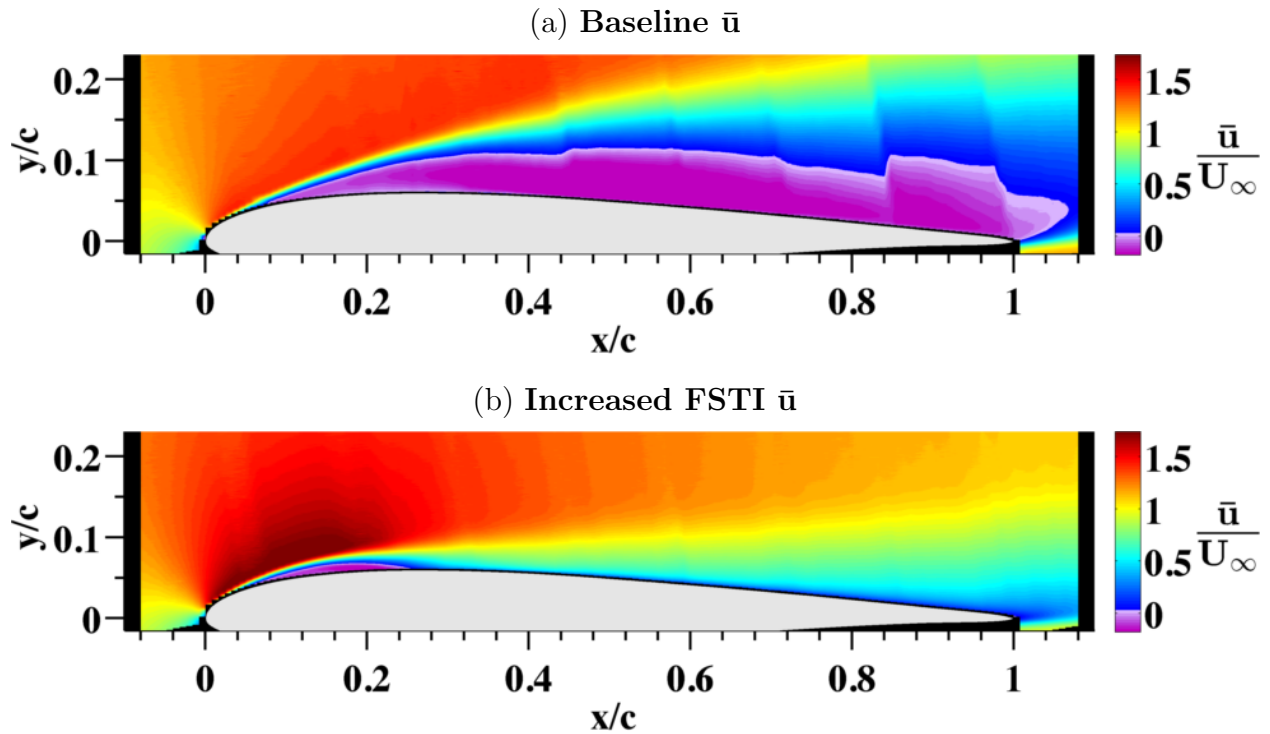


Figure 3.7: The mean flow is compared for the baseline (top) and increased FSTI (bottom) configuration at $Re_c = 2 \times 10^4$ and $\alpha = 10^\circ$. The baseline flow is indicative of stall whereas the flow with increased FSTI the has a well behaved LSB.

Figure 3.8 compares the baseline flow to the flow with increased FSTI at $Re_c = 4 \times 10^4$ and $\alpha \approx 6.7^\circ$. At these conditions, the LSB has been suppressed to the point where it can no longer be detected in the flow with increased FSTI. This may either be because there is no longer a reversed flow in the mean, or the current near wall spatial resolution is not high enough to detect the reversed flow.

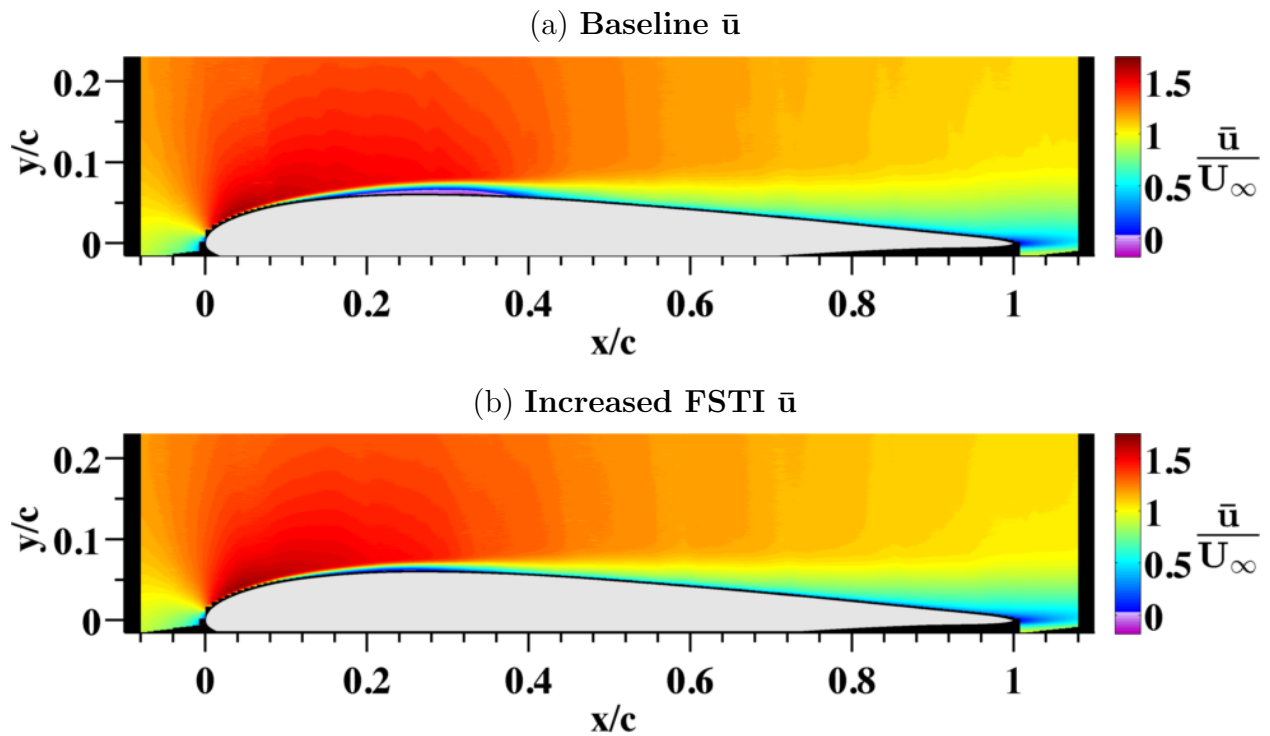


Figure 3.8: The mean flow is compared for the baseline (top) and increased FSTI (bottom) configuration at $Re_c = 4 \times 10^4$ and $\alpha \approx 6.7^\circ$. The baseline flow has a thin, but clearly defined separation bubble whereas there is no reverse flow detected in the case with increased FSTI.

In general, however, the contours of the RMS for both baseline and increased FSTI have similar features for these conditions however, as seen in Figure 3.9. The location of peak RMS occurs farther upstream for the increased FSTI case and the thin band of increased RMS extending upstream from the peak occurs closer to the surface. These observations may also be seen when at other conditions when reversed flow is detected in both configurations. This may support the argument for the reversed flow region has simply become too thin to detect, or, as observed in this case by examining instantaneous results (not depicted), the flow experiences periods in which there is a well defined reversed flow region, that is not seen in the mean velocity.

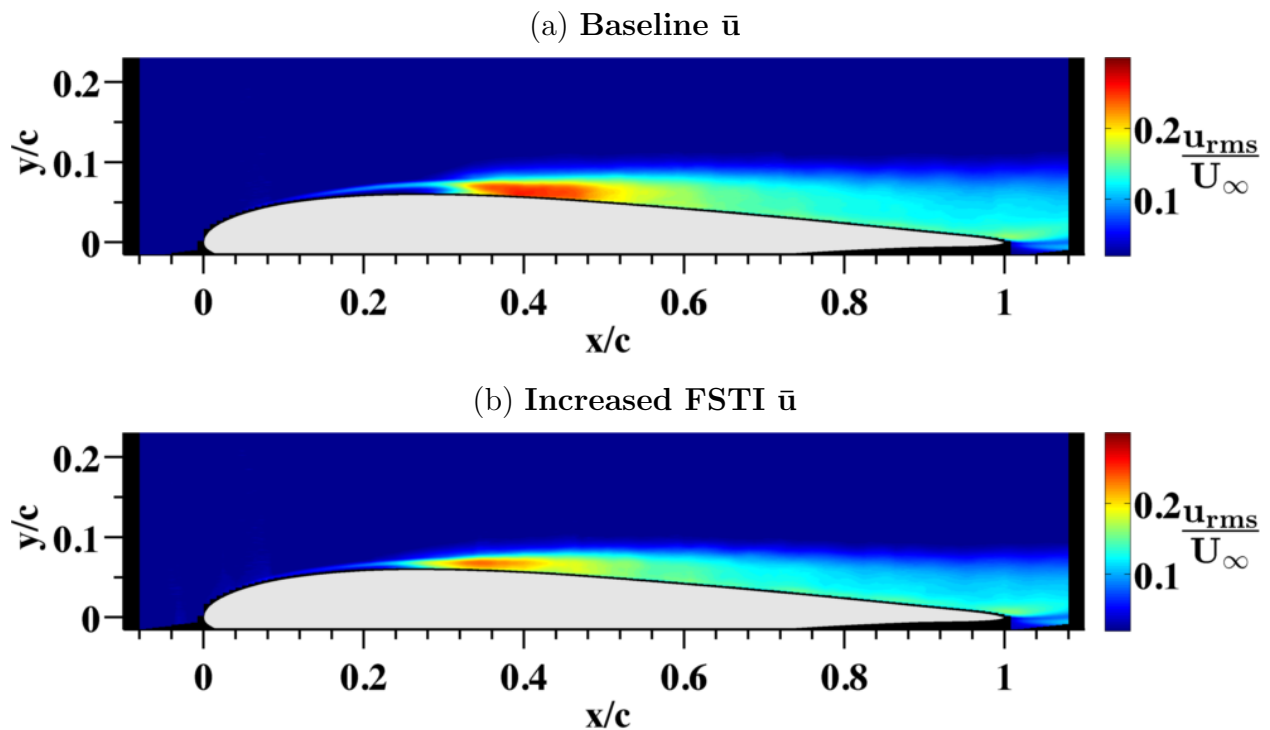


Figure 3.9: The streamwise fluctuations are compared for the baseline (top) and increased FSTI (bottom) configuration for $Re_c = 4 \times 10^4$ and $\alpha \approx 6.7^\circ$. Both contours are qualitatively similar even though there is no reversed flow detected in the increased FSTI configuration.

Increased freestream turbulence intensity also has the qualitative effect of decreasing streamwise velocity fluctuation (u_{rms}) in the separated shear layer and near reattachment. The flow downstream of reattachment is also characterized by a lower u_{rms} . This may be seen by comparing the contour maps of u_{rms} at $\text{Re}_c = 3 \times 10^4$ and $\alpha = 6.4^\circ$ in Figure 3.10.

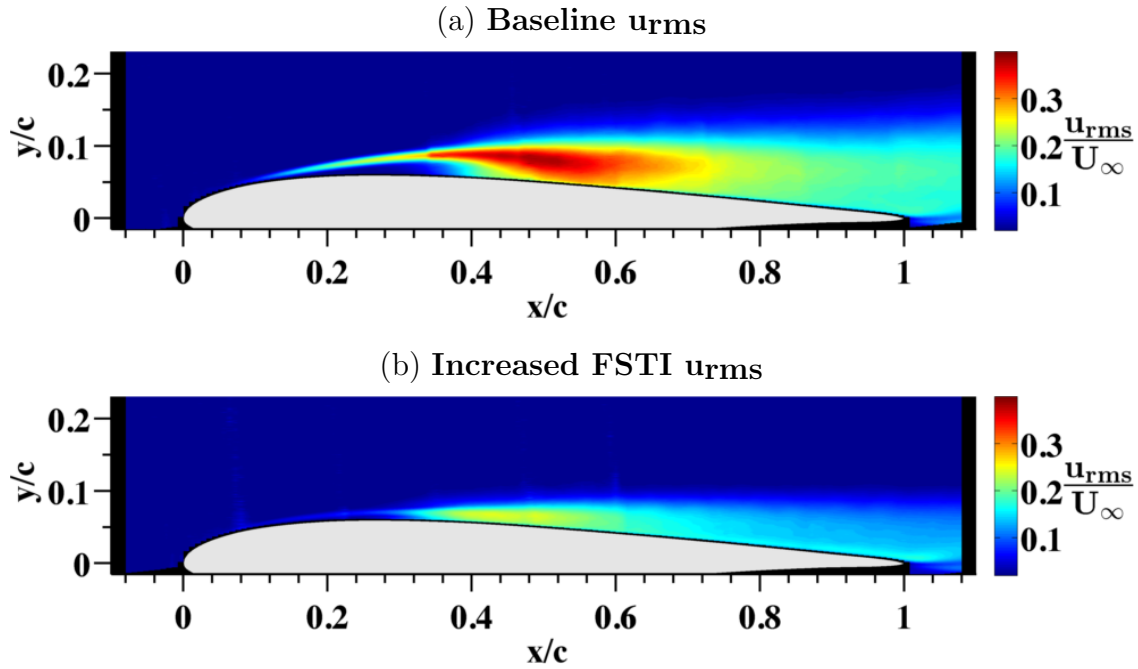


Figure 3.10: The streamwise fluctuations are compared for the baseline (top) and increased FSTI (bottom) configuration for $\text{Re}_c = 3 \times 10^4$ and $\alpha = 6.4^\circ$. The primary effect of increased FSTI is the overall reduction in u_{rms} , indicating a more ‘gentle’ reattachment process.

The bias error in determining the separation and reattachment location discussed in Section 3.2.2 regarding near-wall spatial resolution, has the tendency of shortening the LSB due to delayed detection of separation and an early identification of reattachment. The bias is also inversely proportional to the height of reversed flow region, which increased FSTI decreases, so the bias error is expected to be higher in the increased FSTI configuration than the baseline. Quantification of the bias error for both baseline and increased FSTI configuration should be suggested for future work.

3.3.2 Influence of Angle of Attack

Typically, as the angle of attack of an airfoil is increased, the peak adverse pressure gradient increases in magnitude and also moves upstream. At the low Reynolds numbers of the current study, laminar separation is dictated by the adverse pressure gradient, and is expected to also move upstream as the angle of attack is increased. This trend is observed in the current experiments for both the baseline and flow with added freestream turbulence. The evolution of the flow field as a function of angle of attack for the baseline configuration and a Reynolds number of 3×10^4 is shown in Figure 3.11, all other cases and configurations may be found in Appendix B.1. As the angle of attack is increased the peak streamwise velocity increases and the separation bubble increases in height as it moves upstream.

3.3.3 Influence of Reynolds Number

The primary effect of the Reynolds number can be seen as a thinning of the reversed flow region i.e. the LSB is shorter in height as Re_c increases. Additionally, the separation location moves downstream slightly, and reattachment occurs farther upstream. This effect is seen equally in both the baseline and increased FSTI configurations. The baseline cases at $\alpha \approx 2.4^\circ$ are shown in Figure 3.12. At high angles of attack (such as $\sim 10^\circ$ as shown for both configurations in Appendix B.3), the separation location is not significantly impacted by the Reynolds number, but the LSB becomes shorter (by the reattachment location moving upstream) and thinner with increasing Re_c . The Reynolds number is also very important in determining the bubble length, which may be seen later in Figure 3.16.

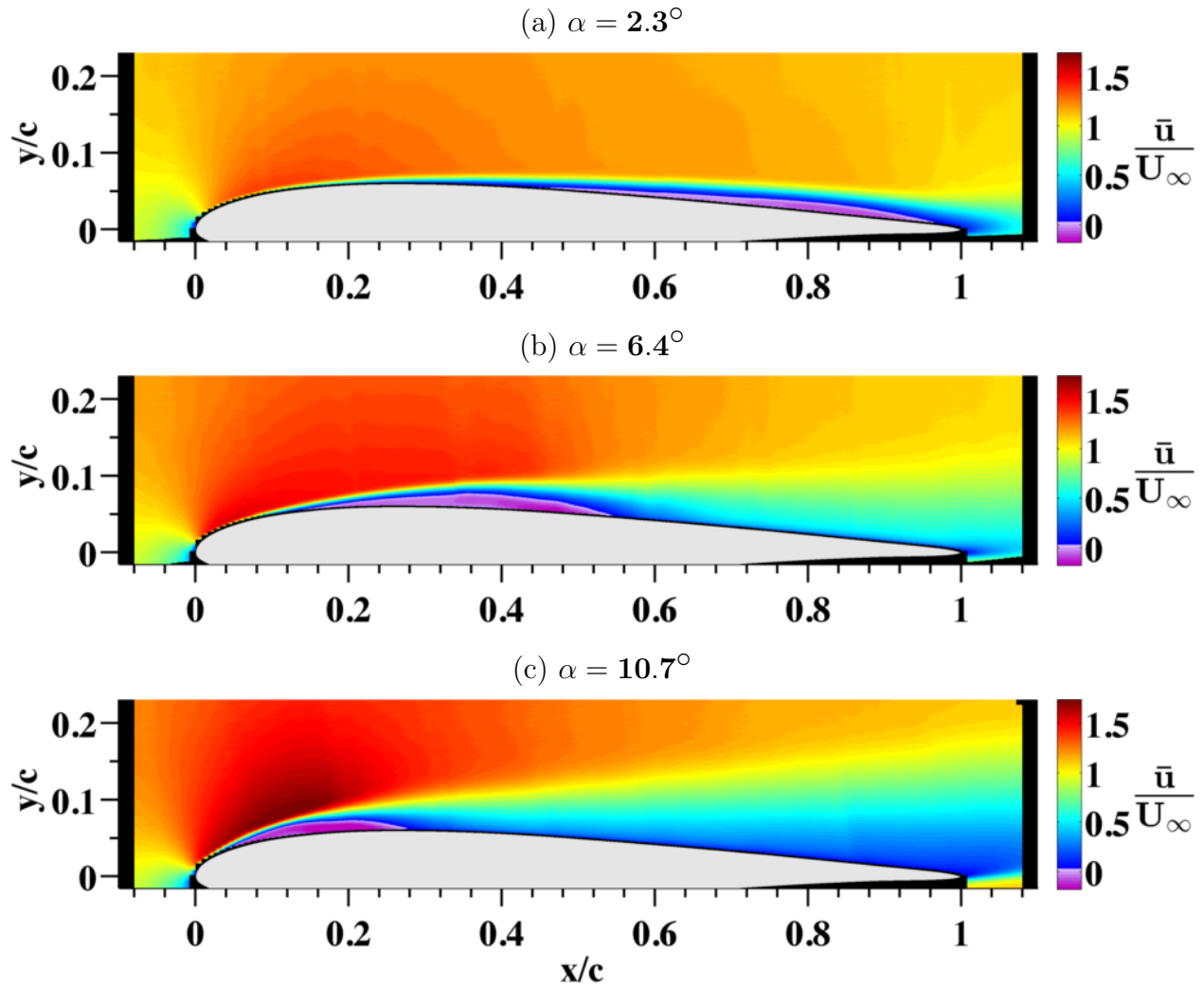


Figure 3.11: The mean flow field is shown for $Re_c = 3 \times 10^4$ with increasing α top to bottom. The location of the reversed flow region moves upstream as the angle is increased. The baseline cases are shown here, all other cases may be found in Appendix B.1

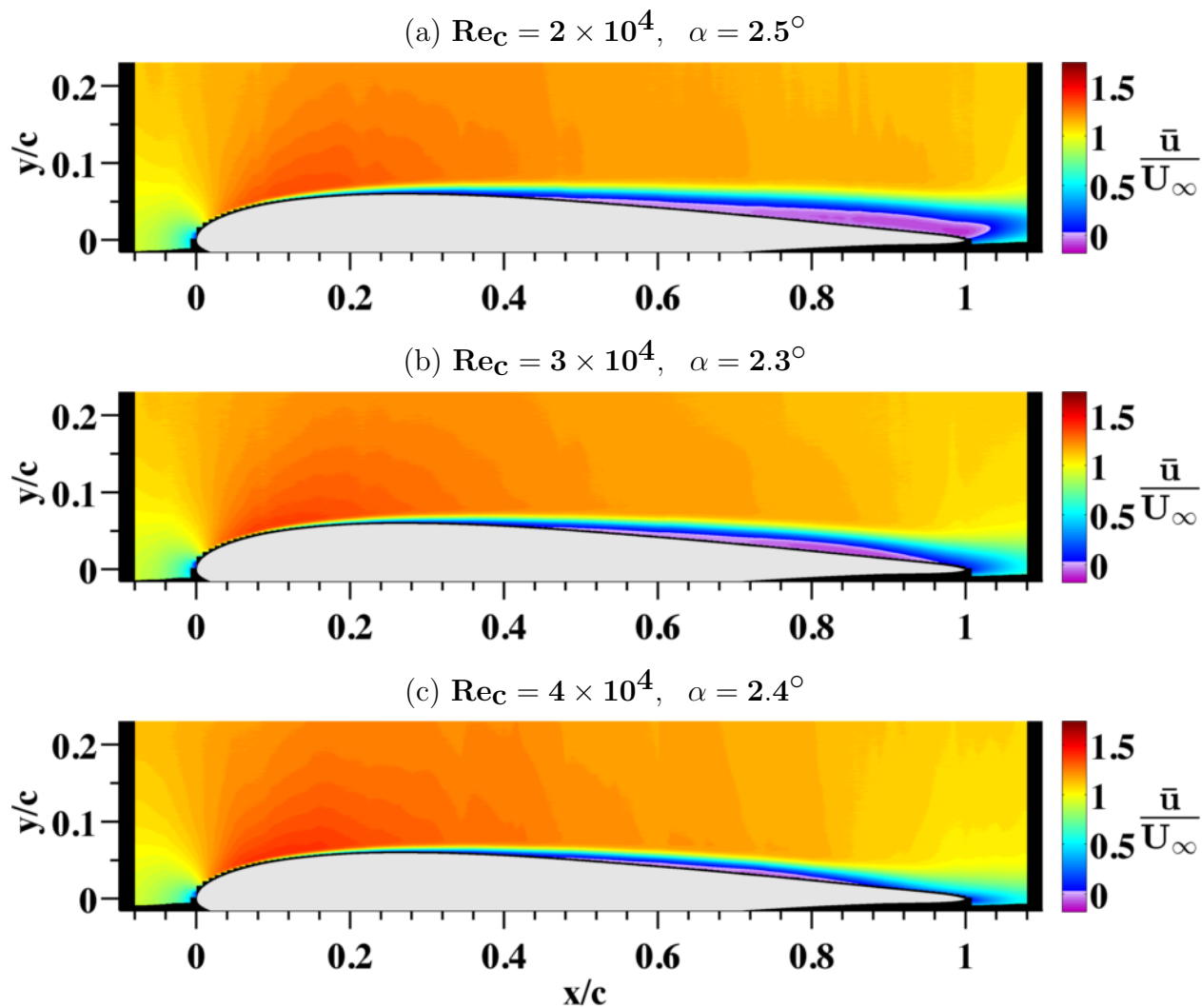


Figure 3.12: The mean flow field is shown for an increasing Re_c top to bottom for an $\alpha \approx 2.4^\circ$. The baseline cases are shown here, all other cases may be found in Appendix B.3. The primary effect of the Reynolds number is a thinning of the reversed flow region i.e. the LSB is shorter in height as Re_c increases. Also with increased Re_c the separation is delayed slightly and reattachment occurs farther upstream.

3.4 Comparisons of LSB Characteristics

The locations of separation, reattachment, and the bubble length between the baseline and added freestream turbulence configurations are compared in this section. The available data in the literature, namely Burgmann and Schröder (2008); Burgmann et al. (2007); Galbraith (2009), and the previous study at MSU, Katz (2010), are also presented for comparison.

3.4.1 Separation and Reattachment

The separation and reattachment locations for each Reynolds number studied are presented along with a discussion of the results. Each Reynolds number will be first discussed separately, with the results shown in Figures 3.13 for $Re_c = 2 \times 10^4$, 3.14 for $Re_c = 3 \times 10^4$, and 3.15 for $Re_c = 4 \times 10^4$. The primary features that are discussed and compared between different investigations in the following are: the general trends of separation and reattachment, the separation and the reattachment locations.

3.4.1.1 Reynolds Number 20,000

In Figure 3.13 the separation and reattachment locations are plotted versus angle of attack for both the baseline and added freestream turbulence configuration. The separation locations move downstream, relative to the baseline case, for the increased FSTI cases. The exception is at $\alpha = 10^\circ$; where, at this angle, the baseline flow has stalled, whereas the increased FSTI case has a closed separation bubble. The drastically different flow conditions may explain why the separation location does not fit the trend (of delayed separation due to increased FSTI) for this case. The strong adverse pressure gradient at this high angle of attack would dominate, making the boundary layer less receptive to freestream disturbances.

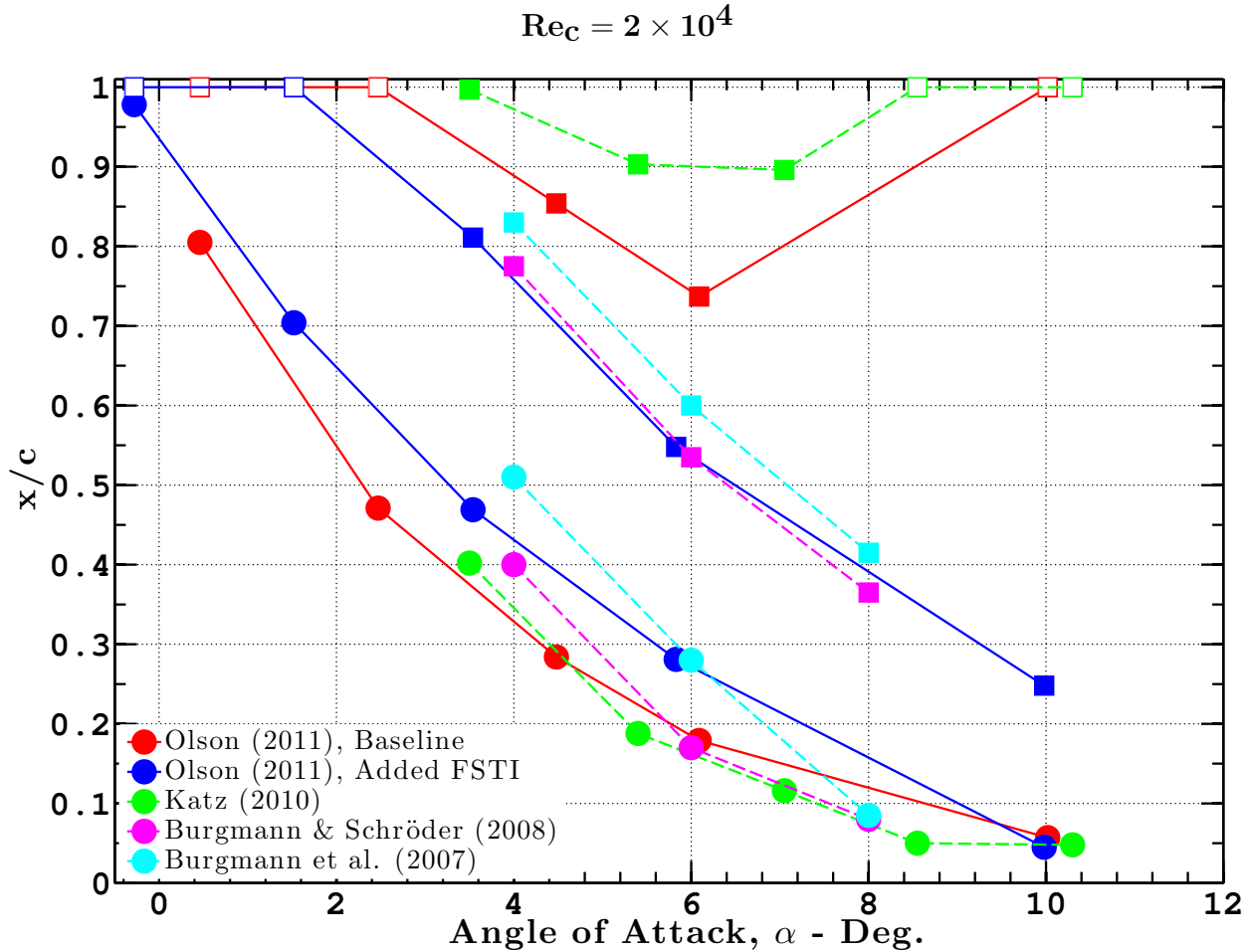


Figure 3.13: Separation (circles) and Reattachment (squares) locations are compared for $Re_c = 2 \times 10^4$. The square symbols with a white face color indicate an open separation. The error bars for the current experiments have been excluded from this and subsequent figures because the random uncertainty is typically less than the symbol size, however, this does not include the systematic error which is discussed later regarding the identification of separation and reattachment location.

The reattachment locations also change with increased FSTI, moving upstream relative to the baseline case. This is constant with the idea of the freestream disturbances exciting the Kelvin-Helmholtz instability, transporting higher momentum fluid towards the surface. At the lowest angles, where open separations occur, flow with increased FSTI has the effect of shortening the reversed flow region extending past the trailing edge (which may be seen in the contours at this Reynolds number of Figure B.1 located in Appendix B.1).

There is good qualitative agreement between the current study and previous MSU study, with open separation occurring in the baseline case at both low and high angles of attack. The disagreements in separation location appear to fall within the uncertainty of the measurements (the α uncertainty in the previous experiments was $\pm 0.4^\circ$).

The actual locations of reattachment are slightly different between the two studies at MSU, but, the overall effect appears to be consistent with the previous study having a lower FSTI than the current study. The freestream turbulence is however, not well known from the previous study and future work should attempt to quantify the FSTI of the previous MSU study utilizing the techniques described in Section 2.3 but applying them to the old data sets.

Comparing the reattachment locations of current data sets with those of Burgmann and Schröder (2008); Burgmann et al. (2007) also supports the hypothesis that the primary differences may be explained by the Burgmann studies having higher FSTI. The reattachment locations of these two studies by the Burgmann also agree very well with the cases with increased FSTI of the current study. The earlier Burgmann study (2007), however, had a FSTI of 1.5% whereas, in the 2008 study it had been reduced to 1.0%, The separation locations did move upstream as expected by increased freestream turbulence, but the reattachment

points actually moved downstream with increased FSTI. It is not entirely clear why this is the case, but as it has been shown, accurate characterization of these flow features are highly sensitive to a variety of issues, which have not all been quantified in previous investigations.

3.4.1.2 Reynolds Number 30,000

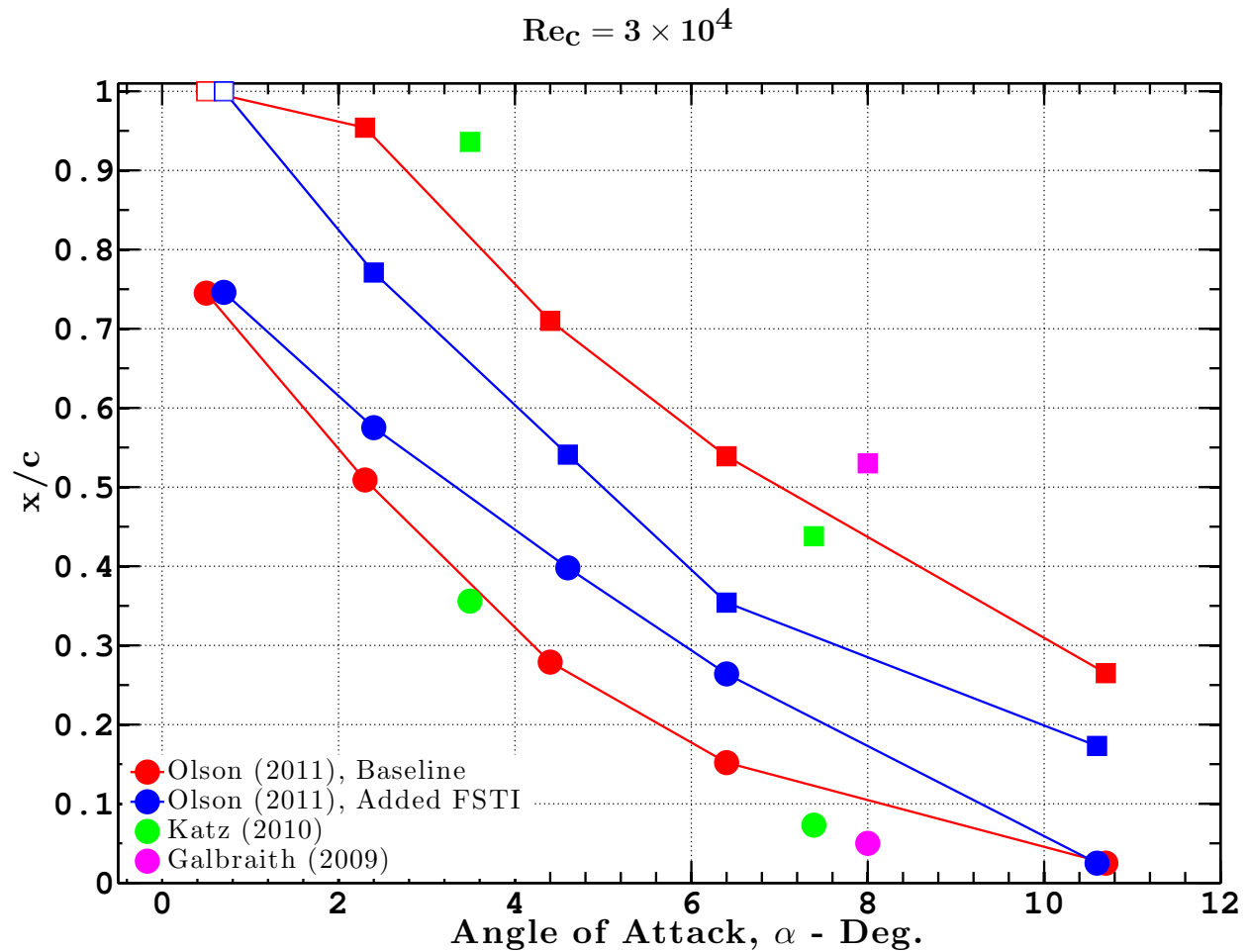


Figure 3.14: Separation (circles) and Reattachment (squares) locations are compared for $Re_c = 3 \times 10^4$. The square symbols with a white face color indicate an open separation.

At a Reynolds number of 3×10^4 , the effect of freestream turbulence and angle of attack are also observed (see Figure 3.14). Separation is delayed and an earlier reattachment is observed with increased FSTI. The influence of freestream turbulence on separation degrades at both high and low angles of attack (as observed at $Re_c = 2 \times 10^4$). The influence of FSTI on reattachment is similar at all angles, with , except in the case at $Re_c = 2 \times 10^4$ where stall was delayed.

There is good agreement between the previous MSU study and the current study. The same systematic difference in FSTI discussed at $Re_c = 2 \times 10^4$ can be applied to this data set as well. The other comparison at this Reynolds number, Galbraith (2009), is a simulation which has no freestream turbulence. With its location of separation farther upstream and reattachment farther downstream than the experimental data, the lack of FSTI in the simulations could potentially explain the differences observed.

3.4.1.3 Reynolds Number 40,000

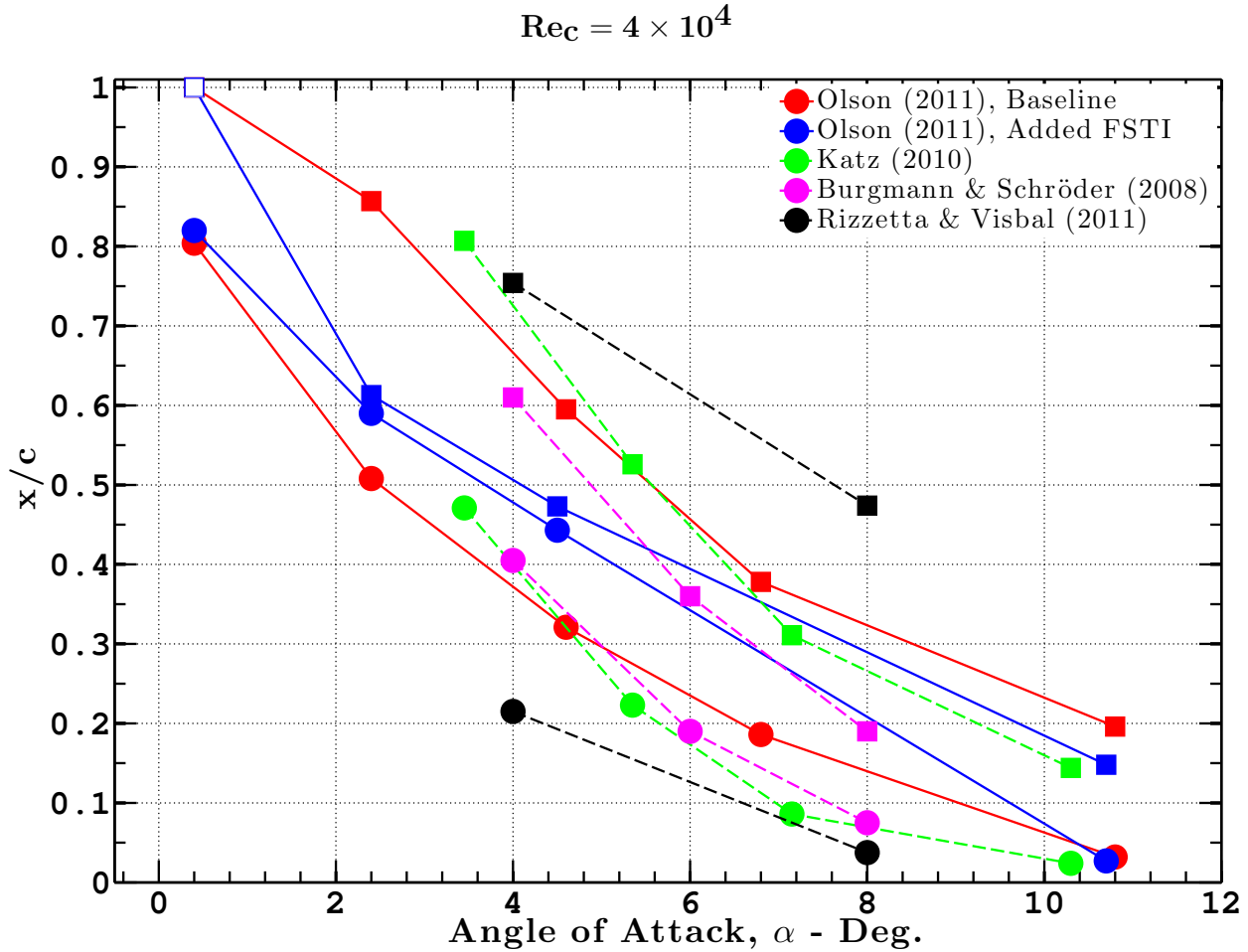


Figure 3.15: Separation (circles) and Reattachment (squares) locations are compared for $Re_c = 4 \times 10^4$. The square symbols with a white face color indicate an open separation.

The data shown in Figure 3.15 is the separation and reattachment locations for the current study and several other experimental (Katz, 2010; Burgmann and Schröder, 2008) and computational (Rizzetta and Visbal, 2011) studies. The same influence of increased FSTI, by delaying separation and an earlier reattachment relative to the baseline case, is observed. The shortening in height of the reversed flow region due to increased FSTI makes it difficult to discern if the bubble is either non-existent or too thin to detect at $\alpha \approx 7^\circ$. At

this Reynolds number, the decreasing influence of FSTI on separation location at both high and low angles of attack is observed.

There is more scatter when comparing the data at this Reynolds number among the different studies. There is relatively good agreement between the MSU studies in reattachment locations. However, there is a different slope in the separation curve between the MSU studies. The slope of the separation curve of the earlier MSU study (Katz, 2010) does, however, more closely match that of Burgmann and Schröder (2008).

With respect to the computations, there is poor agreement in separation location at $\alpha = 4^\circ$ although the agreement is much better at $\alpha = 8^\circ$. The better agreement at the high angle may be due to the larger pressure gradient at this angle of attack dominating the separation location. The bubble geometry is not as sensitive to the near-wall spatial resolution bias discussed below and also in Section 3.2.2. However, the opposite is true for reattachment, with the lower angle closer to the experiments than the higher angle. The systematic differences in numerical results of separation location may be explained in part by FSTI with both its effect on separation and reattachment locations and its effect on the bubble height.

The bias error in the detection of separation location due to bubble geometry, discussed in Olson et al. (2011) and also in Section 3.2.2, is estimated to be $0.05c$ for $Re_c = 4 \times 10^4$ and $\alpha = 4^\circ$ from the numerical results. Since this error estimate relies on the bubble geometry, which has been shown to change significantly for different Reynolds numbers and angles of attack, is also expected to change for each case. Less bias error is expected at $\alpha = 8^\circ$ due to the differences in bubble geometry, which may explain, in part, why separation agrees decently in the simulations to the experiments at this angle.

3.4.2 Bubble Length

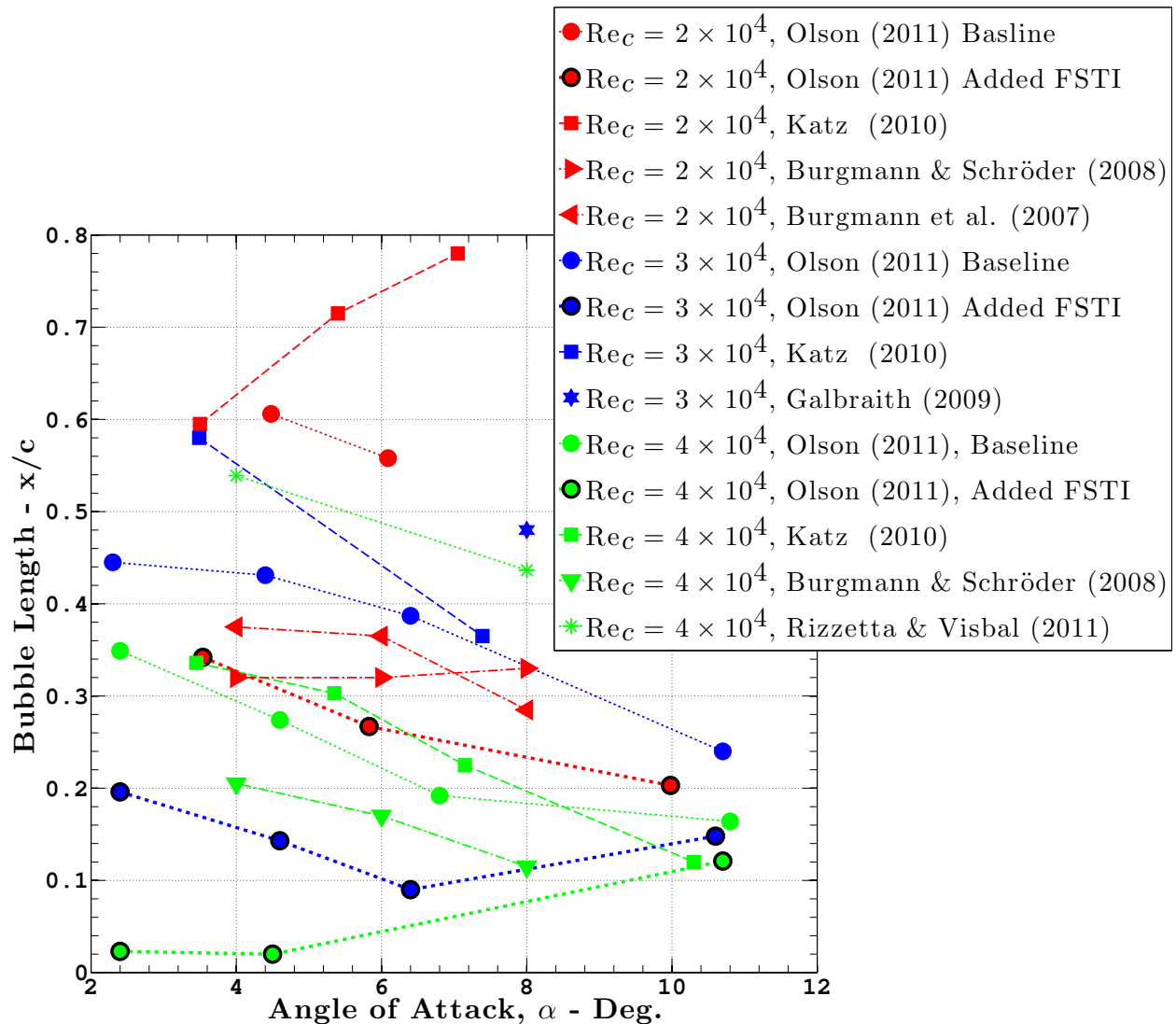


Figure 3.16: The compiled separation bubble length for different conditions and different studies. Each color represents a Reynolds number, and each symbol a particular study. The symbols with a black edge represent the increased FSTI cases with its face color indicating the Reynolds number.

The effect of increased FSTI has been shown to decrease the size of the laminar separation bubble in both length and height. Figure 3.16 show the length of the LSB for various Reynolds numbers versus angle of attack for all the studies discussed in this chapter.

The first observation from the figure is the amount of scatter in the data. There are

however, a few trends that can still be discerned. The effect of freestream turbulence is significant relative to the other influences of Reynolds number and angle of attack. In the Burgmann studies, contrary to all of the other studies, there is little dependency of the bubble length on angle of attack. In the case of all of the computational studies, the bubble length is considerably longer than experiments, which is expected from when the inherent experimental bias in determining the length of the LSB is considered and the influence of freestream turbulence.

For $2^\circ < \alpha < 7^\circ$ the length of the LSB has been shown to be reduced by $60 \pm 11\%$ between the baseline and increased FSTI configurations of the current experiments at $Re_c = 2 \times 10^4$ and $Re_c = 3 \times 10^4$. At $Re_c = 4 \times 10^4$, the length of the LSB is reduced by $\sim 95\%$ for the same range of angles. At the highest angle of attack in the current measurements, $\alpha \approx 10^\circ$, the length of the LSB was reduced by $\sim 18 \pm 4\%$.

3.4.3 Summary of LSB Characteristics

The separation location, reattachment location, and corresponding laminar separation bubble length have been measured for a range of α and Re_c for both the baseline and increased FSTI configurations. These characteristics have been presented in the preceding sections and have been tabulated in in Table C.1, in Appendix C.

3.5 Facility and Flow Dependent Issues

There are many factors that offer explanations for the differences in the measured separation and reattachment locations among the current study and the literature. Several of these effects have been described in the previous sections, such as, freestream turbulence, near-wall resolution, and the geometry of the reversed flow region. Some of these factors cause differences in the actual flow while others are inherent limitations of the experimental technique. The following sections are presented as potential explanations for differences in the literature.

3.5.1 Freestream Turbulence

The turbulence characteristics of the freestream have been shown to alter the flow around a stationary airfoil at $2 \times 10^4 < Re_c < 4 \times 10^4$. This is expected as freestream turbulence acts as excitation source to the boundary layer upstream of separation and also the separated shear layer downstream of separation. It is not clear which aspect(s) of the freestream turbulence influences the laminar separation bubble, whether it be the FSTI, integral length scale, or spectral content, but it is a significant contributing factor to differences in the measured LSB characteristics from different flow facilities. The lack of freestream turbulence in simulations is clearly problematic for comparisons to the flow obtained from experiments. The tendency of simulations to separate earlier and reattach later are consistent with the effect of freestream turbulence and can account for at least some of the discrepancies between simulations and experiments.

3.5.2 Flow Three-Dimensionality

The current experiments and those compared to in the literature all attempt to recreate nominal 2D flow conditions through the use of end walls, however, Burgmann and Schröder (2008) observed a significant amount of 3-dimensional flow over this airfoil. The differences in 3-dimensional flow structures for different levels of FSTI were studied in Burgmann and Schröder (2008) and was concluded to be small. The influence of finite aspect ratio, and blockage effects will both contribute to changes in the 3-dimensional structure of the flow, which were not the same between all the studies. It is not known what influences these effects will have on the separation and reattachment locations that are compared in the current study.

3.5.3 Airfoil Shape

This is a relatively obvious source of error when comparing studies conducted at different facilities and in computations. The actual shape of the current airfoil, described in Section 2.1.2, is approximately 1% thicker than the theoretical profile, with most of the added thickness occurring below the chordline. The decrease in camber compared to the theoretical profile would indicate, from thin airfoil theory estimates of the influence of camber (see Currie, 1993), a slight decrease in the effective angle of attack of $\sim 0.11^\circ$ is expected. This change in effective angle of attack due to the differences in camber is small and therefore, is not expected to effect the results, trends, and conclusions presented. Other studies in the literature do not report the actual shape of their model, which makes it impossible to compare actual profile shapes. The impact the slight deviations in airfoil shape is unknown, but, is easily investigated with inexpensive potential flow simulations.

3.5.4 Near-wall Spatial Resolution

In the current experiments, a region of 4-5 pixels is excluded near the wall due to surface imaging issues. It was seen from the current experiments (and computations found in the literature) that the LSB is very thin near separation, as shown in Figure 3.17. Identifying

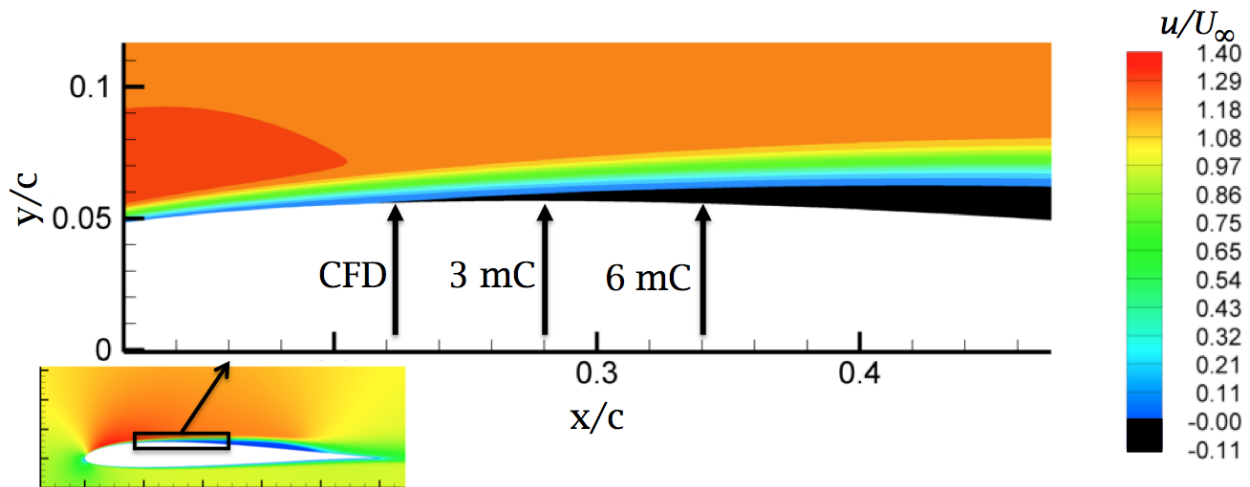


Figure 3.17: The region around separation from simulations (performed by Rizzeta & Visbal (2011)) at $Re_c = 4 \times 10^4$ and $\alpha = 4^\circ$ Olson et al. (2011). The arrows indicate where separation would be detected with the nearest velocity vector at ~ 0 (CFD), 3 mC, or 6 mC above the wall.

separation and reattachment from velocity data at some distance above the surface will introduce a bias in determining these locations. Separation will be identified farther downstream, estimated to be $0.05c$ at $Re_c = 4 \times 10^4$ and $\alpha = 4^\circ$, than compared to where the wall-shear stress is zero. The reattachment will be identified farther upstream than their real locations, by slightly less than the separation error, and is also highly dependent on the separation bubble geometry. The combined effect of these biases is such that the LSB will be measured to be shorter than it really is.

3.5.5 Uncertainty in Wall location

The experimental uncertainty in identifying the wall location in the current experiments is ± 2 pixels, which also contributes to the same type of error described in the previous section. Since the surface locations are used to determine the geometric angle of attack, one would be inclined to believe that this would also produce error in determining the angle of attack, but it does not. There is no increased error in determining α because if the error is purely random, it will not influence the mean surface result.

If there is a fixed bias, i.e. the surface is consistently selected above or below its physical location, the second degree of freedom in the optimization routine, used to determine the geometric angle, will account for this bias. The first degree of freedom is the airfoil angle of attack, while the second is the vertical location of the axis of rotation while its horizontal location is fixed due to the high degree of certainty of the streamwise location of the trailing edge. The only error that would contribute to an incorrect angle of attack would be one that systematically varied the surface identification location from the trailing to leading edge (or visa-versa). This was determined to not be the case by locating the same surface locations on different days and comparing the results.

3.5.6 Angle of Attack Sensitivity

The sensitivity of the separation location to the angle of attack can be seen from the current study and in the literature. The sensitivity at low angles of attack, $\alpha < 4^\circ$, was determined to be $\frac{\partial x_{\text{sep}}}{\partial \alpha} \approx 0.1c\text{deg}^{-1}$ (where x_{sep} is the location of separation) from both simulations and experiments in Olson et al. (2011) and the current experiments at $\text{Re}_c = 4 \times 10^4$. Clearly, with separation location moving $\sim 10\%$ of the chord per degree at low α , a considerable

amount of confidence in the angle of attack is required. Measuring the angle of attack is however, a nontrivial task experimentally: both the geometric orientation of the airfoil must be known as well as the angle of the freestream, which is non-zero due to the boundary layer growth along the test section walls.

The angle of attack listed for all the current experiments is relative to the bottom of the tunnel, which does not take into account the angle of the freestream. The freestream angle is expected to be small and its exclusion in the current experiments does not impact the trends and observations presented; for reference Katz (2010) measured (at ~ 4 c upstream of the airfoil) 0.25° at $Re_c = 2 \times 10^4$ and 0.14° at $Re_c = 4 \times 10^4$. The flow management between the current and this previous study was not the same and therefore, the freestream angles may not be the same. In the other literature, no detailed information is provided to clarify or quantify the freestream angle when computing the angle of attack.

Chapter 4

Summary

4.1 Summary

The influence of added Freestream Turbulence Intensity (FSTI) on the mean flow around a stationary SD7003 airfoil was studied experimentally for a range of chord Reynolds number ($Re_C = 2 \times 10^4 - 4 \times 10^4$) and angle of attack ($\alpha = 0^\circ - 11^\circ$).

The mean and RMS fluctuation of the streamwise velocity of the baseline flow were compared against the flow with added freestream turbulence using high resolution single-component Molecular Tagging Velocimetry with specific focus on the laminar separation bubble on the suction side of the airfoil. The locations of separation and reattachment, and the bubble length are quantitatively compared. Qualitative results regarding the height of the separation bubble and the differences in the streamwise velocity RMS fluctuations are discussed.

The influence of increased freestream turbulence was shown to move the separation location downstream and move the reattachment point upstream from where it occurs in the

baseline flow. The increased freestream turbulence has the effect of suppressing the separation bubble by both shortening it in length and in height. In some cases, the increase in freestream turbulence is associated with delaying stall, or even eliminating the reversed flow region in the mean flow (within the resolution of the measurements).

The influence of freestream turbulence, and other experimental parameters, such as near wall spatial resolution, and angle of attack sensitivity, have been explored to explain most of the discrepancies in separation and reattachment locations in the literature.

4.2 Future Work

There are many different aspects of the current work that can be expanded upon and others that can be immediately addressed from the current data sets.

The influence of increased FSTI should be quantified in terms of: laminar separation bubble height, the value and location of peak RMS of the fluctuating streamwise velocity. The observation of decreased streamwise fluctuation, (which should be correlated to the turbulent kinetic energy, although the current single component data prohibits making a comprehensive conclusion), should be quantified.

The near surface imaging issues, caused by the surface of the model absorbing the incident UV radiation and subsequently phosphorescing with a lifetime on the order of the MTV tracer needs to be addressed. This will enable future measurements of this type to have high quality data near the wall.

The extrapolation of the separation and reattachment location based on bubble geometry should be explored to yield better estimates of separation and reattachment. The technique should be first explored with computational data at various angles of attack and Reynolds

numbers (i.e. for different bubble geometries).

In regards to the influence of freestream turbulence on the laminar separation bubble, additional fundamental research is warranted in the receptivity of shear layer instabilities to freestream turbulence near a wall. It is also recommended that high fidelity simulations are performed that match the freestream conditions used in the present study such that the experiment may be compared directly to simulation results.

4.3 Conclusions

The discrepancies found in the literature regarding the locations of separation and reattachment can be mostly explained by the work presented. The basic flow around the stationary airfoil, in the range of Reynolds number investigated, are highly sensitive to both freestream conditions and the configuration parameters (such as Reynolds number and angle of attack). It has been shown that a high degree of precision and accuracy is required to properly characterize these flows. Luckily, much of the future work of MAV aerodynamics lies in fully unsteady motions, which tend to be less sensitive to these small details.

APPENDICES

Appendix A

Freestream Turbulence

A.1 Freestream Turbulence Spectra

The following Figures show the power spectral density for the freestream. Figure A.1 shows both the raw PSD and after the spatial mean has been removed for both the baseline and increased FSTI configurations. It is clear that the spatial mean, caused by the low frequency oscillations, make up a significant portion of the total fluctuation energy.

Referring to Figures A.1 (c) and (d), the shape of the PSD for each configuration are not significantly altered due to Reynolds number. It is the magnitude that changes with respect to Reynolds number. The Reynolds number effect on the magnitude of the PSD in the increased FSTI configuration is significantly less at low frequencies, and it is the high frequencies that tend to have the greater variation in magnitude. In the baseline case, the opposite is true of the Reynolds number effect, i.e. similar magnitudes at higher frequencies with the low frequencies varying in magnitude as a function of Reynolds number.

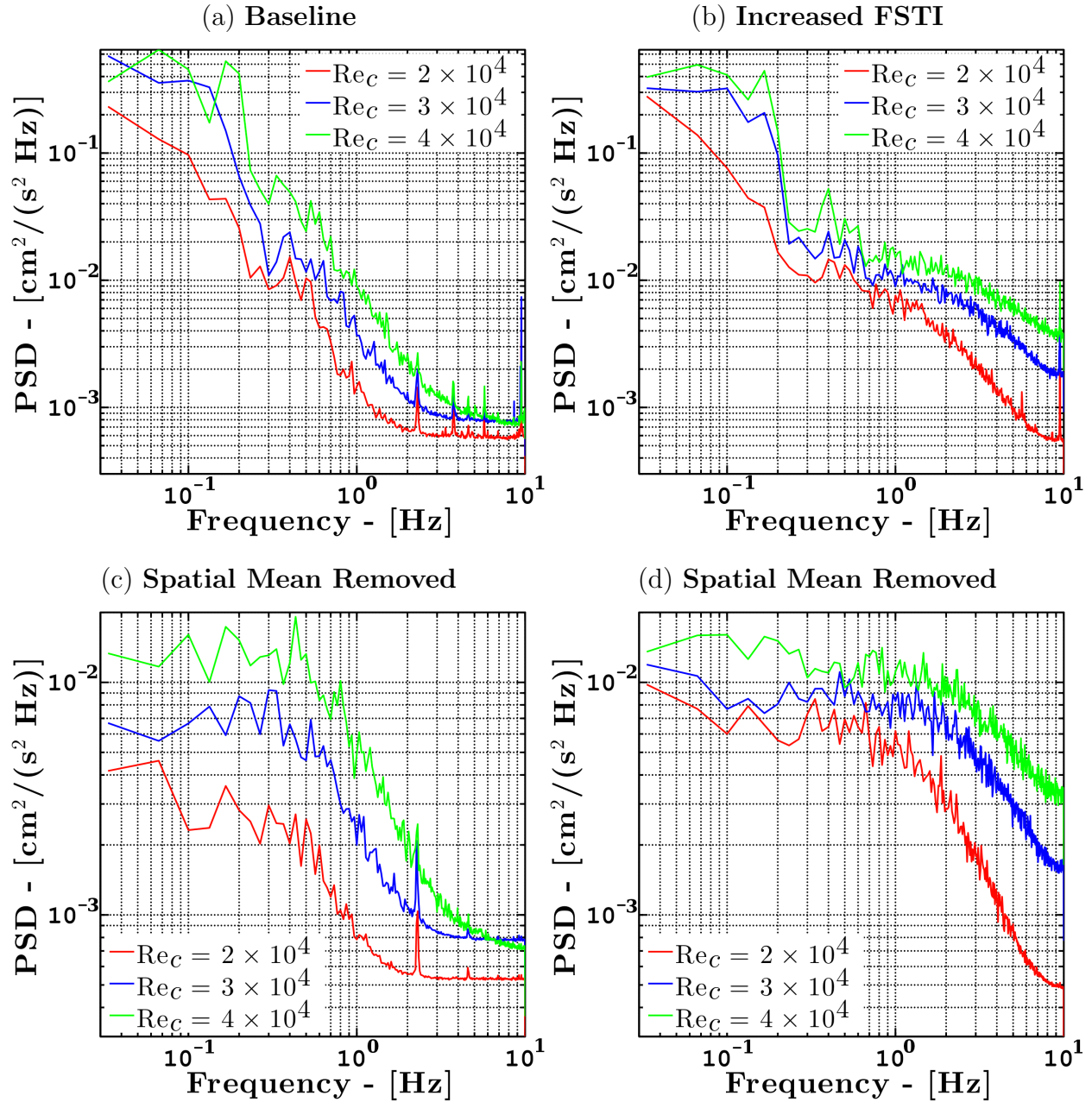


Figure A.1: The power spectral density for both the baseline and increased FSTI configurations are shown. In (a) and (b) the raw PSD are calculated and the low frequencies dominate the spectrum. By removing the oscillatory components due to spatially uniform fluctuations in velocity (the spatial mean velocity from each tag line is removed), the PSD shown in (c) and (d) are computed.

The influence of the grid at each Reynolds number may be seen in Figure A.2. At low Reynolds number, 2×10^4 , the increase in PSD is over a broad range of frequencies, while trailing off at high frequencies. At the higher Reynolds numbers of 3×10^4 and 4×10^4 , the influence of the grid is minimal for frequencies up to 0.3 Hz (3×10^4) and 0.9 Hz (4×10^4).

The differences in the spectra as a function of Reynolds number could be significant. At higher Reynolds number, it appears that it is primarily small scales of turbulence that are introduced, whereas as lower Reynolds number, it is larger scales are primarily introduced. However, since the overall trends observed in this study are consistent across different Reynolds numbers, it is likely that the effect observed can be related to the changes in FSTI and not requiring entire turbulence spectra to describe the changes in LSB characteristics between the baseline flow and the flow in the presence of the grid.

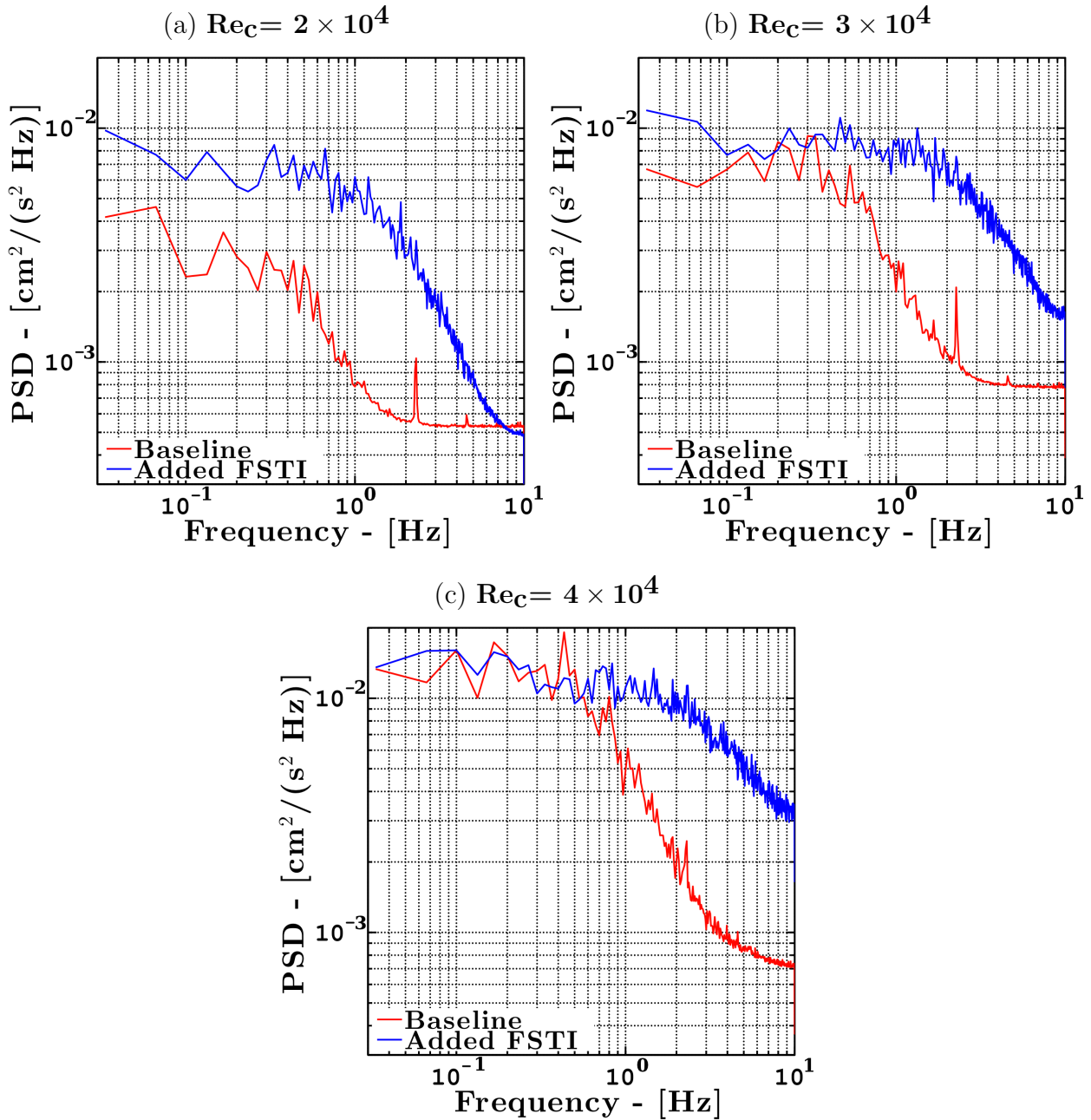


Figure A.2: The power spectral density for $Re_c = 2 \times 10^4$, 3×10^4 , and 4×10^4 are shown comparing the two configuration at each Reynolds number. The addition of the grid increases the broadband freestream turbulence across all Reynolds numbers however, its impact on low frequencies degrades as Reynolds number increases and its impact on high frequencies increases as the Reynolds number increases.

Appendix B

Mean and RMS Contours

B.1 Mean Flow field Evolution by Angle of Attack

The proceeding three pages compare the mean baseline flow to the flow with increased FSTI as a function of Reynolds number and angle of attack. Each page is dedicated to a single Reynolds number, with the baseline cases in the left column and the increased FSTI cases in the right column and an increasing angle of attack top to bottom. All of the colormaps are the same, $-0.18 \leq \frac{\bar{u}}{U_\infty} \leq 1.74$. The colormap has been created with a step change at 0 with an increasing intensity of ‘pink’ representing higher negative velocity. Velocities outside this range are saturated.

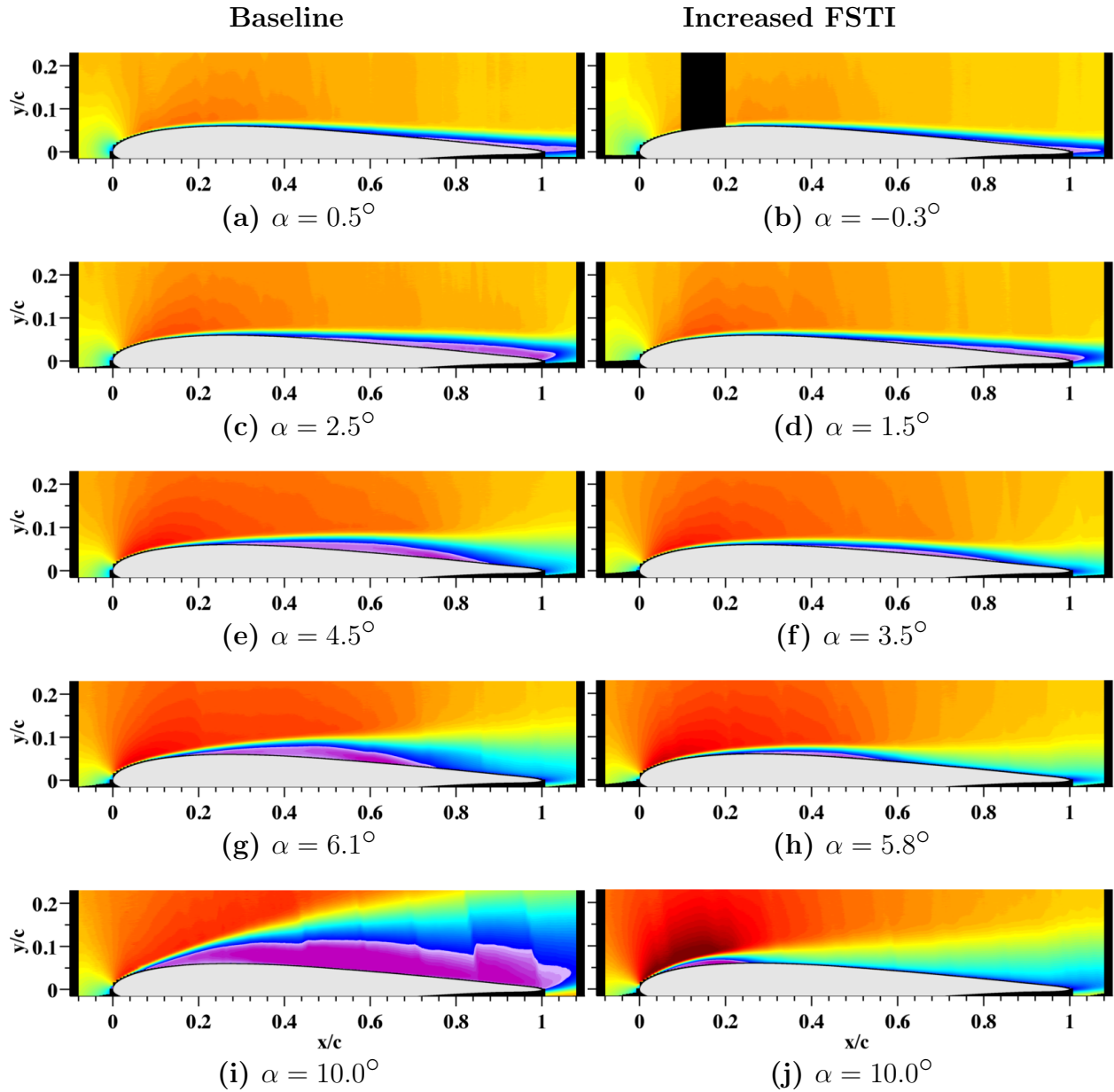


Figure B.1: The mean flow field is shown for $Re_c = 2 \times 10^4$ with increasing α top to bottom. Added freestream turbulence is on the right column.

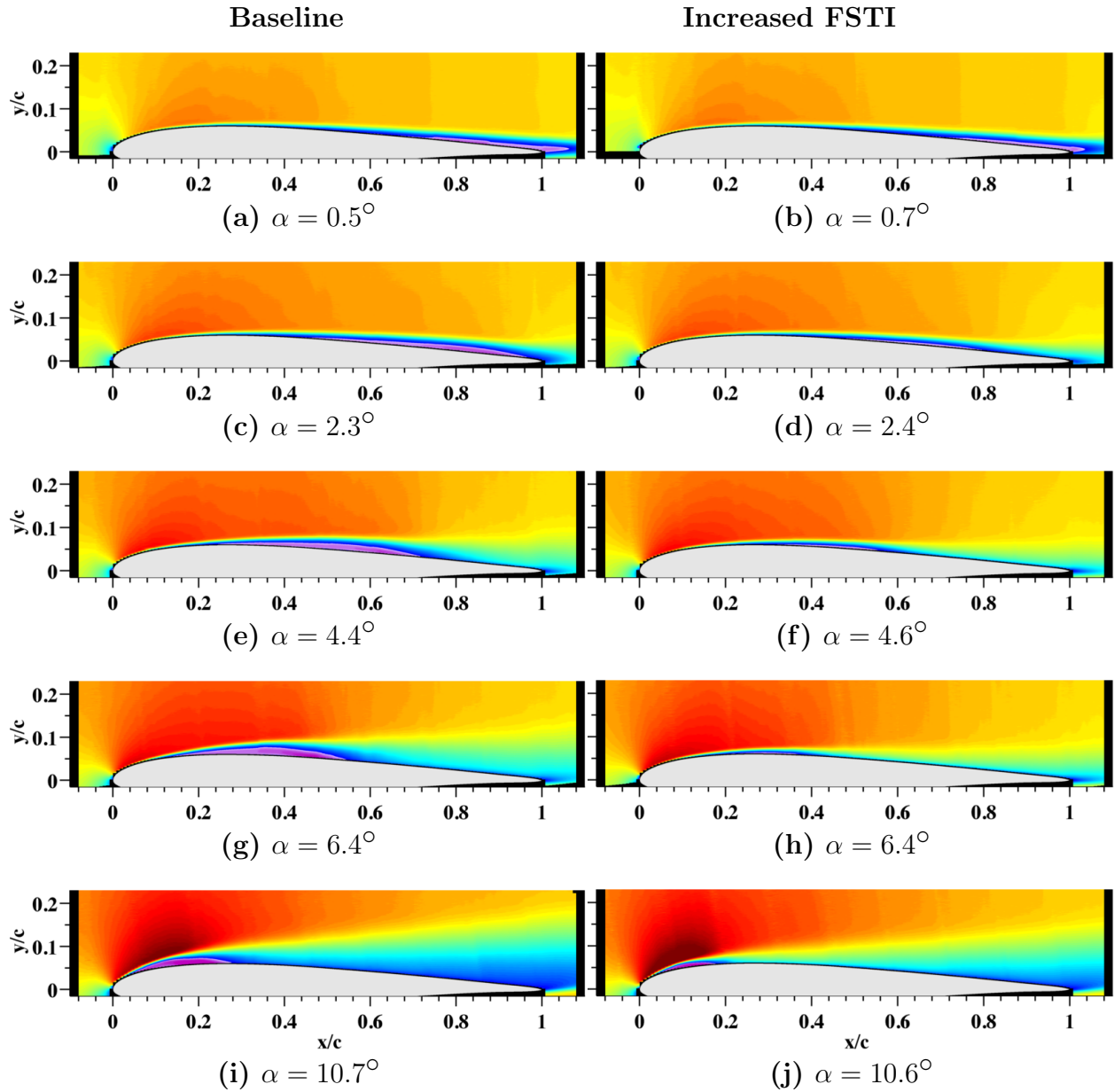


Figure B.2: The mean flow field is shown for $Re_c = 3 \times 10^4$ with increasing α top to bottom. Added freestream turbulence is on the right column.

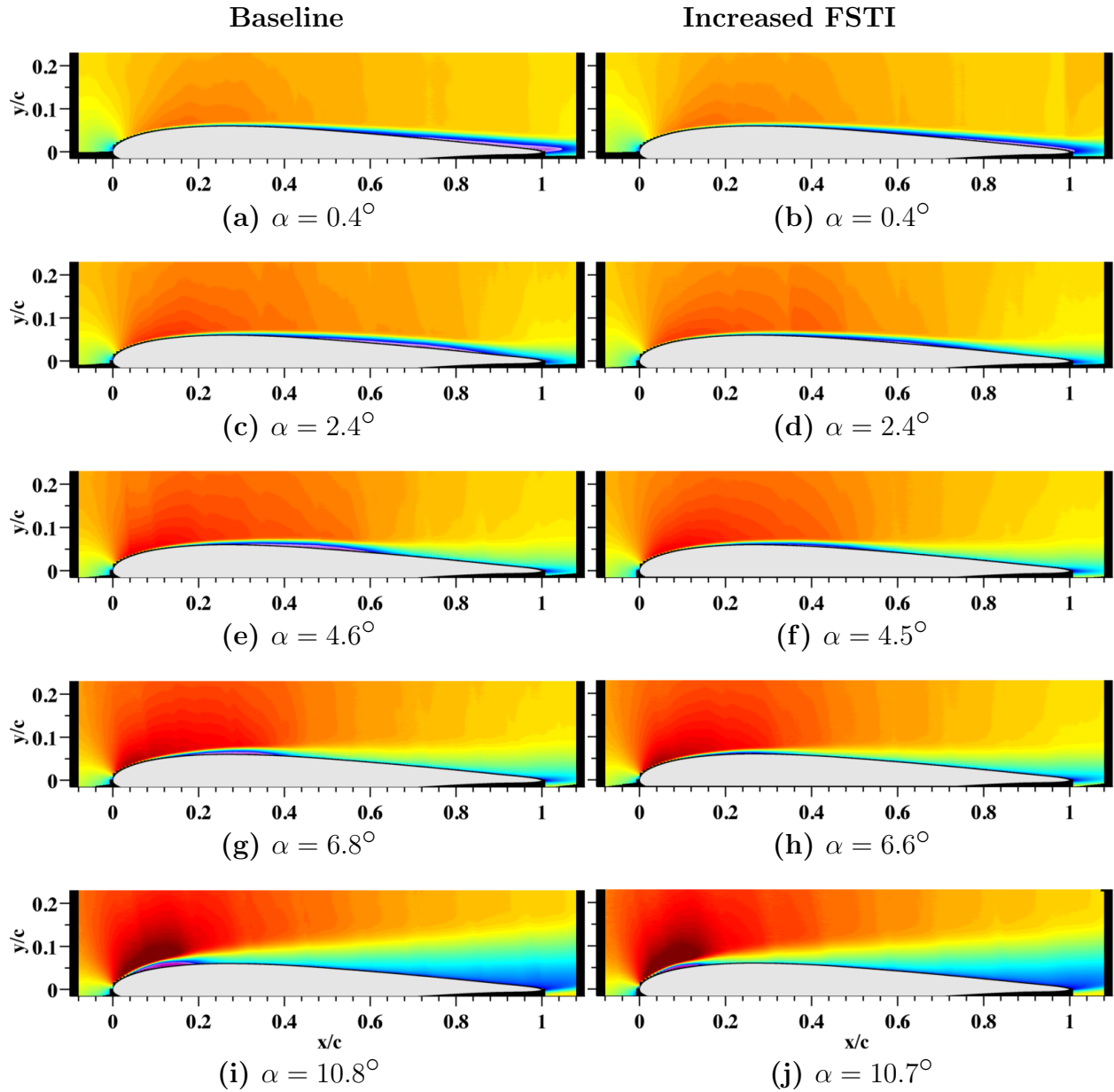


Figure B.3: The mean flow field is shown for $Re_c = 4 \times 10^4$ with increasing α top to bottom. Added freestream turbulence is on the right column.

B.2 RMS Flow field Evolution by Angle of Attack

The following three pages compare the streamwise RMS fluctuation of the baseline flow to the flow with increased FSTI as a function of Reynolds number and angle of attack. Each page is dedicated to a single Reynolds number, with the baseline cases in the left column and the increased FSTI cases in the right column and an increasing angle of attack top to bottom. There are two color scales; the first for $Re_c = 2 \times 10^4$ and 3×10^4 is $0.02 \leq \frac{u_{rms}}{U_\infty} \leq 0.40$ and the second, for $Re_c = 4 \times 10^4$, is $0.02 \leq \frac{u_{rms}}{U_\infty} \leq 0.30$. In almost all cases, the floor level of $\frac{u_{rms}}{U_\infty} < 0.02$ yields no appreciable flow information, and is made up mostly of non-uniform background noise. The exception is the $Re_c = 2 \times 10^4$ at the lowest α , where one can see a very slight increase in RMS above the trailing edge location. With a more appropriate color scale, one would see a slender band of increased RMS over the aft end of the airfoil, similar to the next higher angle.

The background RMS has been subtracted from each line to account for the spatial non-uniformities in the SNR of each tag line, which greatly influence the RMS as SNR drops. The background RMS that is subtracted is simply the mean u_{rms}^2 from the first 100 pixels in the tag line with no appreciable difference between the removed background between the baseline and increased FSTI cases were found.

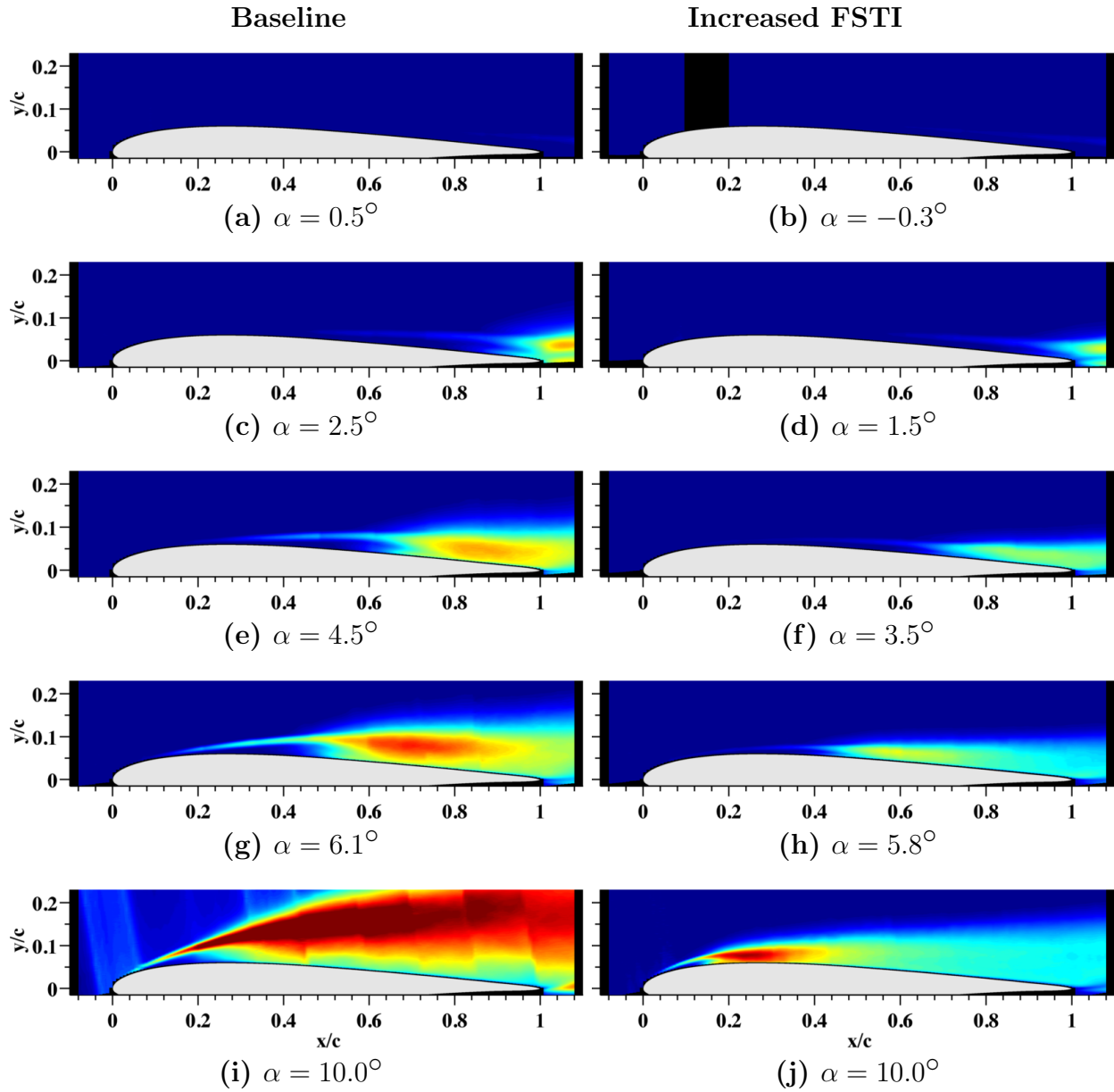


Figure B.4: The RMS flow field is shown for $Re_c = 2 \times 10^4$ with increasing α top to bottom. Added freestream turbulence is on the right column.

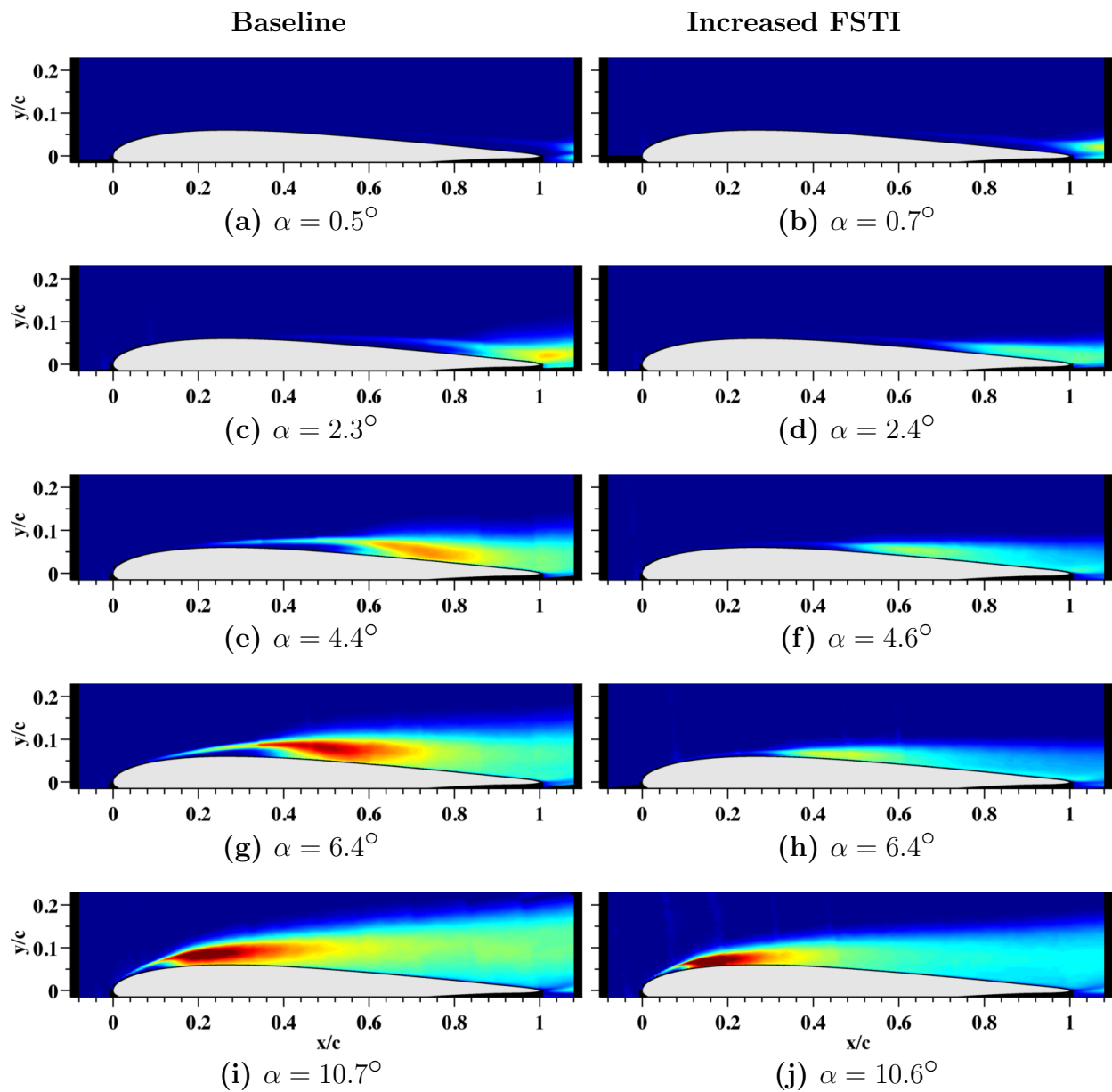


Figure B.5: The RMS flow field is shown for $Re_c = 3 \times 10^4$ with increasing α top to bottom. Added freestream turbulence is on the right column.

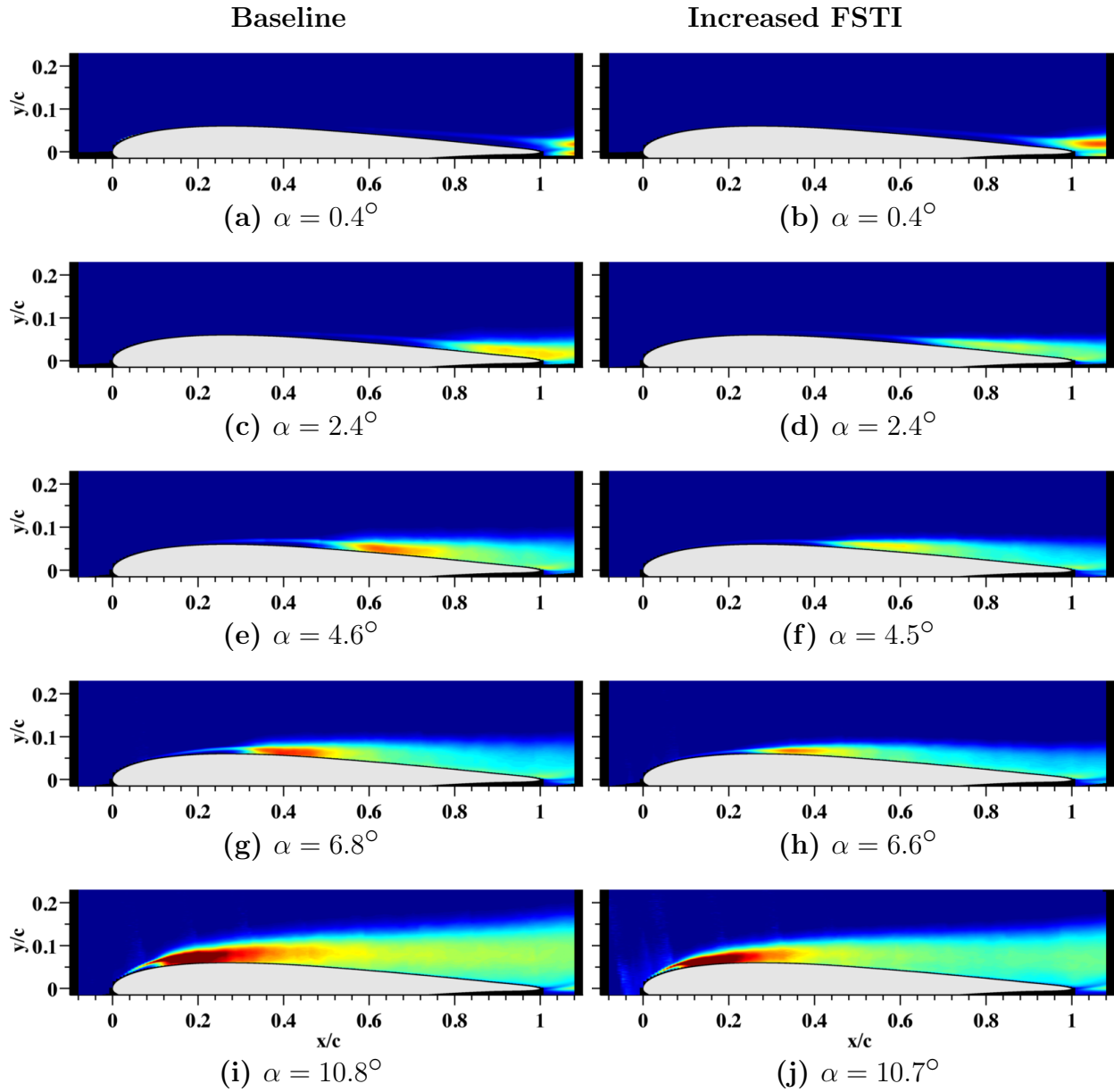


Figure B.6: The RMS flow field is shown for $Re_c = 4 \times 10^4$ with increasing α top to bottom. Added freestream turbulence is on the right column.

B.3 Mean Flow field Evolution by Reynolds Number

The proceeding section compares the mean flow as a function of Reynolds number at simliar angles of attack. Each page is dedicated to a single angle of attack, with an increasing Reynolds number top to bottom.

There is little effect of Reynolds number at very low angles of attack, $\alpha \approx 0.5^\circ$ as seen in Figure B.7. However, increasing the angle of attack to $\alpha \approx 2.5^\circ$, shown in Figure B.8, both the length and height of the reversed flow region can be seen to decrease with increasing Reynolds number. The location of separation appears to not be significantly effect at this angle of attack. At a much higher angle, $\alpha \approx 10.5^\circ$, which may be seen in Figure B.9, the effect of Reynolds number is even more drastic than at the lower angle, but the effects are the same: reversed flow region thins and shortens with increasing Reynolds number, with the reattachment location moving upstream considerably with Reynolds number.

The same trends are observed between both the baseline and increased FSTI configurations. The increased FSTI configuration for $\alpha \approx 10.5^\circ$ is shown in Figure B.10 to demonstrate the simliar Reynolds number effects between both levels of freestream turbulence.

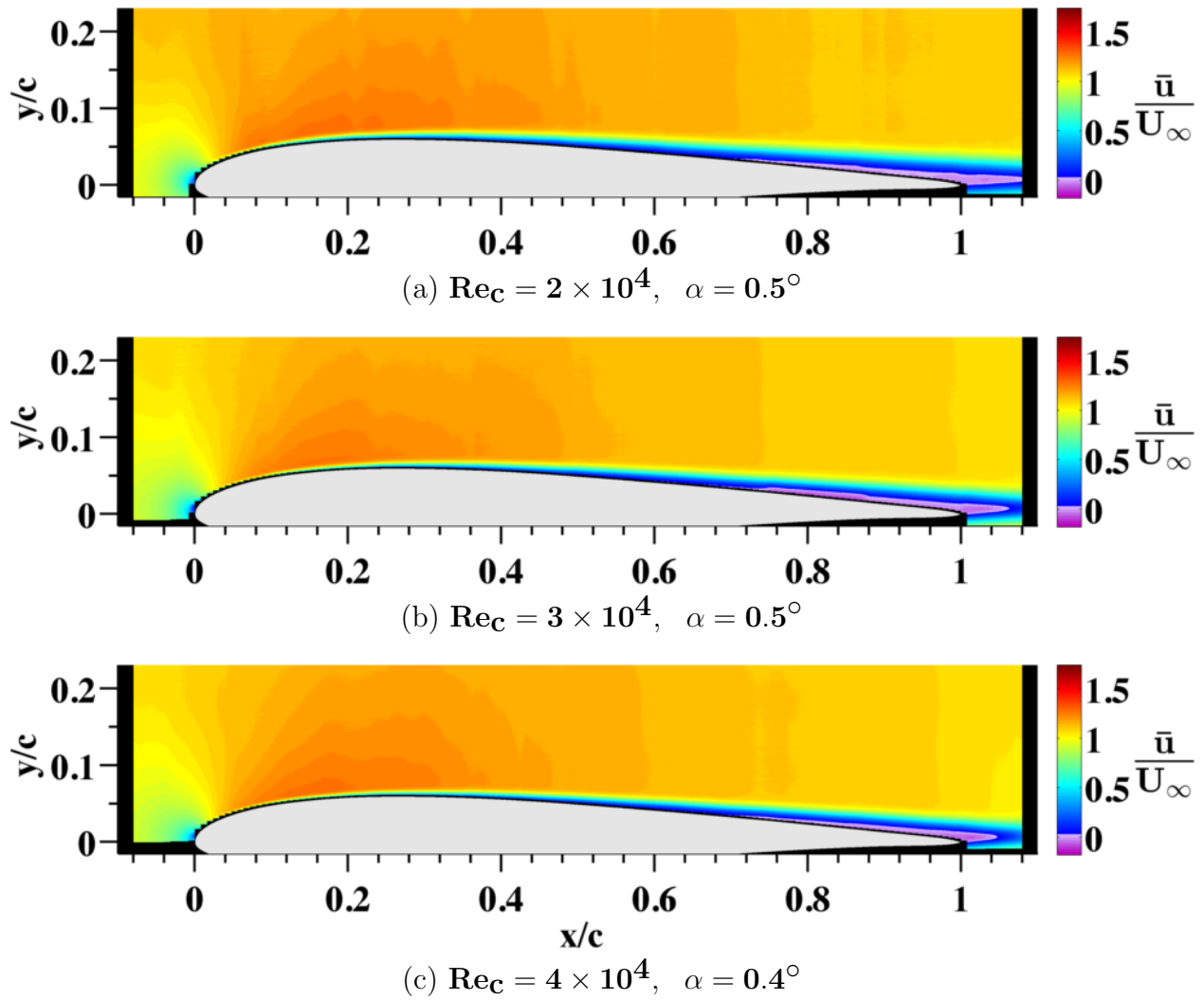


Figure B.7: The baseline configuration mean flow fields are shown for an increasing Re_c top to bottom for an $\alpha \approx 0.5^\circ$.

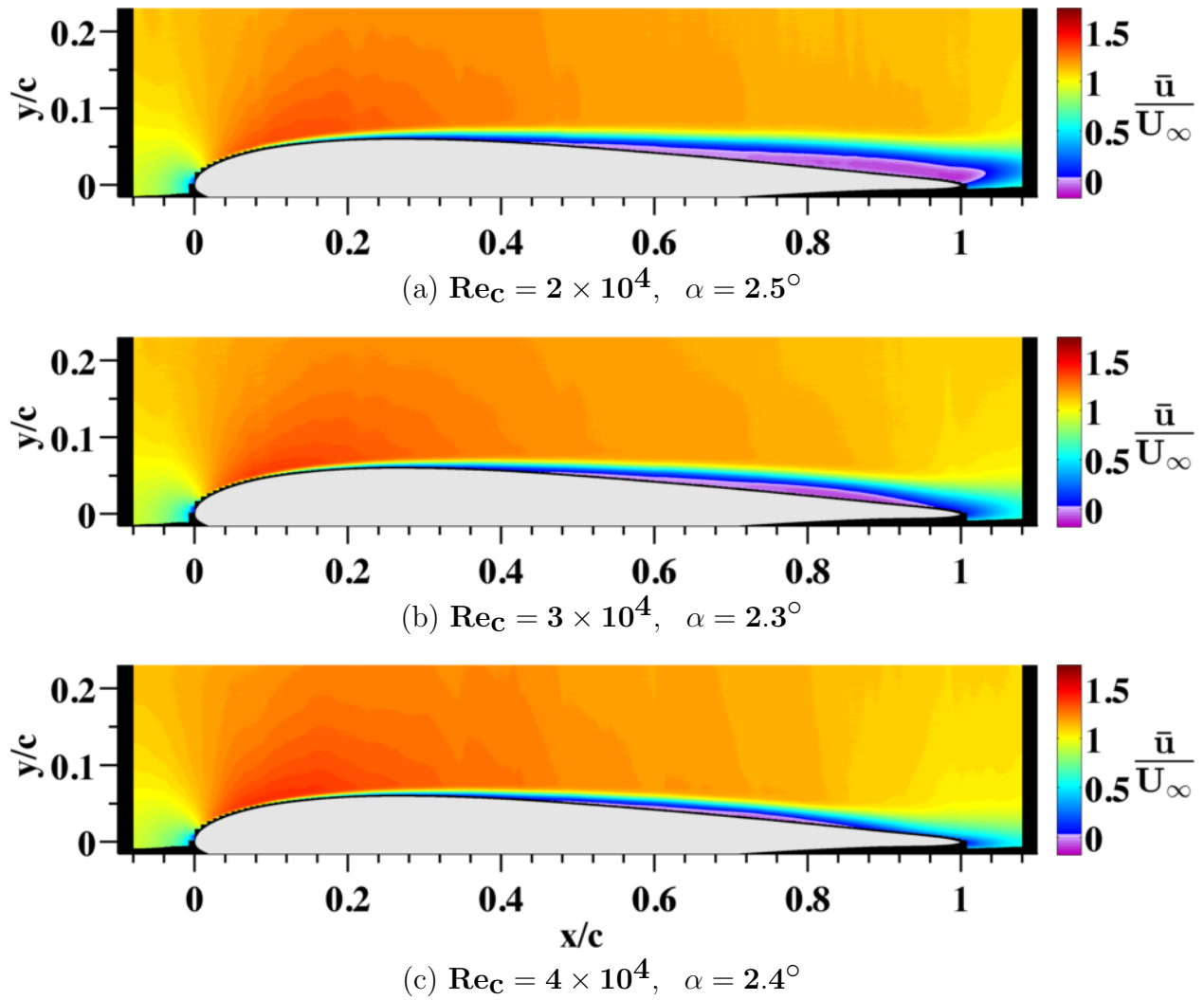


Figure B.8: The baseline configuration mean flow fields are shown for an increasing Re_c top to bottom for an $\alpha \approx 2.4^\circ$.

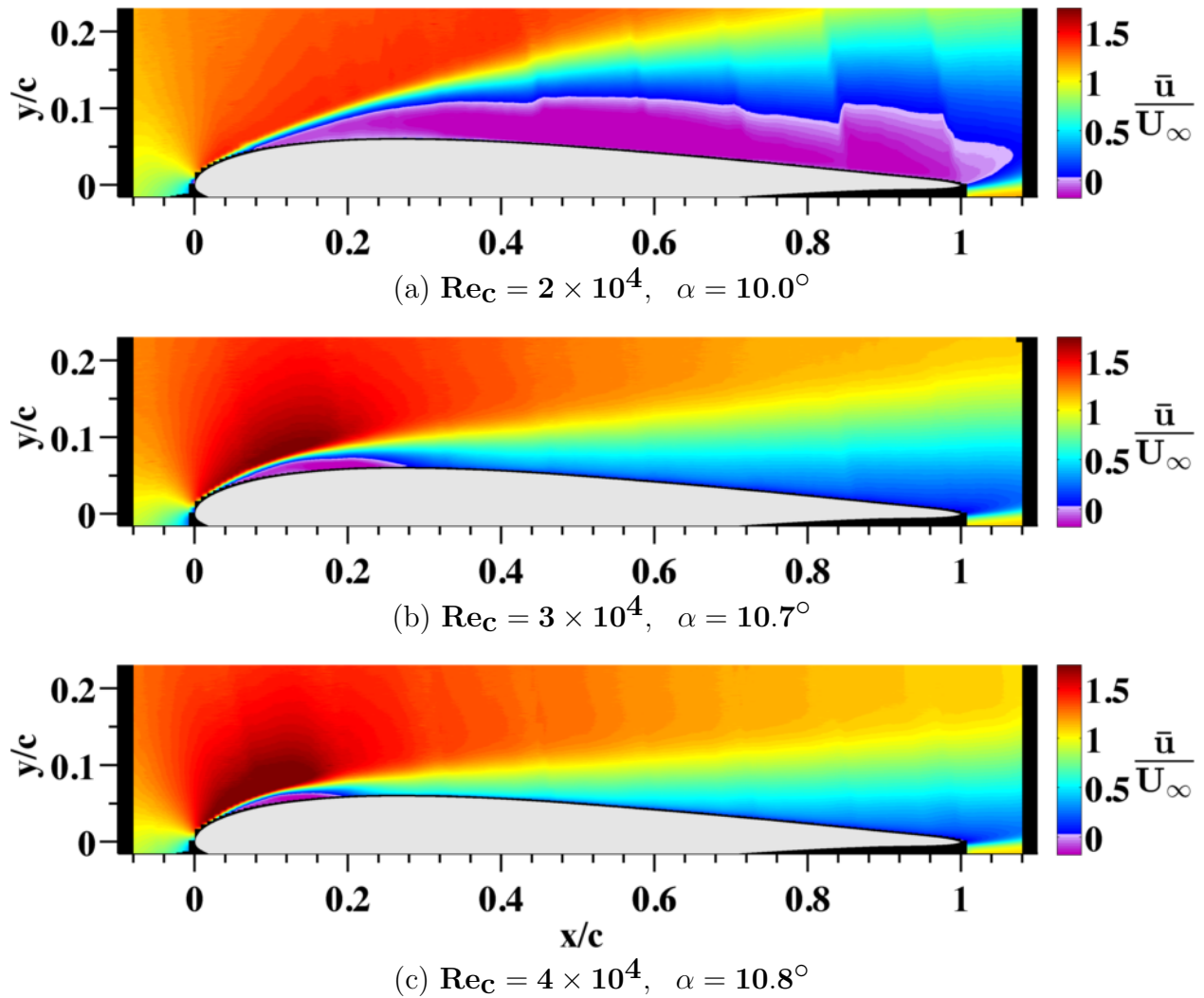


Figure B.9: The baseline configuration mean flow fields are shown for an increasing Re_c top to bottom for an $\alpha \approx 10.5^\circ$.

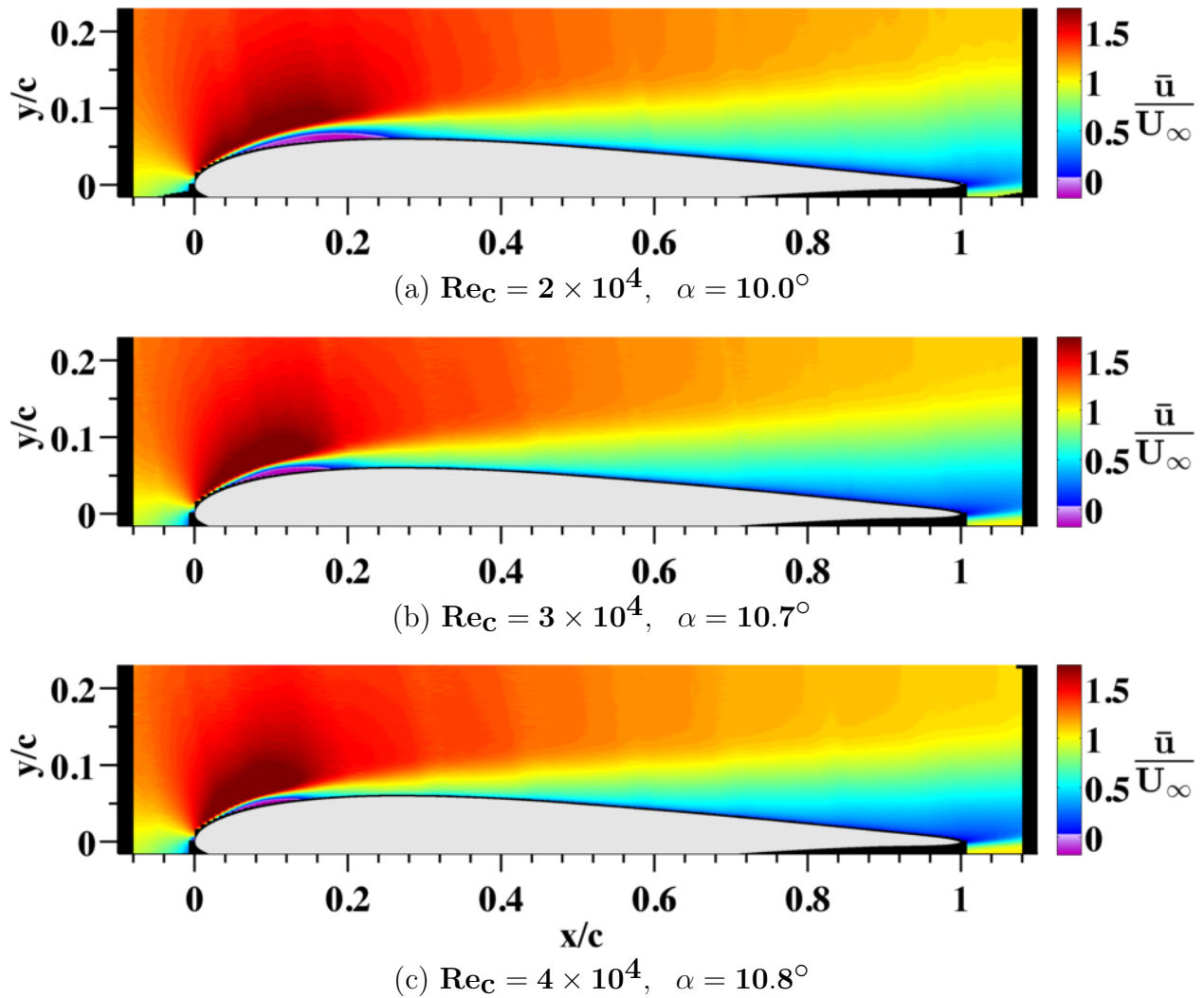


Figure B.10: The increased FSTI configuration mean flow fields are shown for an increasing Re_c top to bottom for an $\alpha \approx 10.4^\circ$.

Appendix C

Compiled LSB Characteristics

The following table lists the separation and reattachment locations and the LSB bubble length from the current experiments. The Reynolds number referenced is the nominal Reynolds number, the precise Re_c and the angle of attack uncertainty may be found in Table 2.1 on 33.

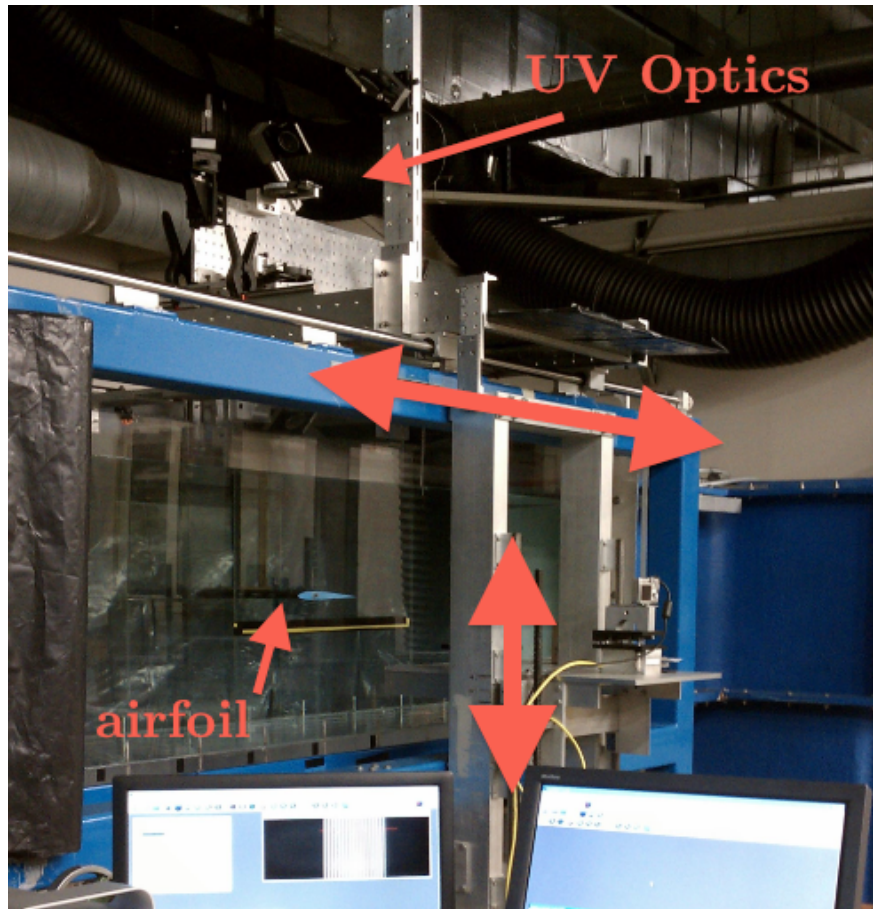
Table C.1: Separation location, reattachment location, and bubble length are tabulated for each case. All values are determined from a location ~ 2.69 mm (0.0013c) above the airfoil surface. If the flow does not reattach, the reattachment location is listed as ‘open’. If flow separation is not detected, the separation location is listed as N/A.

	α [deg]	Separation Location [x/c]	Reattachment Location [x/c]	Bubble Length [x/c]
Baseline $Re_C = 2 \times 10^4$	0.5	0.81 ± 0.01	open	N/A
	2.5	0.47 ± 0.02	open	N/A
	4.5	0.28 ± 0.01	0.86 ± 0.01	0.57 ± 0.01
	6.1	0.18 ± 0.02	0.74 ± 0.02	0.28 ± 0.02
	10.0	0.06 ± 0.01	open	N/A
Baseline $Re_C = 3 \times 10^4$	0.5	0.70 ± 0.05	open	N/A
	2.3	0.51 ± 0.01	0.95 ± 0.01	0.45 ± 0.01
	4.4	0.27 ± 0.01	0.71 ± 0.01	0.44 ± 0.01
	6.4	0.15 ± 0.02	0.55 ± 0.01	0.40 ± 0.02
	10.7	0.03 ± 0.01	0.27 ± 0.01	0.24 ± 0.01
Baseline $Re_C = 4 \times 10^4$	0.5	0.80 ± 0.01	open	N/A
	2.5	0.51 ± 0.01	0.86 ± 0.01	0.35 ± 0.01
	4.5	0.32 ± 0.01	0.60 ± 0.01	0.27 ± 0.01
	6.8	0.19 ± 0.01	0.38 ± 0.01	0.19 ± 0.01
	10.8	0.03 ± 0.02	0.20 ± 0.01	0.16 ± 0.01
Added FSTI $Re_C = 2 \times 10^4$	-0.3	0.98 ± 0.01	open	N/A
	1.5	0.70 ± 0.01	open	N/A
	3.5	0.47 ± 0.01	0.81 ± 0.01	0.34 ± 0.01
	5.8	0.28 ± 0.02	0.55 ± 0.02	0.27 ± 0.02
	10.0	0.05 ± 0.02	0.25 ± 0.01	0.20 ± 0.02
Added FSTI $Re_C = 3 \times 10^4$	0.7	0.76 ± 0.02	open	N/A
	2.4	0.57 ± 0.01	0.77 ± 0.02	0.20 ± 0.02
	4.6	0.40 ± 0.01	0.54 ± 0.01	0.14 ± 0.01
	6.4	0.26 ± 0.01	0.36 ± 0.02	0.09 ± 0.02
	10.6	0.03 ± 0.01	0.18 ± 0.01	0.15 ± 0.01
Added FSTI $Re_C = 4 \times 10^4$	0.4	0.82 ± 0.01	open	N/A
	2.4	0.59 ± 0.02	0.61 ± 0.02	0.02 ± 0.02
	4.5	0.44 ± 0.02	0.47 ± 0.02	0.03 ± 0.02
	6.6	N/A	N/A	N/A
	10.7	0.03 ± 0.02	0.15 ± 0.01	0.12 ± 0.01

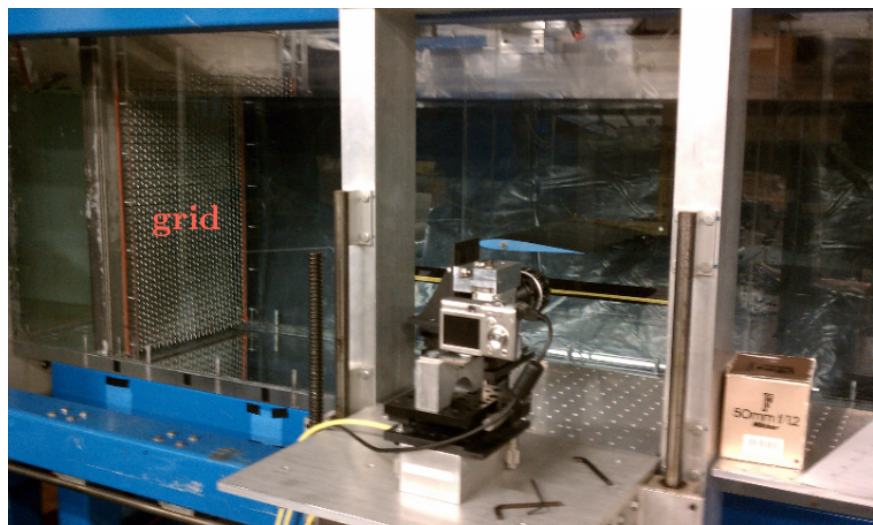
Appendix D

Miscellaneous

D.1 Test Section Photos



(a) View Looking Downstream



(b) View Looking Upstream

Figure D.1: Photos of the test section. The primary imaging system and the translating UV optics attached to the streamwise linear traverse.

D.2 Procedure of Simulated Experiments

The following procedure outlines the simulated experiments that were performed to validate using the 1c-MTV technique over the surface of an airfoil under the conditions of the experiments.

1. “Known Flow Field”

The mean velocity field from CFD simulations are utilized to provide the flow field in which the “experiments” will be performed. This flow field is assumed to be indicative of the flow fields to be examined during the actual experiments of this study.

2. Coordinate Transformations

The coordinate systems of CFD simulations place the chordline of the airfoil along the x-axis and the freestream u and v are adjusted to achieve the desired angle of attack. The experiments on the other hand, move the airfoil relative to a freestream that has (nearly) zero v . So, coordinate system of the CFD simulation is transformed into the experimental reference frame.

3. Tag Lines

The Lagrangian displacement of prescribed fluid locations, with a spatial resolution in the cross stream and line spacing indicative of the current experiments, are tracked in time.

4. Displacement

Each fluid element is displaced using the known flow field for a time period of Δt using 10 intermediate time steps between $t = 0$ and $t = \Delta t$.

5. Measurement

The displaced fluid elements are remapped (via linear interpolation) such that the y-positions of original fluid locations are found. This yields a displaced lines of fluid whose Y-locations are the same as the initially prescribed fluid. The displacement is found from subtracting the originally prescribed fluid location from the location of the fluid with the same y-value. This accurately simulates the processing technique used for 1c-MTV without considering a finite line thickness or signal to noise of images, i.e. it is the best possible estimate of velocity using this technique. The velocity is calculated by dividing by Δt .

6. Comparison

The known flow field (CFD) is remapped onto the simulated experiment's originally prescribed fluid data locations to allow the error in u to be calculated for each location.

D.3 Experimental Procedure

The following procedure outlines the experiments that were performed in this study.

1. Tunnel Speed Adjustment

At the beginning of each session the freestream speed is adjusted to the correct speed for the desired Re_c using the 2c-MTV measurements upstream of the airfoil. The temperature is measured at the beginning of each case and is used for computing the viscosity term in the Reynolds number.

2. Airfoil Angle of Attack

The upstream measurements also provide the angle of the freestream, which was utilized for setting the geometric angle of attack such that the freestream angle plus the geometric angle of attack would yield the desired $\alpha = 2, 4, 6, 8$ or 12 degrees. It was later found that the v component of velocity at a location $2c$ upstream of the airfoil has not been sufficiently reduced to a level representative of the freestream. The initial α was determined with a rotational correlation routine using an image of the profile of the airfoil and the theoretical profile. After setting the initial angle all subsequent angle changes were achieved using the traversing mechanism (but also, incorrectly, utilized a new freestream angle, hence why not all $\Delta\alpha$'s are precisely 2° or 4°).

3. Image Acquisition, FOV #1-10

For the first FOV, an undelayed image sequence is recorded, then immediately the delayed image sequence and upstream images are recorded at the same time. To reduce the number of times settings needed to be changed, in the second FOV the delayed image sequence and upstream images are recorded first, immediately followed

by the undelayed image sequence. This pattern was repeated until each FOV had been completed. Each delayed image sequence is 5 minutes, and each undelayed image sequence is 1.5 minutes in length. The flow was observed for several seconds prior to recording the the images and the exposure and time delay were optimized for each FOV. The traverse motion between each FOV was determined from one of the eleven different shift patterns developed to maximize the measurement domain.

4. Image Acquisition, FOV #11 & 12

For FOV #11 and #12, the laser repetition rate was increased from 10 Hz to 20 Hz. To achieve the higher frame rate, the Pixelfly was binned in the cross-stream direction. This yielded a resolution of 512×1392 pixels for the same physical FOV size, i.e. the scale factor in the Y-direction has reduced by a factor of 2. In these FOVs, the delay time was typically 12 ms, which was determined to be the optimum delay time for measuring fluctuating quantities in the freestream based on the relationship between subpixel accuracy and the fluid displacement.

5. Repeat

The procedure listed above is repeated for each angle of attack at the current Reynolds number. The intra-day temperature fluctuations were typically negligible, but could vary significantly day-to-day since the building's ambient temperature fluctuated considerably depending on the weather and building cooling schedule. The final set of experiments were taken over an approximately 2.5 week time period.

BIBLIOGRAPHY

BIBLIOGRAPHY

- Bohl, D. G. (2002). *Experimental Study of the 2-D and 3-D Structure of a Concentrated Line Vortex Array*. PhD thesis, Michigan State University.
- Burgmann, S., Dannemann, J., and Schröder, W. (2007). Time-resolved and volumetric PIV measurements of a transitional separation bubble on an SD7003 airfoil. *Experiments in Fluids*, 44:609–622.
- Burgmann, S. and Schröder, W. (2008). Investigation of the vortex induced unsteadiness of a separation bubble via time-resolved and scanning PIV measurements. *Experiments in Fluids*, 45:675–691.
- Currie, I. G. (1993). *Fundamental Mechanics of Fluids*. McGraw-Hill, 2nd edition.
- Galbraith, M. C. (2009). Implicit large eddy simulation of low-reynolds-number transitional flow past the SD7003 airfoil. Master’s thesis, University of Cincinnati.
- Gendrich, C. P. (1999). *Dynamic Stall of Rapidly Pitching Airfoils: MTV Experiments and Navier-Stokes Simulations*. PhD thesis, Michigan State University.
- Gendrich, C. P. and Koochesfahani, M. M. (1996). A spatial correlation technique for estimating velocity fields using molecular tagging velocimetry (MTV). *Experiments in Fluids*, 22:67–77.
- Gendrich, C. P., Koochesfahani, M. M., and Nocera, D. G. (1997). Molecular tagging velocimetry and other novel applications of a new phosphorescent supramolecule. *Experiments in Fluids*, 23:361–372.
- Hill, R. B. and Klewicki, J. C. (1996). Data reduction methods for flow tagging velocity measurements. *Experiments in Fluids*, 20:142–152.
- Katz, A. W. (2010). Molecular tagging velocimetry measurements of the low-reynolds-number flow around an SD7003 airfoil. Master’s thesis, Michigan State University.
- Koochesfahani, M. M. and Nocera, D. G. (2007). Molecular tagging velocimetry. In Tropea, C., Yarin, A., and Foss, J. F., editors, *Handbook of Experimental Fluid Dynamics*, volume XXVIII, chapter 5.4. Springer-Verlag.
- Ol, M. V., McAuliffe, B. R., Hanff, E. S., Scholz, U., and Kähler, C. (2005). Comparison of laminar separation bubble measurements on a low reynolds number airfoil in three facilities. In *35th AIAA Fluid Dynamics Conference and Exhibit*, number AIAA 2005-5149.
- Olson, D. A., Katz, A. W., Naguib, A. M., Koochesfahani, M. M., Rizzetta, D. P., and Visbal, M. R. (2011). An investigation of the effect of freestream turbulence on the laminar separation bubble on an SD7003 airfoil. In *49th AIAA Aerospace Sciences Meeting including the New Horizons Forum and Aerospace Exposition 4 - 7 January 2011, Orlando, Florida*, number AIAA 2011-395.

Selig, M. S., Guglielmo, J. J., Broeren, A. P., and Giguere, P. (1995). *Summary of Low-Speed Airfoil Data*, volume 1. Soartech Publications.